AN ABSTRACT OF THE DISSERTATION OF

John M. McGlone for the degree of Doctor of Philosophy in

Electrical and Computer Engineering presented on March 20, 2017.

Title:

Development of Amorphous Metal Thin Films for Thermal Inkjet Printing and Microelectronics.

Abstract approved: _____

John F. Wager

Due to a lack of grain boundaries, an amorphous metal thin film (AMTF) possesses advantageous mechanical properties and enhanced chemical stability that is potentially useful for thermal inkjet (TIJ) printing applications. The use of an AMTF as a TIJ resistor or cavitation plate could lead to a thinner TIJ cavitation plate and improved thermal performance. However, if an AMTF is to be used as in a TIJ application, it must remain amorphous during TIJ operation. Six new Ta-based AMTFs are investigated and are found to remain amorphous up to temperatures in excess of 600 °C. AMTFs prepared using a sputter target composition of $Ta_{30}W_{30}Si_{40}$ possess the highest thermal stability, remaining amorphous to a temperature of 1000 to 1100 °C in vacuum. Additionally, this AMTF forms a stable surface oxide when annealed in oxygen up to 700 °C. To demonstrate TIJ feasibility, $Ta_{30}W_{30}Si_{40}$ resistors are fabricated and stressed in an open-pool test bed. $Ta_{30}W_{30}Si_{40}$ AMTFs remain amorphous after testing to $>10^7$ pulses. This suggests that $Ta_{30}W_{30}Si_{40}$ is a promising AMTF candidate material for TIJ applications. Ta-based AMTFs are also employed as bottom electrodes

in metal-insulator-metal tunnel diodes in order to demonstrate their potential for microelectronic applications.

Development of Amorphous Metal Thin Films for Thermal Inkjet Printing and Microelectronics

by

John M. McGlone

A DISSERTATION

submitted to

Oregon State University

in partial fulfillment of
the requirements for the
degree of

Doctor of Philosophy

Presented March 20, 2017
Commencement June 2017

Doctor of Philosophy dissertation of John M. McGlone presented on March 20, 2017

APPROVED:

Major Professor, representing Electrical and Computer Engineering

---

Director of the School of Electrical Engineering and Computer Science

---

Dean of the Graduate School

I understand that my dissertation will become part of the permanent collection of Oregon State University libraries. My signature below authorizes release of my dissertation to any reader upon request.

John M. McGlone, Author

ACKNOWLEDGMENTS

I would like to thank my wife, Marian, without her patience and support none of this work would have been possible. This dissertation is for our wonderful son, Angus Stephen, and his soon to be born brother. I would also like to thank my parents (Stephen and Mary), siblings and their spouses (Stephanie, Ryans, and Alanna), and numerous members of the Ladenburg family for their support of Marian and I while I have been back in school.

I would like to thank Dr. John Wager for his support and guidance in accomplishing this work and completing the writing process. I am grateful for Dr. Douglas Keszler in the Chemistry Department who provided technical support and immense knowledge furthering this materials development. Kris Olsen, in the Chemistry Department, technical contribution and XRD measurements were essential for this work. Rick Presley and Chris Tasker made this work possible by providing cleanroom training and keeping the MaSC cleanroom facilities up and running. Thank you to Dr. Ram Ravichandran and Dr. Pratim Chowdhury for the encouragement during the long writing process. Thank you to my Wager group peers, Kevin Stewart, Hans Chiang, Fan Zhou, and Greg Angelos. A very special thank you is needed for Dr. William Cowell, Dr. Sean Muir, and Dr. Wei Wang for their insightful office conversations and depositing Al_2O_3. Dr. John Conley and his group, Dr. S. Smith, Dr. N. Alimardani, D. Austin, M. Jenkins, M. Hayes and T. Klarr, contributed productive discussions about MIM diodes and deposited Al_2O_3. Dr. Brady Gibbons in the Material Science provided the use of his characterization equipment and measurement advice.

Finally, I would like to thank Dr. James Abbott, Dr. Roberto Pugliese, Dr. Greg Long, and Stafford Johnson for continued support and funding of the amorphous metals research. I would like to thank Dr. William Stickle of HP for the XPS measurements.

This work was funded by the the Hewlett-Packard Company.

TABLE OF CONTENTS

TABLE OF CONTENTS (Continued)

TABLE OF CONTENTS (Continued)

TABLE OF CONTENTS (Continued)

LIST OF FIGURES

LIST OF TABLES

DEVELOPMENT OF AMORPHOUS METAL THIN FILMS FOR THERMAL INKJET PRINTING AND MICROELECTRONICS

1. INTRODUCTION

An amorphous metal thin film lacks grain boundaries and dislocations. These attributes eliminate pathways for chemical attack compared to that of a crystalline metal and improve mechanical strength. Additionally, an amorphous thin film possesses an ultra-smooth surface when deposited onto a substrate with a smooth surface. These considerations have stimulated interest in the use of amorphous metal thin films (AMTFs) for new applications in micro-electro mechanical systems (MEMS), electrode materials, and others industries such as medical coatings [13, 14] .

A thermal inkjet (TIJ) printer is a MEMS device that could benefit from an amorphous metal thin film (AMTF). A TIJ printer employs a mechanically robust and chemically inert metal cavitation plate to increase a device lifetime [1, 3, 15, 16]. The most commonly cited cavitation plate is a β-phase Ta thin film. A mechanically superior AMTF may enable use of a thinner cavitation plate, leading to improved thermal efficiency.

An amorphous material exists in a metastable state. Thus, it is prone to crystallization at an elevated temperature. This tendency to crystallize is a serious liability of an amorphous material if it is to be used as a cavitation plate since advantages associated with its amorphous structure are lost. For TIJ applications, thermal stability to temperatures well in excess of 340 °C are required [1, 17, 18].

Using an amorphous metal as an electrode in electronics is also possible. The ultra-smooth surface of an amorphous metal is particularly attractive for use in an electronic de-

vice. Previously, AMTFs have been employed as electrodes for metal-insulator-metal (MIM) tunnel diodes [19, 20, 21, 22, 23] and as a gate metal in a MOSFET [24, 25]. For a MIM diode, the smooth surface enables realization of an uniform electric field to facilitate Fowler-Nordheim tunneling and to improve device performance, manufacturability and reliability.

The primary goal of the research discussed herein is to develop and characterize new thermally-stable AMTFs for TIJ cavitation plate application. Development of a thermally robust AMTF is potentially useful for TIJ applications. The AMTFs developed for TIJ application are also potentially useful for the fabrication of MIM tunnel diodes.

The structure of this thesis is as follows. Chapter 2 presents a review of pertinent literature and provides the technical background necessary to understand thermal inkjet printers, amorphous metals, and the results presented in later chapters. Chapter 3 provides details on fabrication techniques and characterization methods, such as structural analysis (XRD, AFM, TEM) and electrical characterization methods, which are used in this study. Chapter 4 presents characterization results for each AMTF material system. Chapter 5 provides application testing results for amorphous metals in the TIJ application. Chapter 6 provides analysis of fabricated MIM diodes utilizing the new metals developed here-in. Finally, Chapter 7 presents conclusions and recommendations for future work.

2. LITERATURE REVIEW

This chapter reviews the relevant literature used in developing this dissertation work and is divided into three sections. The first section introduces thermal inkjet (TIJ) printing, TIJ operating principles, and requirements for metal thin film applications. This provides design considerations and specifications for developing amorphous metals in TIJ applications. The second section introduces amorphous metals and provides a brief background of these materials. An analysis of driving forces giving rise to improved thermal stability is outlined, followed by a review of relevant reference materials used to establish an amorphous metals thermal stability database. Finally, guidelines are formulated for development of a thermally stable amorphous metal thin film (AMTF). The final section of this chapter covers electronic transport in amorphous metals, basic diode device operation, and metal-insulator-metal (MIM) devices.

2.1 Thermal Inkjet Printing

A TIJ printer utilizes drop-on-demand (DOD) technology to eject fluid, such as color ink, onto a medium, such as paper. DOD technology uses a piezo-electric, an electro-static membrane [26], or a thermally-driven actuator to create a single droplet of ink [1, 27, 28, 17]. The TIJ DOD device is a thermally-driven actuator where joule (resistive) heating of a resistor creates a vapor bubble, which acts as a piston to eject ink from the nozzle. TIJ DOD actuation is not only important to printing but it has also expanded to other applications such as maskless lithography [29, 30], 3-D ceramic printing [31], and pharmaceutical industries [32].

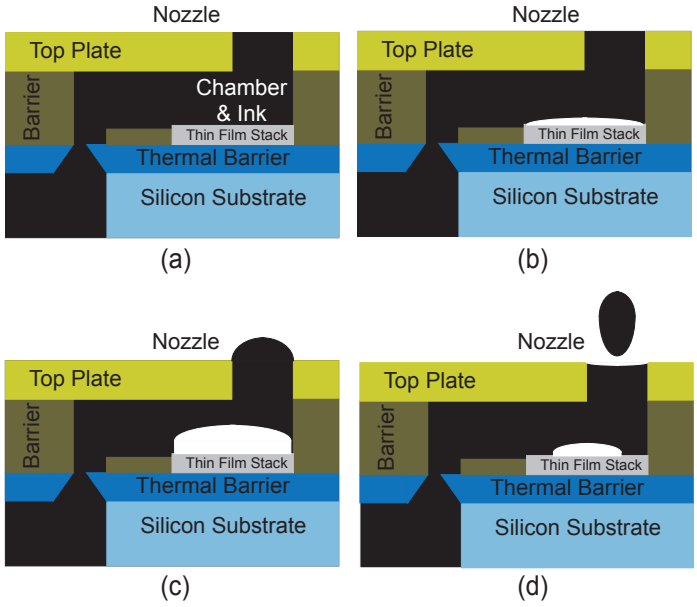

Figure 2.1: (a) An illustration of a front-shooter TIJ firing chamber with ink prior to electrical pulse/firing event. (b) TIJ firing chamber as the electrical pulse is sent heating the thin-film stack, resulting in the creation/nucleation of a single vapor bubble (depicted in white). (c) The bubble expands and pushes ink out of the nozzle, leading to the creation of an ink droplet. (d) The chamber cooling after the electrical pulse has stopped and the droplet of ink has been ejected from the firing chamber [1, 2].

The process of generating a vapor bubble, to create a droplet of ink in a TIJ device is depicted in Fig. 2.1 [1, 2]. The firing chamber and ink prior to generating the vapor bubble, also known as a firing event, is shown in Fig. 2.1(a). To eject a droplet of ink, a voltage pulse is sent to a resistor in the thin-film stack, causing the resistor to heat up, increasing the temperature of the thin-film stack. The pulse is designed to increase the ink temperature high enough to form a single vapor bubble, corresponding to homogeneous nucleation. This occurs when the ink reaches its superheat limit, $\sim$ 330-400 °C for aqueous-based inks [1, 27, 28, 18], as shown in Fig. 2.1(b). As the bubble grows, it acts like a piston providing momentum to the ink [33] and ejects ink from the nozzle, as shown Fig. 2.1(c). After the electrical pulse is applied, the thin-film stack passively cools and the bubble begins to col-

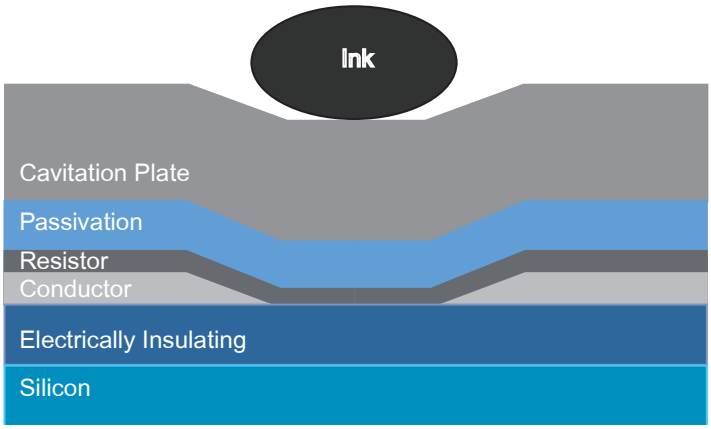

Figure 2.2: TIJ thin-film stack used to generate and transfer heat to ink. The thin-film stack is built on a silicon substrate, with an electrical insulating layer, conductor, resistor material, passivaton layers, and a cavitation plate [3].

lapse as ink refills the chamber, as shown in Fig. 2.1(d). At this point, the ejected ink droplet has enough momentum to break free from chamber ink and is transferred to the paper. Finally, as the thin-film stack cools, the bubble completely collapses, sometimes leading to a cavitation effect in which mechanical damage is imparted to the thin film stack [17, 2, 3].

2.1.1 Thermal Inkjet Thin-Film Stack

A TIJ thin-film stack employed in production inkjet printers is shown in Fig. 2.2. Modern TIJ design utilizes a silicon substrate with a SiO_2 layer providing electrical and thermal isolation. The silicon wafer acts as a heat sink to aid in the passive cooling of the resistor between firing events [17, 3]. Thermal isolation, typically SiO_2, provides a thermal barrier for more efficient heat transfer to the ink [1, 17, 3, 15]. Conductor traces, typically AlCu, connect a resistor to a field effect transistor (FET), which controls the operating pulse for DOD operation. The resistor material is deposited over the conductor and provides the joule heating for TIJ operation. The passivation layers are deposited over the resistor and

are employed for electrical isolation and chemical protection. Typical passivation layers consist of a SiN (electrical isolation) and SiC (chemical protection) stack [33, 3, 15]. A crucial requirement for these films is to ensure a lack of pinholes in order to prevent ink from penetrating to the resistor. Finally, a cavitation plate is used for chemical and mechanical protection to increase reliability [15].

Turn on energy (TOE) defines the amount of energy required for a resistor to heat the thin-film stack to nucleation temperatures at the ink interface. In typical operation, an over energy is applied to the resistor to ensure nucleation occurs. The energy, E (J), sent to the resistor is defined as [34],

$$E = P * t = I * V * t, \tag{2.1}$$

where P is power (W), t is time (s), I is current (A), and V is voltage (V). The TOE is typically determined experimentally and depends on material properties such as thermal conductivity and thickness of the layers above the resistor. A thicker stack or materials with lower thermal conductivity require more energy, increasing the required power [34].

2.1.2 Metal Thin Film Requirements

Metal thin films are commonly employed as the cavitation plate or resistor material in the TIJ thin-film stack. Table 2.1 lists requirements and ideal properties for metal thin films used in TIJ.

Table 2.1: List of desired material properties for TIJ cavitation plate and resistor materials.

Property	**Cavitation Plate**	**Resistor**
Thermal Stability	400-1000 °C	400-1000 °C
Chemical Robustness	Inks consist of anionic dyes w/ pH values 5-12 [35] Oxide resistant/stable	Resistant to ink
Mechanical Strength	High fracture toughness	High fracture toughness
Adhesion	Adheres to SiC and SiO_2	Adheres to SiO_2
Resistivity	N/A	150-6000 [$\mu\Omega$-cm]
Temperature Coef. Resistance	N/A	0 [ppm-K^{-1}]
Thermal Conductivity	Large	N/A
Kogation Resistance	Prevent ink build up on surface	N/A

Table 2.1 shows that the requisite thermal stability, chemical robustness, and mechanical strength properties are similar for the cavitation plate and the resistor. The thin-film stack undergoes severe thermal cycling from room temperature to temperatures approaching 1000 °C numerous times during a printer's lifetime. Thermal stability requires consistent material properties, such as phase retention, mechanical strength, and minimal internal stress at elevated temperatures. Chemical stability requires corrosion resistance to the operating environment. This environment consists of exposure to a range of pH values (5 to 12), aqueous-based inks (which may oxidize the film), and ink dispersants including Na, Cl, and K [1, 3, 35]. The metal films must be chemically inert not only in ambient conditions but

also at firing temperatures. Finally, the thin films must be mechanically robust to withstand the forces created by bubble collapse (cavitation) and adhere to the material onto which they are deposited. Cavitation damage and chemical attack of the thin-film stack degrades the integrity of the resistor, typically resulting in an open circuit failure [33, 15, 36, 37, 38].

Manufacturability and process integration are two final concerns that need to be considered for all metal thin films [33, 3]. The success of TIJ products is due to the development of cost-effective printing solutions. Metal films used in production are typically deposited through sputtering, a common industrial process. The films must also be compatible with etchants and fabrication integration issues in silicon processing. Finally, novel thin film solutions, such as graded resistors or multi-layer stacks, must possess extraordinary performance in order to justify any additional complex or expensive processing techniques.

2.1.3 Cavitation Plate Material Requirements

A cavitation plates sole function is to protect the resistor from mechanical and chemical damage in order to increase resistor life. In the development of inkjet technology, the cavitation plate was added to increase the lifetime of the resistor as the ink volumes increased and as color printing developed [3, 15]. The mechanical, chemical, and thermal stability requirements described in the previous section are critical, especially at the interface between the ink and thin-film stack.

The typical design tradeoff for a cavitation plate is lifetime versus thermal efficiency. Through increased thickness, the resistor lifetime increases but the thermal efficiency is decreased, thus requiring a larger TOE and more power. This causes more thermal stress on the thin-film stack below the cavitation plate, requiring greater thermal stability of the resistor. Additionally, having a high thermal conductivity is crucial. A more thermally conductive

material improves heat transfer from the heater to the ink. A cavitation plate is generally 0.2 to 3 μm in thickness.

The last requirement of a cavitation plate is to prevent kogation with existing inks [1]. Kogation is the build up of ink residue on the surface of the cavitation plate. This creates additional thermal barriers and changes the TOE. Kogation issues are dependent on a combination of ink chemistry and cavitation plate material.

2.1.3.1 Cavitation Plate Materials

Ta, Ti [39], Pd [40], Ir [41], TaFeNiCr alloy [42], FeCoCrMn alloy [43], and diamond-like carbon [44] have all been reported in the literature and in patents as cavitation plate materials. Most of the materials listed are found in patents rather than in journal articles. Cavitation plate performance is strongly dependent on printer design and on product inks specific to each company. Potentially useful inkjet materials are generally found in the literature by searching for hard, scratch-resistant wear coatings. These materials are subsequently tested in house [45]. Results of this testing are likely to be considered proprietary information.

Ta is the most commonly reported cavitation plate material [1, 33, 3, 15, 46] and thus can be used as a reference material for cavitation plate thin film assessment. Ta is a refractory metal that is deposited through magnetron sputtering. Fig. 2.3 shows a TIJ thin-film stack with the top, thickest layer being a $\sim$500 nm thick Ta cavitation plate. Sputtering Ta deposits in the β phase (β-Ta) with a columnar structure and well-defined grains. The β-phase to α-phase transition temperature has been reported as $\sim$775 $^{\circ}$C [47]. Thin film β-Ta possesses a hardness of 18 GPa, a Young's modulus of 13 GPa, and is known to be chemically stable. Bulk Ta possesses a bulk thermal conductivity of 57 $\mathrm{Wm^{-1}K^{-1}}$. Note that in oxidation

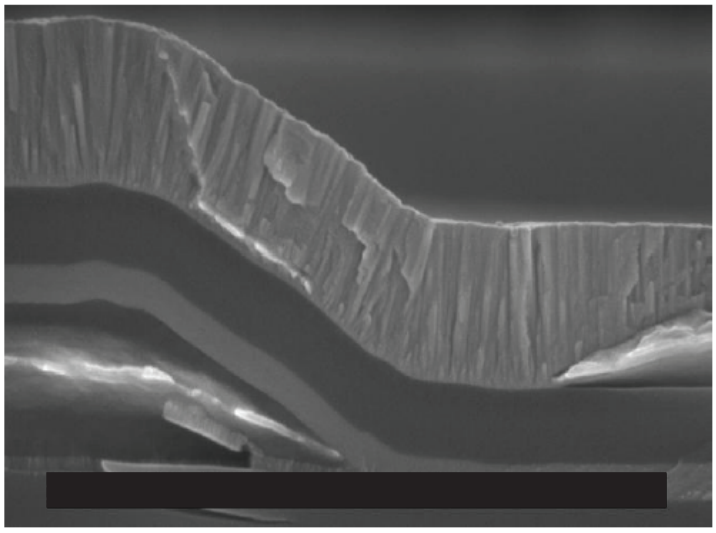

Figure 2.3: A scanning electron microscope image of a TIJ thin-film stack with a columnar Ta cavitation plate as the top layer.

studies above 700 °C, stress from oxide diffusion in grain boundaries creates cracking and stability issues [48].

The TaFeNiCr [42] or FeCoCrMn [43] alloys listed previously serve as an interesting comparison to single-element materials. These references are from Canon (TaFeNiCr) and Hewlett-Packard (FeCoCrMn) patents, which claim each alloy possesses an amorphous or pseudo-amorphous microstructure for improved chemical stability and mechanical strength. The benefits are cited to be due to an atomically-flat surface and an amorphous microstructure. In both patents, the amorphous layer is part of a two-layer cavitation plate stack in addition to Ta.

2.1.4 Resistor Material Requirements

The resistor is at the heart of TIJ operation. The resistance determines much of the system design and power parameters. TIJ design employs a FET to control a voltage pulse

to the firing resistor. This provides power for a set time, delivering TOE for nucleation. The power dissipated by a resistor is defined as [49],

$$P = I * V = I^2 * R = \frac{V^2}{R}, \tag{2.2}$$

where R is resistance (Ω). As seen by Eq. 2.2, a lower resistance (larger resistance) requires less voltage (more voltage) but more current (less current) to achieve a specific power. The amount of current dictates the size of the firing FETs in the integrated electronic drivers. Smaller current allows for smaller gate widths, higher packing density, and lower cost electronics. Resistors range from 30 to 1000 Ω. For a 30 Ω resistor, a 10 to 20 V pulse is reported as the voltage range required for nucleation (corresponding to 3.3 - 13.3 W; 160 - 333 mA) [18, 50]. Note that the large range is due to the use of dramatically different thin-film stacks in test devices. The ideal resistor thickness is 50 to 200 nm [51], corresponding to a desired resistivity range of $\sim$150 to 6000 $\mu\Omega$-cm.

A small temperature coefficient-of-resistance (TCR) is the other desired electrical property of the resistor material [37]. Resistance (R_1 (Ω)) at an elevated temperature for most metals can be calculated as,

$$R_1 = R_0 + \alpha * R_0[T_1 - T_0], \tag{2.3}$$

where R_0 (Ω) is the room temperature resistance, α is the resistor material TCR (ppm-K^{-1}), T_1 (K or $^\circ$C) is the elevated temperature, and T_0 (K or $^\circ$C) is room temperature [33]. For a material with a large TCR of 3850 ppm-K^{-1}, a 60 Ω resistor at room temperature will double in resistance to 123 Ω at 300 $^\circ$C, a minimum TIJ firing temperature. This leads to complex operating parameters and shows why a small TCR is needed for stable TIJ performance [52].

The thermal, chemical, and mechanical stability properties of a thin film determine the thin-film stack design. Improving these properties for the resistor enables use of thinner passivation and cavitation layers. This allows for more efficient thermal performance and lower operating power.

2.1.4.1 Current TIJ Resistor Materials

Table 2.2: A list of TIJ resistor materials with corresponding resistivity and TCR values.

Material	**Resistivity** [$\mu\Omega$-cm]	**Thermal Coeffience of Resistance** [ppm-K^{-1}]	**Reference**
TaAl	200-280	-120	[53, 54]
Degenerate Poly Si	$\geq$ 500	–	[55]
HfB_2	220-340	-33	[56, 57]
TaN	280 - 2997	-143 to -2000	[58]
WSiN	800-4500	-100 to -1200	[59, 60]
TaSiN	800-10000	Not Provided	[61]
TaRu	180-320	Not Provided	[51, 53, 62]
$WSiN_xO_y$, $TaSiN_xO_y$	1400-30000	Not Provided	[63]
IrO_2-TiO_2 (ALD)	356-1500	-75 to -420	[64]
RuO_2-TiO_2 (ALD)	370-2600	-55 to -557	[65]
RuO_2-Al_2O_3 (ALD)	243-1200	-63 to -381	[66]
$Ru_X(AlN)_{1-X}$ (PE-ALD)	490-9 x 10^7	x=.47 TCR = -420 x= .58 TCR = +335	[52]

Continued on next page

Table 2.2 – *Continued from previous page*

Material	**Resistivity** [$\mu\Omega$-cm]	**Thermal Coeffience of Resistance** [ppm-K^{-1}]	**Reference**
TiAlN	225-317	-765	[67]
CrAlN	200-1600	-2670	[68]

Table 2.2 lists materials that have been cited as potential TIJ resistor materials, with a corresponding resistivity range, and TCR values. Original resistor materials, such as TaAl, were choosen due to a high resistivity in comparison to that of a conductor metal. As TIJ designs evolved, higher resistance materials, e.g., TaN and WSiN, were developed. These materials have been reported to be unstable in inks, requiring a need for better chemical robustness [64]. Recent investigations of mixed metal oxides such as IrO_2-TiO and RuO_2-Al_2O_3 are an attempt to improve mechanical and chemical stability while maintaining a higher resistivity. In turn, it is hoped that this would lead to a reduction in the number of passivation and/or cavitation layers which would improve inkjet delivery thermal performance.

2.1.5 TIJ Materials Summary

The success of TIJ printing has relied upon delivering a reliable product at low cost. To maximize printing speeds and lower system costs, thin film performance has been optimized over the last 30 years of production [17, 3, 15]. In order to introduce change into this well-established product, a new material must have greatly improved properties to create any change to a stable design. A thermally-stable amorphous metal thin film could provide advantageous TIJ properties, as outlined in the next section, which would lead to the adoption of a new material into this established application.

2.2 Introduction to Amorphous Metals

Most metals in nature are found to be polycrystalline [4, 69]. A crystalline structure has translational symmetry in which atoms are arranged in a repeating order, thereby forming a lattice. A lattice possesses long-range order formed by repeated short-range positioning of atoms in a unit cell. Such a lattice is characterized by a coordination number (CN), or the number of nearest neighbors, and is the same regardless of its position in the lattice [70]. Crystalline structures can be determined by x-ray diffraction (XRD) or electron beam diffraction techniques. In these characterization measurements, well defined peaks occur in the diffraction patterns due to the high degree of order. Crystalline metals have been studied extensively and to a large extent their structural relationships to material properties are well understood.

Amorphous materials possess short-range but not long-range order. This implies that the arrangement of a given atom and its nearest-neighbor atoms is somewhat similar to that expected in a corresponding crystalline solid. However, next-nearest-neighbor atoms and further separated atoms are to a large extent randomly distributed. However, even short-range order is not perfect since the CN for an atom in an amorphous solid may vary [4]. The structure of an amorphous solid is typically characterized by broad peaks in diffraction measurements, e.g., XRD or electron diffraction [4, 69]. This is in dramatic contrast to the very sharp peaks characteristic of a crystalline lattice. Microstructure in an amorphous material or glass is often discussed within the context of an atomic pair distribution function (PDF) or a radial distribution function [69, 71]. A PDF establishes the average distance between pairs of atoms in an amorphous solid [72]. Determining the structure of an amorphous metal and relating its structure to physical properties is an active area of research [71].

In 1960, the Pol Duwez research group at Cal-Tech created the first metallic glass through rapidly quenching a Au-Si compound [73]. This was the birth of bulk metallic glass (BMG) research. The term metallic glass refers to an amorphous metal synthesized through rapidly quenching a melt. Prior to the report by Pol Duwez, amorphous metal synthesis relied on vapor deposition onto a cooled substrate, thus quenching to create a thin-film amorphous alloy. A BMG is an alloy with no long-range crystalline order. Furthermore, a BMG typically conforms to the following characteristics: possesses a minimum thickness of 1 mm, comprised of three or more elemental components, possesses a wide super-cooled region, and is achieved through slow solidification[1] of a melt, typically 10^3 K s^{-1}, [4].

An amorphous microstructure is often advantageous due to the absence of grain boundaries [4, 69]. This can provide an amorphous alloy with high resistance to corrosion, in comparison to the same alloy in polycrystalline form, since a lack of grain boundaries reduces the number of enhanced diffusion pathways for chemical attack [4, 69, 74]. The amorphous microstucture can improve mechanical hardness as mechanical stress and fatigue commonly occur along grain boundaries. Soft magnetic properties are improved via use of an amorphous microstructure [4, 74, 75]. Finally, the lack of grain boundaries means that amorphous metal thin films can be prepared with atomically flat surfaces leading to uniform electrical properties when used as bottom contacts [19, 24].

2.2.1 Review of Amorphous Metal Mechanical Properties

Figure 2.4(a) is a comparison of the tensile strength versus Young's modulus in an amorphous metal and a crystalline metal alloy. This further illustrates amorphous metal mechanical advantages compared to crystalline material. A review of basic mechanical prop-

[1] A slow solidification rate is in comparison to other metallic glass cooling rates, i.e., 10^6 K s^{-1}

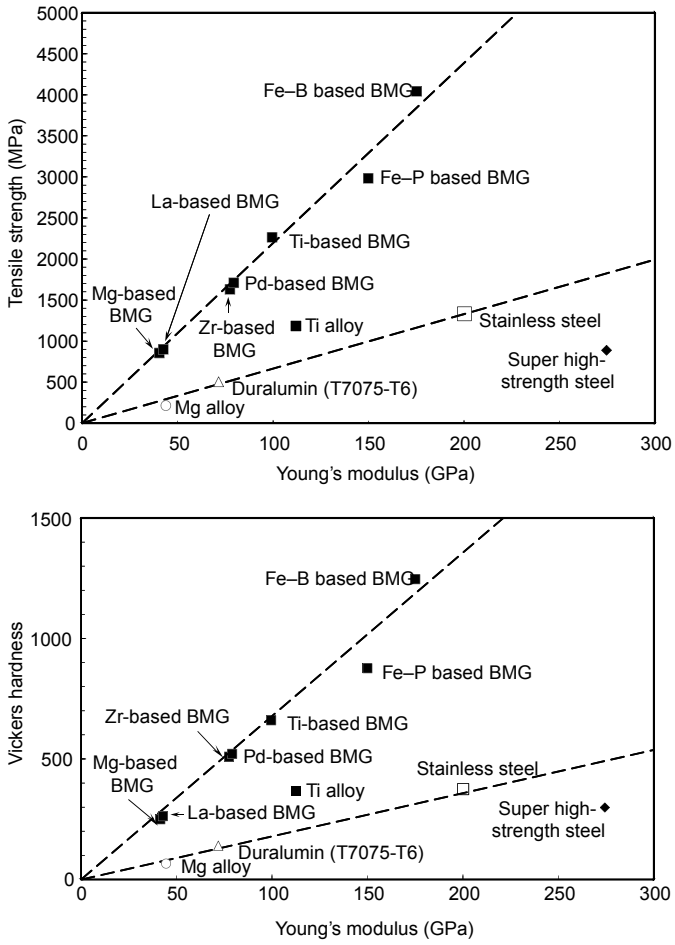

Figure 2.4: Comparison of mechanical properties and trends of amorphous metals versus polycrystalline metals for (a) tensile strength versus Young's modulus, and (b) Vickers hardness versus Young's modulus [4].

erties, e.g., Young's modulus, elastic modulus, tensile strength and hardness, is provided in Appendix 8.1. It is apparent that the tensile strength is much larger for an amorphous metal than it is for a crystalline alloy. This improvement is due to the lack of dislocations in the amorphous structure. The dashed lines indicate expected trends for potential new materials. New amorphous metals are expected to demonstrate even higher strength.

Figure 2.4 (b) is a comparison of Vickers hardness versus Young's modulus in an amorphous metal and a crystalline metal alloy. An amorphous metal has a larger Vickers hardness

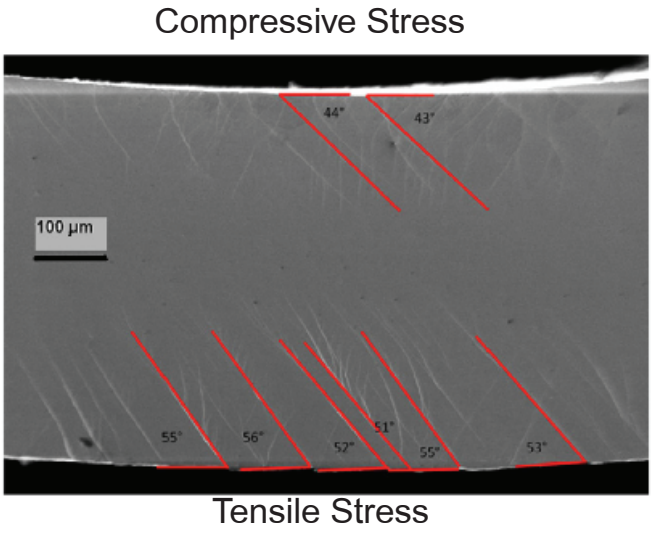

Figure 2.5: A scanning electron microscope (SEM) image of shear bands, highlighted by red lines, created in a bend test. Compressive (tensile) shear occurs at the top (bottom) of the image [5].

compared to a crystalline metal having the same Young's modulus. This property makes an amorphous metal an attractive option for other scratch- and wear-resistant applications [4]. Based on this trend, an amorphous metal is likely to better withstand TIJ resistor cavitation forces.

In Fig. 2.4, an amorphous metal at the same Young's modulus exhibits larger tensile strength (and Vickers hardness) in comparison to a crystalline alloy. Thus, it may be inferred that an amorphous metal offers an improvement in performance with respect to elastic behavior. Additionally, the bulk modulus of an amorphous metal is generally 6% smaller, i.e., more elastic, for an amorphous metal in comparison to a crystalline alloy composed of the same constituent elements [76]. The superior elasticity of an amorphous metal is attributed to the lack of dislocations in an amorphous microstructure [4]. Amorphous metals are currently used in spring applications and in sporting goods equipment, such as golf clubs and tennis racquets, where high elasticity is desirable [4, 69, 77].

A typical amorphous metal mechanical failure is non-ductile and is attributed to the development of shear bands. Figure 2.5 is a scanning electron microscope (SEM) image of the development of shear bands from a bend test [5]. A shear-induced failure is ascribed to rearrangement of localized atoms within the structure, leading to cracking and eventual failure [78]. In an amorphous metal, it is not possible to predict the location of the failure prior to the failure occurring, since shear-induced failure is not attributable to lattice defects or other atomic structural features. The failure mechanism and brittle behavior have precluded amorphous metals from being employed in many applications [4, 69, 79].

AMTFs have been an increasingly active area of research. They are used in microelectromechanical systems (MEMS) for their mechanical properties. MEMS applications include springs, hinges, variable capacitors, and cantilevers [80, 81, 82, 83]. While the development of shear bands is still expected, AMTFs appear to exhibit different mechanical behavior than their bulk metallic glass counterparts. It has been reported that a thinner amorphous metal sample possesses more ductility in comparison to a thicker amorphous metal of identical composition [76, 13]. These authors suggest that the dimensionally-enhanced ductility of a thin film may be due to the fact that the spatial distribution of shear bands (typical widths are 10-1000 nm) is close to the thickness of the film [76, 14]. AMTFs are a topic of accelerating interest and the subject of a recent review and expanding applications [13, 14].

2.2.2 Thermal Properties of an Amorphous Alloy

An amorphous metal is a metastable material. A metastable material does not exist in thermodynamic equilibrium. Figure 2.6 shows an energy diagram of a metastable material where ΔG is the Gibbs free energy difference between the amorphous metastable state and the energetically favored crystalline state and E_A is an energetic barrier inhibiting the ma-

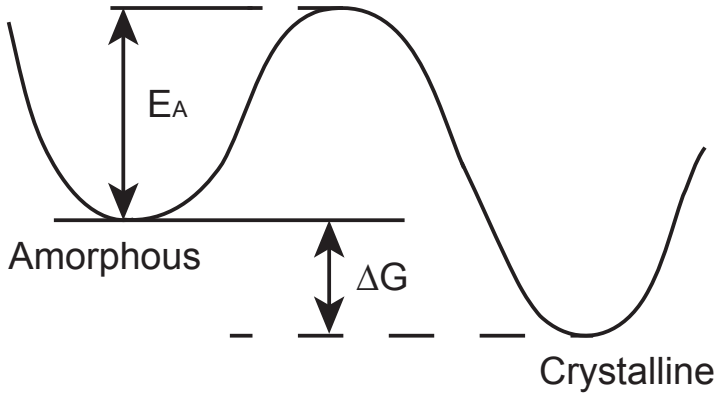

Figure 2.6: An energetic picture of a metastable amorphous state and an equilibrium crystalline state. ΔG is the Gibbs free energy difference between amorphous and crystalline states and E_A is an energy barrier inhibiting transformation from the amorphous to the crystalline state.

terial from moving to its lowest energy thermodynamic equilibrium state. In an amorphous metal, atoms find themselves locked into a disordered state prior to crystallization. An energy barrier exists which precludes atomic rearrangement such that the metal can achieve its lowest energy equilibrium state. Thus, an amorphous metal energy state constitutes a local minimum whose energy is larger than that of the crystalline state which is thermodynamically more favorable as a global minimum. An amorphous metal microstructure persists until enough energy is provided to facilitate its crystallization. Annealing an amorphous metal to a certain temperature provides sufficient energy to overcome the barrier and crystallize the metal.

Figure 2.7 is a differential scanning calorimetry (DSC) plot for a typical amorphous metal. DSC is a characterization technique that measures the energy flow into or out of a sample. The energy exchange is constant until the glass transition temperature, T_g [K], is

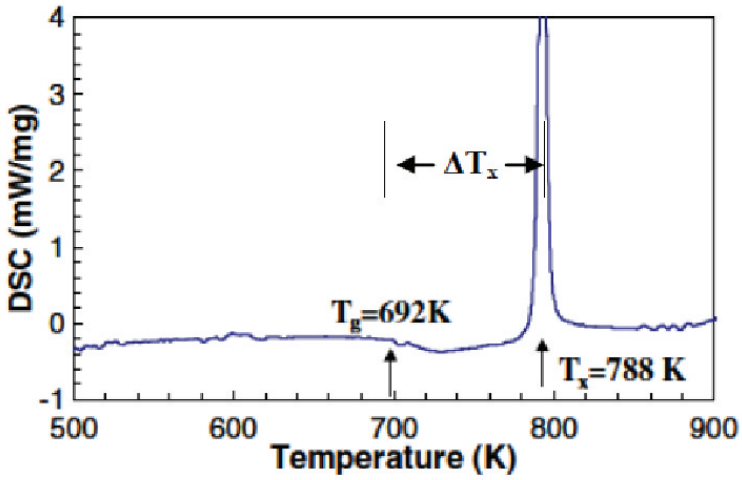

Figure 2.7: Differential scanning calorimetry (DSC) plot for a $Zr_{55}Cu_{30}Al_{10}Ni_5$ bulk metallic glass. The glass transition temperature (T_g), crystallization temperature (T_x), and width of the super-cooled region (ΔT_x) are indicated [6].

reached. This is followed by a super-cooled region, ΔT_x [K], and then by an exothermic spike at the crystallization temperature, T_x [K]. Additional crystalline phase changes and the melting temperature, T_m [K], occur at higher temperatures. The exothermic spike occurs when sufficient energy is applied to allow the material to overcome the energy barrier (E_A in Fig. 2.6) and release energy as the material moves to a lower energy state. An important goal of the research discussed herein is to maintain an amorphous microstructure to as large a temperature as possible for TIJ compatibility.

2.2.3 Glass Forming Ability

In order to fabricate an amorphous metal, constituent elements must be rapidly brought from a molten or vapor state into the solid state by quenching. Properties such as atomic radii and enthalpy of mixing of each constituent element in an alloy determine if the alloy can form an amorphous glass. Glass forming ability (GFA) refers to how readily a given set

of elements can form an amorphous alloy. Various methods for predicting GFA have been developed. Unfortunately, most quantitative descriptions of GFA provide conflicting results. Typically, an amorphous metal must be synthesized before its GFA can be assessed [69]. Thus quantitative estimates of GFA are of limited utility for designing a new amorphous metal. An alternate approach to assessing GFA within the context of amorphous metal thin film design, based on kinetic and thermodynamic considerations, is outlined below.

2.2.3.1 Kinetic Considerations

Cooling rate kinetics are an important consideration in establishing glass formation [4]. Formation of an amorphous structure requires the cooling rate to be fast enough to lock atoms inton place in a metastable energy state (see Fig. 2.6). A fast cooling rate prevents nucleation and circumvents crystallization. A critical cooling rate in which crystallization is suppressed is unique for a given alloy. Different bulk metallic glass processing techniques, such as the melt spun ribbon technique, are used to achieve the fast cooling rates necessary [4]. For thin-film processing, vapor deposition techniques, such as sputtering, achieve these rates as the vapor species impinge onto the substrate and cool.

2.2.3.2 Thermodynamic Considerations

Inoue proposed three empirical rules for designing an amorphous metal [4, 84]:

1. The material should be composed of a mixture of at least three different elements.

2. There should be a difference of at least 12 % in the atomic size of each of the components.

3. There should be a negative heat of mixing among the components.

These three rules can be understood in the context of thermodynamic considerations [4]. The change in Gibbs free energy, Δ G [$kCal - mol^{-1}$], is equal to,

$$\Delta G = \Delta H - T\Delta S, \tag{2.4}$$

where ΔH [J] is the change in enthalpy, T is temperature [K], and ΔS [$kCal - mol^{-1}K^{-1}$] is the change in entropy. A negative value of ΔG denotes a thermodynamically favorable process. As ΔG becomes more negative, the process becomes more thermodynamically favorable. It is apparent from Eq. 2.4 that thermodynamic stability can be enhanced in an amorphous alloy by making ΔH more negative and ΔS more positive.

Inoue's first two criteria contribute to an increase in ΔS while the last criterion contributes to ΔH. The first criterion, adding multiple elements, creates more bonding arrangements for an atom. This can be interpreted as a lattice confusion principle which increases the disorder of the system [69]. The second criterion, employing elements with differing atomic radii, creates more entropy through enabling denser packing [4, 85]. This is a topological consideration involving the use of elements with differing radii in order to accomplish more efficiently packing into a volume. The last criterion, a large negative heat of mixing, relates to the enthalpy of mixing, ΔH_M, and contributes to a lowering of ΔH. A valuable collection of calculated (estimated) enthalpy of mixing values for a wide variety of multi-component metal and metalloid alloys is available from Takeuchi and Inoue [85]. By following the first two rules using elemental properties and utilizing calculated mixing enthalpies, it is possible to design an alloy that is likely to form an amorphous metal with an overall negative value of free energy. Post quenching considerations determine if an amorphous alloy is stable with respect to crystallization at high temperature.

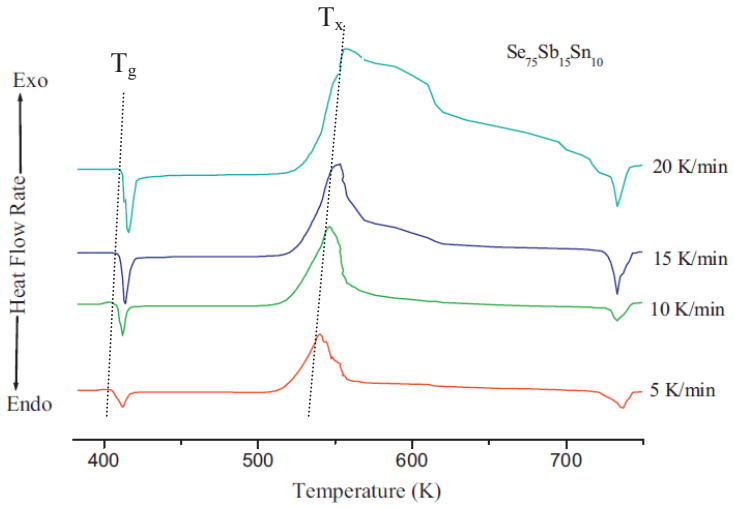

Figure 2.8: Differential scanning calorimetry (DSC) curves showing increasing glass-transition temperature (T_g) and crystallization temperature (T_x) at increasing heating rates [7].

2.2.4 Crystallization Kinetics

Crystallization is a thermally-activated process. The crystallization rate constant, k, is often formulated using the Arrhenius equation,

$$k = A \exp\left(\frac{-E_A}{k_B T}\right), \tag{2.5}$$

where A is a pre-exponential factor (which may depend upon temperature), E_A is an activation energy [eV], k_B is Boltzmann's constant [eV K^{-1}], and T is temperature [K]. As temperature increases, the tendency towards crystallization increases exponentially, at a rate established by the magnitude of E_A. In the design of a more refractory amorphous metal, a large E_A is desirable. In turn, a large E_A increases T_X.

Figure 2.8 shows DSC curves of a Se-based alloy evaluated at different heating rates [7]. It is evident there is an increase in T_x with increasing heating rate. It is important to

recognize that T_x is not a thermodynamic parameter, such as T_m, and that it depends on the heating rate [4, 86]. Kissinger formulated a relationship, similar to Eq. 2.5, which includes the heating rate dependence [87, 88]. By specifying the activation energy (E_A) in Eq. 2.5 as a crystallization activation energy (E_x) and assuming that the pre-exponential term in Eq. 2.5 has a ${T_x}^2$ dependence, Eq. 2.5 can be recasts as.

$$\ln\left(\frac{\beta}{{T_x}^2}\right) = -\frac{E_x}{k_B T_x} + constant, \tag{2.6}$$

where β is the heating rate. E_x can be calculated by using data from Fig. 2.8 in conjunction with Eq. 2.6. More speciffically, a plot of $\ln\left(\frac{\beta}{{T_x}^2}\right)$ versus $\frac{1}{T_x}$ yields a line with a slope of $-\frac{E_x}{k_B}$ which allows estimation of the activation energy E_x.

2.2.5 Reference Materials

Table 2.3: Tabulated properties of amorphous metals with composition, glass-transition temperature (T_g), and material type (BMG = bulk metallic glass, TF = thin film).

#	Amorphous Metal (atomic %)	T_g (°C)	Material Type	Reference
1	$Ni_{59\text{-}62}Ta_{38\text{-}41}$	720	BMG	[89]
2	$Ta_{50}Ni_{32}Co_{18}$	706	BMG	[90]
3	Ta_{42} $Ni_{36}Co_{22}$	731	BMG	[90]
4	$Mo_{55}Si_{28}Co_{12}Y_5$	862	BMG	[91]
5	$Mo_{45}Si_{28}Ta_{10}Co_{12}Y_5$	864	BMG	[91]
6	$Mo_{44}Si_{26}Ta_5Zr_5Fe_3Co_{12}Y_5$	928	BMG	[91]

Continued on next page

Table 2.3 – *Continued from previous page*

#	Amorphous Metal (atomic %)	T_g °(C)	Material Type	Reference
7	$Ta_{40}W_{40}Si_{10}C_{10}$	$\geq$ 1120**[2]	TF	[24]
8	$W_{56}Ta_{24}Si_{10}B_{10}$	1100-1200	BMG	[92]
9	$Ta_{20}W_{60}Si_{10}C_{10}$	400 - 800[2]	TF	[93]
10	$Ta_{60}W_{20}Si_{10}C_{10}$	900 - 1000[2]	TF	[93]
11	$Ta_{30}W_{30}Si_{20}C_{20}$	$>$ 1000[2]	TF	[93]
12	(Metal 1*+Metal 2*)[3] $_{80}Si_{10}B_{10}$	400-1200	BMG	[92]
13	$Ta_{95}Cu_5$	600-700	TF	[94]
14	$Ta_{55}Zr_{10}Al_{10}Ni_{10}Cu_{15}$	561	BMG	[95]
15	$Zr_{55}Al_{10}Ni_5Cu_{30}$	419	BMG	[6]
16	$Zr_{63}Cu_{18}Al_{10}Ni_9$	397	BMG	[96]
17	$Zr_{58.8}Cu_{16.8}Al_{10}Ni_{8.4}Ta_6$	407	BMG	[96]
18	$Ni_{60}Nb_{6.8}Ta_{27.2}Sn_6$	647	BMG	[97]
19	$Ni_{60}Nb_{27.2}Ta_{6.8}Sn_6$	607	BMG	[97]
20	$Pd_{67.8}Cu_{14.3}Si_{17.9}$	387	TF	[98]
21	$Pd_{75.1}Cu_{6.6}Si_{18.3}$	361	TF	[98]
22	$Pd_{67.7}Cu_{18.2}Si_{14.1}$	354	TF	[98]
23	$Pd_{80.7}Cu_{6.9}Si_{12.4}$	318	TF	[98]
24	$Cu_{81.8}Si_{18.2}$	365	TF	[98]

Continued on next page

[2] Indicates crystallization temperature

[3] * indicates a refractory metal or near refractory metal, such as Ti, Zr, Hf, V, Nb, Ta, Cr, Mo, W

Table 2.3 – *Continued from previous page*

#	Amorphous Metal (atomic %)	T_g °(C)	Material Type	Reference
25	$Co_{43}Fe_{20}Ta_{5.5}B_{31.5}$	622-638	TF	[99]

Table 2.3 is a list of amorphous metals found in the literature, along with their T_g and a material type designation specifying whether they were synthesized as a BMG or in a thin film (TF) form. Since the goal of this study is to develop a high temperature amorphous metal, the emphasis in the results section focuses on crystallization temperature, T_x, as it is an absolute measure of amorphous stability. However, T_g of a material is an indicator of thermal stability. A higher T_g is expected to have higher crystallization temperature. Thus, T_g values are reported in the reference material database (Table 2.3) . This research utilizes previous work from both BMG and thin-film literature to analyze the thermal stability since both systems are constrained by the same kinetic and thermodynamic phenomena.

Analysis of Table 2.3 shows that amorphous metals with the highest T_g all have a refractory metal as a primary constituent. It has been noted by several authors that T_g scales with the primary element's melting point in the alloy [91, 97]. Ta- and Mo-based alloys (Materials 1 to 6) all have T_g values over 700 °C. Additionally, Ta-W based alloys (Materials 7 to 13), such as Ta-W-Si-C and W-Ta-Si-B, increase T_g to values of 800 °C and higher. The most stable materials are reported in Material 12, where 'Metal 1' and 'Metal 2' are different refractory metals, achieve glass transition temperatures approaching 1200 °C. When comparing $Zr_{55}Cu_{10}Al_5Ni_{30}$ or $Zr_{63}Cu_{18}Al_{10}Ni_9$ to $Ta_{55}Zr_{10}Cu_{10}Al_{10}Ni_{15}$, a large increase of 150 °C in T_g occurs due to the addition of Ta. This large change is due to the refractory

metal becoming a dominant element in the composition. As Table 2.3 demonstrates, T_g can be greatly increased through the use of a refractory element as a primary component.

Table 2.3 also shows a trend of increasing thermal stability through the use of multiple elements with differing atomic sizes, thus increasing T_g. The Mo-based alloys (Materials 4 to 6) show a 70 °C increase in T_g by adding three more elements to the alloy. The authors specifically chose Ta, Zr, and Fe in order to achieve a distribution of sizes. They attribute this wide size distribution to the observed rise in T_g [91]. Similarly, a 10 °C increase in T_g is obtained when adding a small percentage of Ta, to $Zr_{63}Cu_{18}Al_{10}Ni_9$, creating $Zr_{58.8}Cu_{16.8}Al_{10}Ni_{8.4}Ta_6$ [96]. As seen from these examples, T_g can be increased by using more components and by selecting elements of varying atomic radii.

A large negative heat of mixing between elements promotes thermal-stability and increases T_g. The author's specifically included Si when designing Materials 4 to 6 due to Si having a large negative heat of mixing with respect to the other elements in the alloy [85, 91]. They cite the large negative heat of mixing as a promoter of thermal stability, increasing T_g [91]. The Pd-Cu-Si compositions (Materials 17 to 20) show a higher T_g with increasing Si content. There is a high negative heat of mixing between Si and many metals [85]. Finally, Li *et al*. investigated the heat of mixing relationship to T_g in ternary amorphous metals. They found that changing the elemental ratio of a given composition such that it increases the calculated heat of mixing leads to an increase in T_g.

2.2.6 Amorphous Metal Thermal Design Conclusions

Design guidelines to create thermally stable AMTFs can now be formulated. The resultant film should meet the following criteria,

- The amorphous metal should be composed of three or more elements with the major element being a refractory metal.
- The constituent elements should have a wide distribution of atomic radii, with at least a 12% difference in size between any two elements.
- There should be a large negative heat of mixing among each of the components.
- At least one of the components should be a metalloid, such as Si.

The following AMTF material systems have been formulated using these guidelines and are explored in this study: $Ta_{40}Ni_{40}Si_{20}$, $Ta_{40}Hf_{40}Si_{20}$, $Ta_{40}Mo_{40}Si_{20}$, $Ta_{40}W_{40}Si_{20}$, $Ta_{30}W_{50}Si_{20}$, and $Ta_{30}W_{30}Si_{40}$. The first offers a wide size distribution. The latter compositions contain two refractory metals. While all of the systems contain Si, the final system explores increasing Si in the composition.

2.3 Amorphous Metal Electrodes

The surface roughness of an electrode impacts the electrical performance of a thin film electronic device such as a metal-insulator-metal (MIM) diode or MIM capacitor. An increase in surface roughness leads to a non-uniform electric field in the device. As a result, the non-uniform electric field creates non-uniform current-voltage behavior in MIM diodes or increases the leakage current in a MIM capacitor.

Recent amorphous metal thin-film research has involved the use of an amorphous metal electrode for their ultra-smooth surfaces [19, 24, 25, 20, 21, 22, 23]. Since an amorphous metal surface is atomically smooth, it aids in the creation of an ideal metal-insulator interface with uniform electrical field. Amorphous metal gate electrodes have been investigated for silicon microelectronic applications in order to obtain consistent electrical prop-

erties and to reduce threshold voltage shifts [24, 25]. An amorphous metal has also been implemented as a bottom electrode for MIM tunneling diodes [19, 20, 21, 22, 23].

2.3.1 Electrical Conduction in Metals

Electrical conduction in a metal involves the flow of electrons giving rise to an electrical current. Conduction in a crystalline metal is more straightforward and is described first. Electrons in a crystalline metal are able to move freely through the metal, similar to the case of a free electron. In a crystalline metal, conduction is often described using the Drude model in which the conductivity, σ $[\Omega^{-1} - cm^{-1}]$, is given by [100],

$$\sigma = \frac{1}{\rho} = \frac{nq^2\tau}{m^*}, \tag{2.7}$$

where ρ $[\Omega - cm]$ is the resistivity, n $[cm^{-3}]$ is the electron density, q $[C]$ is the electronic charge, τ $[s]$ is the average momentum relaxation time, and m^* is the electron effective mass. τ is a key parameter for electron conduction because it relates the mean free path of the electron to the electron velocity at the Fermi surface [100]. The mean free path, l $[cm]$, is given by,

$$l = v\tau, \tag{2.8}$$

where v $[cm - s^{-1}]$ is the electron velocity at the Fermi surface. The long-range order of a crystalline metal gives rise to a mean free path much greater than the inter-atomic spacing. In other words, $l >> a$ where a is the atomic spacing.

τ is precisely defined as the average momentum relaxation time. However, it is more easily understood as the mean time between scattering events. Scattering of electrons can occur due to phonons, impurities, or other interactions. If the number of scattering events increases, there is a decrease in τ, and correspondingly an increase in resistivity. Also, as

the temperature increases, more phonons are generated in a crystalline metal, increasing the scattering rates and causing an increase in resistivity. This results in a positive thermal coefficient of resistivity (TCR) and is a defining feature of a crystalline metal [101].

While Eq. 2.7 is sometimes employed for transport assessment in an amorphous metal, conduction in an amorphous metal is different to that of a crystalline metal. Because of the lack of long-range order, τ is shorter and l is approximately equal to a, or $l \sim a$. Thus, the resistivity of an amorphous metal is typically much larger than for a crystalline metal. For example, using Eq. 2.7 and Eq. 2.8, the mean free path for a $Cu_{60}Ti_{40}$ amorphous metal with a resistivity of 190 $\mu\Omega - cm$ results in a mean free path of 0.4 nm [101]. This very short mean free path is sometimes referred to as involving the weak localization of electrons [101]. The amorphous structure and weak localization alters the behavior of the thermal coefficient of resistivity (TCR) in comparison to that of a crystalline metal. The Mooij correlation, named after its discoverer, uses a critical room temperature resistivity value to predict the TCR trend of a metal. The Mooij correlation predicts that a metal with a room temperature resistivity greater than (less than) 150 $\mu\Omega - cm$ possesses a negative (positive) TCR [100, 101]. The magnitude of the TCR of an amorphous metal is much smaller than that of its elemental crystalline components. For example, a $Cu_{50}Zr_{50}$ amorphous metal possesses a TCR of -1×10^{-4} $[K^{-1}]$ [101] while a Cu polycrystalline metal possess a TCR of $+39 \times 10^{-4}$ $[K^{-1}]$ [102].

These amorphous metal electrical conduction considerations provide a simple method to evaluate the microstructure of a metal thin film. The magnitude of the room temperature resistivity provides an indicator of whether a metal is crystalline or amorphous. In the course of AMTF research conducted at Oregon State University it has been determined that

if the resistivity is approximately 200 $\mu\Omega - cm$, then the metal is likely to be amorphous. Additionally, if the TCR is small and negative, the metal is likely to be amorphous.

An amorphous metal typically has a higher resistivity than that of a crystalline metal, which is not ideal for most electronic applications. A higher resistivity leads to higher joule heating losses and limits operating speeds. The operating frequency, f $[Hz]$, is often established as an RC time constant [49], i.e.,

$$f = \frac{1}{RC}, \tag{2.9}$$

where R $[\Omega]$ is resistance and C $[F]$ is capacitance. An increase in R lowers the operating frequency.

The higher resistivity of an amorphous metal is ideal for TIJ resistor applications while being a serious liability in terms of high-speed electronic applications. The higher resistivity of an amorphous metal is in the lower range of desired resistivities for a TIJ resistor. Even after accounting for high frequency concerns, the ultra-smooth surface of an amorphous metal offers a great advantage and opportunity for high-speed applications, enabling ideal surfaces to fabricate devices such as a MIM tunnel diode.

2.3.2 Two-Terminal Devices

A two-terminal device consists of two electrodes, or metal contacts, and a medium to achieve the desired effect. Common two-terminal devices are capacitors, resistors, and diodes. A capacitor is a charge storage device, and is typically fabricated as two metal plates separated by an insulator. Ideally, no current flows between the two electrodes and is characterized by capacitance versus voltage measurements. I-V characterization is used to evaluate leakage current and associated mechanisms. Unlike a capacitor, a resistor and a diode are both solely characterized by current flow between electrodes. Figure 2.9 (a) shows the ex-

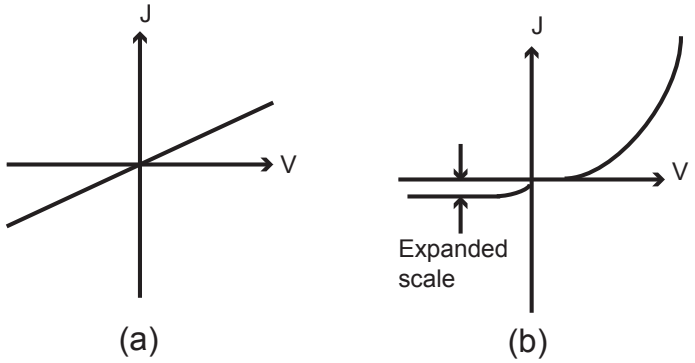

Figure 2.9: (a) A linear current density-voltage (J-V) response, characteristic of a resistor. (b) A non-linear J-V curve, characteristic of a diode. The reverse current scale is enhanced in order to illustrate the idealized reverse current trend.

pected current density-voltage, J-V, relationship for a resistor and a diode in Fig. 2.9 (b). A resistor follows Ohm's law and has a linear relationship between current and voltage. A diode exhibits a non-linear relationship between current and voltage. The non-linear characteristics of a diode are commonly used in rectification applications.

2.3.3 MIM Diodes

Different types of diodes exhibit different types of J-V curves. The J-V characteristics of a perfect diode are shown in Fig. 2.10 (a). Infinite current flows at a positive bias, while zero current flows at a negative bias [49]. The ideal diode J-V curve shown in Fig. 2.10 (b) possesses a small reverse current at negative voltages and much larger currents at positive voltages. According to ideal diode theory [49, 103, 104],

$$J = J_0 \left[exp\left(\frac{qV}{k_{\mathrm{B}}T}\right) - 1 \right], \tag{2.10}$$

where J [$A\ cm^{-2}$] is the current density, J_0 [$A\ cm^{-2}$] is the reverse saturation current density, q [C] is the electron charge, V [V] is the applied voltage, T [K] is the temperature, and k_B [$J\ K^{-1}$] is Boltzmann's constant. The MIM tunneling diode J-V behavior shown in Fig. 2.10

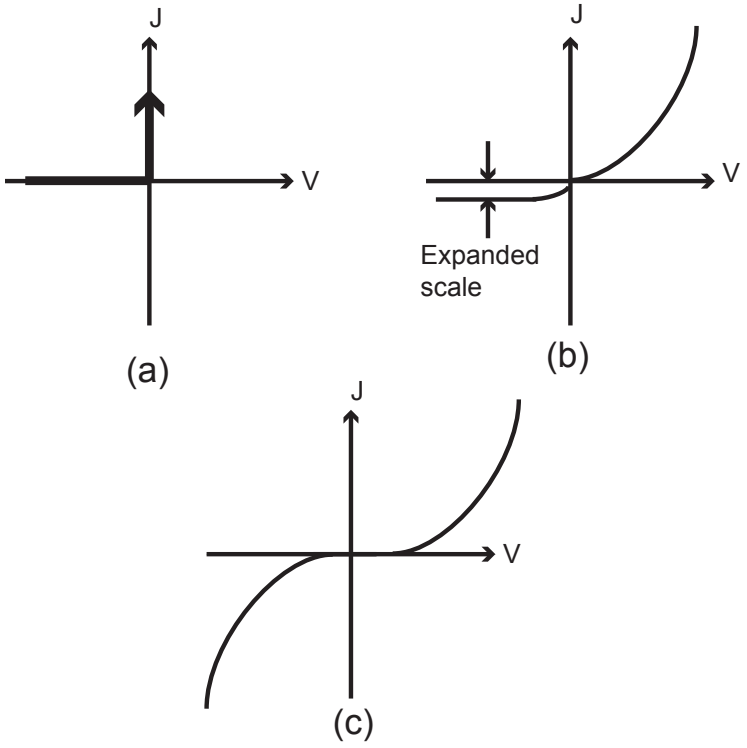

Figure 2.10: (a) Perfect ideal diode current density-voltage (J-V) curve. (b) Ideal J-V curve. The reverse current scale is enhanced in order to illustrate the idealized reverse current trend. (c) Ideal MIM tunneling diode J-V curve.

(c) is distinctly different since appreciable conduction occurs for both polarities. The J-V characteristic of a MIM tunneling diode are given by the Fowler-Nordheim equation [103, 105],

$$J = \frac{C_1 \xi^2}{\phi_{ox}} \exp\left(\frac{-C_2 \phi_{ox}^{\frac{3}{2}} \sqrt{m^*}}{\xi}\right), \tag{2.11}$$

where ϕ_{ox} $[eV]$ is the oxide barrier height, m^* $[unitlesss]$ is the effective mass, C_1 $[A\ cm^{-2}]$ and C_2 $[V\ cm^{-1}]$ are constants and ξ $[V\ cm^{-1}]$ is the applied electric field.

A MIM tunnel diode possesses some advantages compared to a conventional diode. A conventional diode is typically a bipolar semiconductor device (a p-n junction) in which both electrons and holes participate in electron conduction. In contrast, a MIM diode is a unipolar

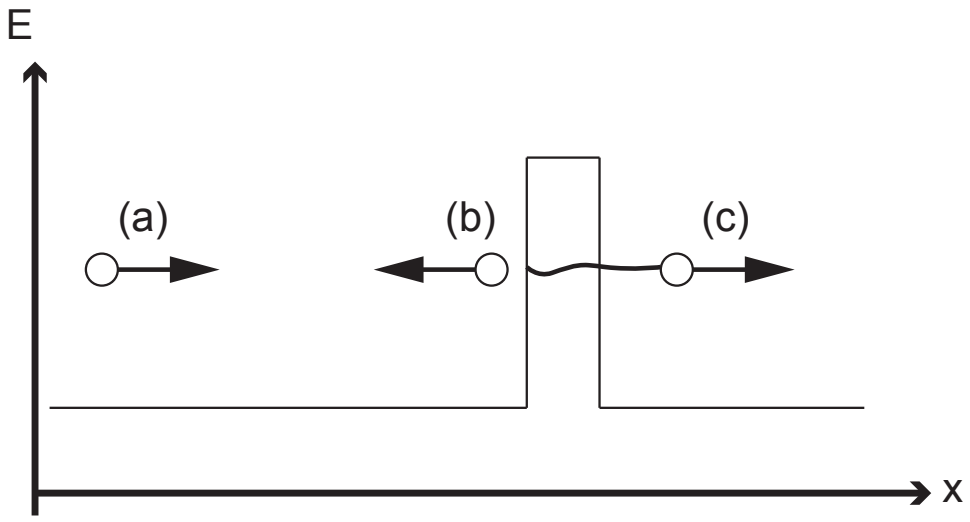

Figure 2.11: Energy (E) versus position (x) of (a) a free electron traveling towards an energy barrier, (b) a free electron reflected by an energy barrier, and (c) a free electron that has tunneled through an energy barrier.

device in which conduction depends only on electrons. A MIM diode is potentially superior to a p-n junction in terms of switching speed since it is a unipolar device. Additionally, a MIM diode is fabricated using fewer processing steps in comparison to a p-n junction which is typically fabricated via conventional silicon processing. Thus, a MIM diode may be employed in applications that are not appropriate for a p-n junction, such as large-area display backplanes [19, 106, 107].

2.3.4 MIM Tunnel Diode Conduction Mechanism

To understand the basic current conduction mechanism for a MIM tunnel diode, it is best to first consider an electron traveling in free space when it encounters an energetic barrier. Figure 2.11 (a) shows a free electron traveling along the positive x direction. Classical mechanics treats the electron as a particle and dictates that the electron is reflected from the

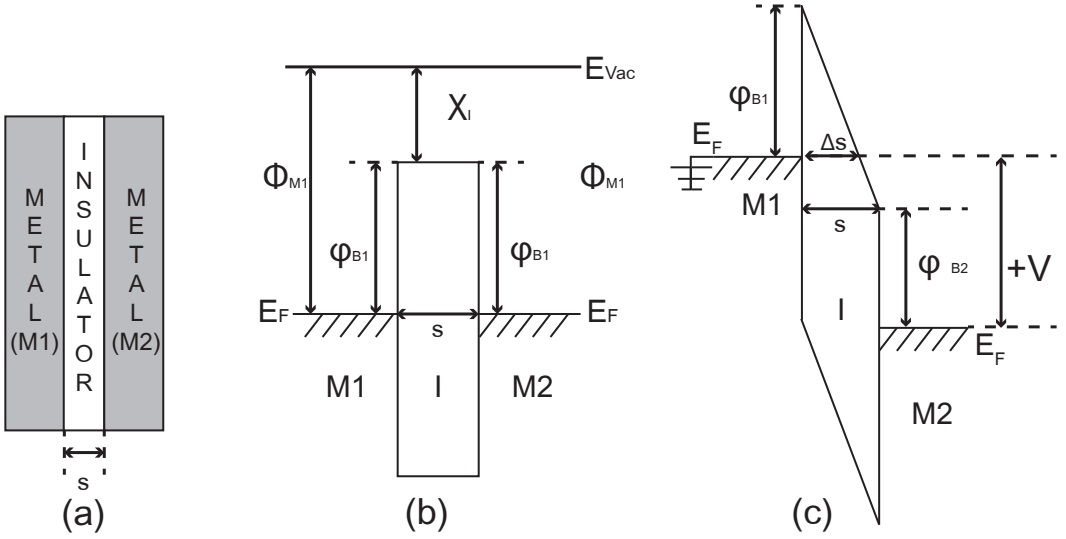

Figure 2.12: (a) MIM diode cross-section with an insulator thickness, *s*. (b) Equilibrium energy band diagram of a symmetric MIM diode with identical metal electrodes. (c) A non-quilibrium energy band diagram of a symmetric MIM diode where M2 has a large positive bias and M1 is at ground. A electron's probability of tunneling increases through Δs.

energy barrier, as shown in Fig. 2.11 (b). Quantum mechanics treats the electron as a wave with a given wavelength [108]. As a result, an electron encountering a barrier has a finite probability of penetrating through a barrier, shown in Fig 2.11 (c). This phenomena is known as quantum mechanical tunneling. By decreasing the thickness of the barrier or the barrier height, the tunneling probability of the incident free electron increases.

The primary mechanism for current conduction in a well-designed MIM diode is tunneling. As opposed to the free electron energy diagram shown in Fig. 2.11, the energy barrier is established by the insulator in a MIM tunnel diode. The probability of tunneling is dictated by the insulator thickness, *s*, and the average barrier height with respect to the metal Fermi level. Figure 2.12 (a) shows the construction of a MIM diode. As the thickness of the insulator increases the probability of tunneling significantly decreases. Thus, for a large value of *s* and common operating voltages the MIM diode transitions into a MIM capacitor.

Figure 2.12 (b) shows an equilibrium energy band diagram of a symmetric MIM diode where the metal work functions of M1 and M2 are equal. Energy band diagram shown in Fig. 2.12 represents material properties (work function, electron affinity, and ionization potential) and provide an intuitive picture of transport through a MIM diode. For a symmetric diode, a rectangular barrier is formed where electron traveling from M1 to M2 faces the barrier ϕ_{B1} and an electron traveling from M2 to M1 faces an equal barrier ϕ_{B2} . Using the energy band diagram from Fig. 2.12, ϕ_{B1} and ϕ_{B2} can be expressed as,

$$\phi_{B1} = \phi_{B2} = \phi_{\mathrm{M1}} - \chi_I = \phi_{\mathrm{M2}} - \chi_I \tag{2.12}$$

where χ_I $[eV]$ is the electron affinity of the insulator, and ϕ_{M1} and ϕ_{M2} $[eV]$ are work functions of electrode M1 and M2, respectively. The barrier height needs to be sufficiently large in order to prevent thermionic emission in which energetic electrons in the Boltzmann tail of the thermal distribution surmount the barrier and contribute to appreciable current flow. The barrier height is also critical in determining the probability of tunneling from an electrode, with larger barriers heights exponentially decreasing the tunnel probability.

Figure 2.12 (c) depicts Fowler-Nordheim tunneling through a symmetric MIM diode. Here, a positive bias, V, is applied to M2 while M1 is held at ground. If a sufficient voltage is applied, the insulator begins to form a triangular barrier with an effective insulator thickness of Δs, as seen in Fig. 2.12 (c). The change in effective thickness increases the probability of tunneling. Fowler and Nordheim used the WKB approximation to solve the quantum mechanical probability of tunneling and define the current-voltage relationship as shown

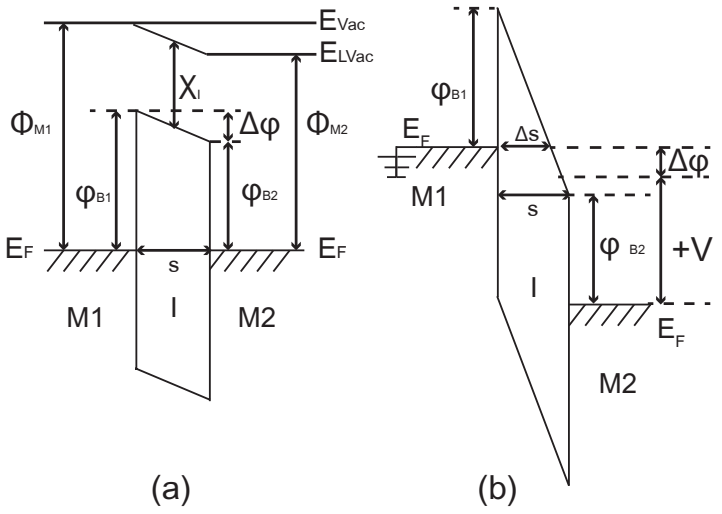

Figure 2.13: (a) An equilibrium energy band diagram for an asymmetric diode where the metal work function of the left electrode (M1) is greater than the metal work function of the right electrode (M2). (b) Non-equilibrium energy band diagram with a large positive bias applied to electrode M2 and M1 is at ground.

above in Eq. 2.11, where ϕ_{ox} is equal to ϕ_{B1}. The constants C_1 and C_2 are defined as:

$$C_1 = \frac{q^2}{8\pi h} = 1.54 \times 10^{-6} \frac{A}{V^2}, \tag{2.13a}$$

$$C_2 = \frac{8\pi q^{\frac{3}{2}} \sqrt{2m_0}}{3hq} = 6.85 \times 10^{7} \frac{V}{cm}, \tag{2.13b}$$

where h is the Plank's constant [$J\ s$], m_0 [kg] is the rest mass of an electron, and q [C] is the charge of an electron.

Simmons considered tunneling of an asymmetric MIM diode where the work function of M1 is different to that of M2, as shown in Fig. 2.13 (a) [103, 109, 110]. Similar to the symmetric case, the barrier is defined as the difference of the metal work function and the insulator electron affinity, i.e $\phi_{B1} = \phi_{M1} - \chi_I$ and $\phi_{B2} = \phi_{M2} - \chi_I$. For an asymmetric MIM diode under equilibrium, work functions of the two electrodes align to develop a zero-bias potential across the insulator, as shown in Fig. 2.13 (a). The zero-bias potential, or built

in field, across the insulator forms a trapezoidal barrier, as seen in Fig. 2.13 (a). Simmons accounts for the trapezoidal barrier with a new term, $\Delta\phi$, which is defined as,

$$\Delta\phi = \phi_{B2} - \phi_{B1} = \phi_{M2} - \phi_{M1}. \tag{2.14}$$

It is evident that in a symmetric diode $\Delta\phi = 0$ eV.

Similar to the Fowler-Nordheim equation, Simmons developed a general expression for calculating the tunneling current in an asymmetric MIM tunnel diode by solving for the tunnel probability using the WKB approximation incorporating $\Delta\phi$ [103, 109, 110]. For the case of a positive bias applied to M2 with M1 grounded, an electron travels from M1 to M2 and the barrier seen is ϕ_{B1}, as seen in Fig. 2.13 (b). Simmons found the positive polarity current density to be given as [110],

$$J = \frac{C_3\left(\xi + \Delta\phi\right)^2}{\phi_{B1}} \exp\left(\frac{-C_4\phi_{B1}^{\frac{3}{2}}\sqrt{m^*}}{(\xi + \Delta\phi)}\right). \tag{2.15}$$

For the case of a negative potential applied to M2, an electron travels from M2 to M1 and the barrier seen is ϕ_{B2}.The current density is given as [110],

$$J = \frac{C_3\left(\xi + \Delta\phi\right)^2}{\phi_{B2}} \exp\left(\frac{-C_4\phi_{B2}^{\frac{3}{2}}\sqrt{m^*}}{(\xi + \Delta\phi)}\right). \tag{2.16}$$

It is important to that note the sign of $\Delta\phi$ remains the same in both equations. Simmons derivation results in new constants C_3 and C_4 defined as,

$$C_3 = \frac{2.2q^2}{8\pi h} = 3.39 \times 10^{-6}\frac{A}{V^2}, \tag{2.17a}$$

$$C_4 = \frac{8\pi\sqrt{2m_0}q^{\frac{3}{2}}}{2.96hq} = 6.96 \times 10^{7}\frac{V}{cm}, \tag{2.17b}$$

where h is the Plank's constant [$J\ s$], m_0 [kg] is the rest mass of an electron, and q [C] is the charge of an electron.

Equations 2.11, 2.15, and 2.16 provide a quantitative description of current flow through a MIM diode when Fowler-Nordheim tunneling dominates. The result of Simmons yields a similar result to the reported Fowler-Nordheim equation with slight variation to the constants and the additional $\Delta\phi$ term. In the quantitative equations, there is no temperature dependence for F-N tunneling. Acquiring current-voltage data from a device at multiple temperatures should result in no change in the tunnel current and should be assessed to confirm the conduction mechanism. Finally, these equations demonstrate how material properties can influence MIM current conduction. For example, increasing the barrier height or insulator thickness reduces the current.

3. EXPERIMENTAL TOOLS AND TECHNIQUES

This chapter describes the experimental tools and analytical characterization techniques utilized in this research. This chapter is divided into three sections: amorphous metal thin film (AMTF) development, thermal inkjet (TIJ) resistor development, and metal-insulator-metal (MIM) device fabrication and characterization. AMTF development includes sputter deposition of an AMTF and the associated materials characterization used to determine the thin film structure and stability. Next, TIJ resistor development discusses process integration of an AMTF into a TIJ resistor, development of a TIJ resistor test platform, and testing methodology. Finally, MIM device fabrication and characterization presents the fabrication steps to build a MIM device and the electrical characterization techniques utilized for this research.

3.1 Amorphous Metal Thin Film Fabrication

3.1.1 Sputter Deposition

All AMTFs are fabricated using sputter deposition. Sputtering parameters and deposition conditions play a key role in determining resulting properties of the film. It is necessary to understand key components of sputtering to relate measured properties and processing conditions. DC and RF magnetron sputtering are used to create the AMTF and are described below.

Sputtering is a physical vapor deposition process that utilizes energetic ions to remove atomic material from a target [111]. Figure 3.1 shows the basic components (plasma, target and substrate) of a sputtering system. Energetic ions are created in the plasma and are attracted to the target. An attracted ion can strike the target with sufficient energy to eject

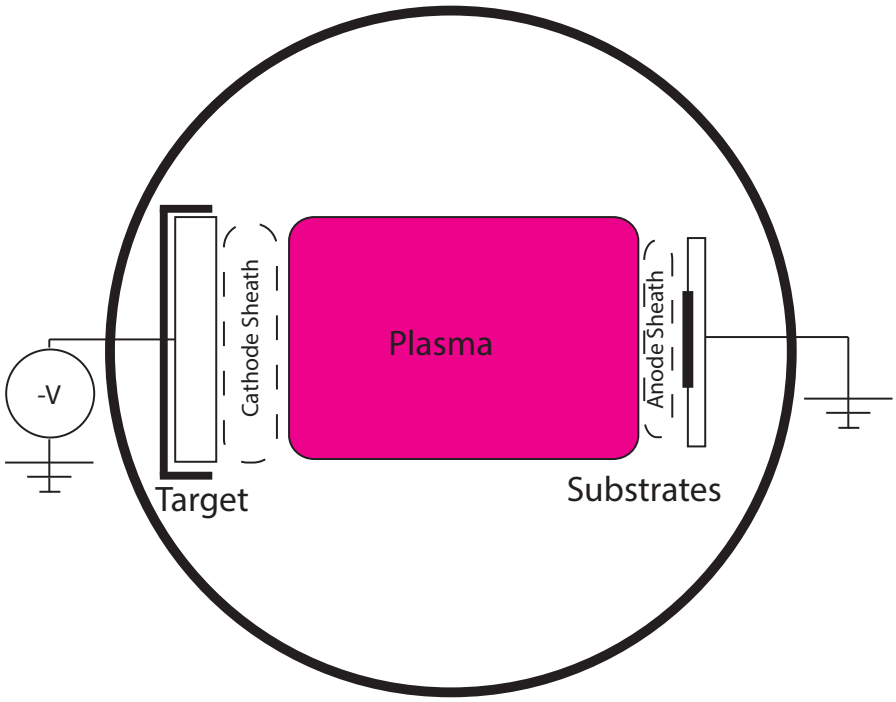

Figure 3.1: The basic components in a sputtering system.

a target atom. A flux of atoms is created from multiple ions hitting the target. This flux of atoms travels from the target to the substrate forming a thin film of target material. Figure 3.1 shows two additional important regions; the cathode sheath, between the target and plasma and the anode sheath, between the substrate and plasma.

A sputtering system requires a high vacuum and the capability to maintain a medium vacuum environment. High vacuum is needed to remove any contaminants, preventing unintentional species incorporating into the AMTF. A medium vacuum is required to create and sustain the plasma. This is accomplished through introducing a *process gas*, such as Argon (Ar). A medium vacuum also provides an environment in which an atom ejected from the target can travel to the substrate with minimal collisions. This requirement is related to the

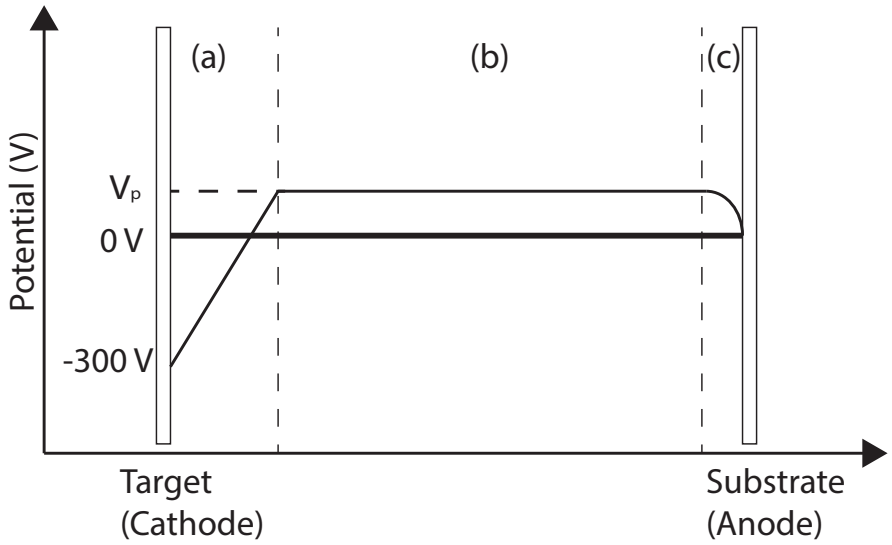

Figure 3.2: A typical voltage distribution across a sputtering chamber.

mean free path of the atom. The mean free path is the average distance a species travels before colliding with another atom or molecule and is inversely proportional to pressure. A short mean free path indicates an increase in collisions and reduces the film growth rate.

The sputtering process is driven by the potential distribution in the chamber. Figure 3.2 shows the voltage distribution across the sputtering chamber from the applied bias on the target. Region (a) of Fig. 3.2 shows a large change in potential from the bias on the target to the plasma. This region is the cathode sheath which constitutes a dark space region. A dark space is an area where no plasma exists. The large potential difference between the target and the plasma is the most important region of the sputter process [111]. The large negative potential on the target creates a flux of electrons repelled from the bias. An electron possessing enough kinetic energy ionizes an Ar atom. The ionized Ar atom has a positive charge and accelerates to the target, bombarding the surface and creating the sputtering process of ejecting target

atoms. This can be visualized by imagining billiard balls colliding [112]. The ejected atom travels through the chamber, as discussed above. Region (b) of Fig. 3.2 is characterized by a constant potential of the plasma, referred to as the plasma potential V_p. This is typically taken to be 15 V [113]. In this region repelled electrons are accelerated with enough energy to excite an Ar atom to a higher energy state. As the Ar atom returns to its ground state, a photon is emitted, giving rise to the color associated with the plasma. Region (c) of Fig. 3.2 shows the anode sheath and grounded substrates. The anode sheath is a dark space but it is considerably smaller due to the much smaller change in potential from V_p to the target.

Secondary electron emission is critical to sustain the plasma and ionization process. Secondary electron emission is the process of producing additional free electrons in the chamber. They are created through various means. In addition to the ejected atoms from the target, the bombarding ions create these secondary electrons. This is the major source of secondary electrons [111]. The number of secondary electrons generated by the target varies per target material and alloy [112]. The Ar ionization process creates a cascading reaction generating additional secondary electrons. Lastly, secondary electrons are also generated by the chamber walls, substrate and other system components.

Magnetron sputtering is commonly used to increase the efficiency of ionized gas atoms near the target surface. Magnetron sputtering utilizes a rare earth magnet behind the target. This creates a magnetic field and Lorentz Force near the target trapping electrons in a localized area, resulting in an increased probability of ionization of gas atoms. This increases the sputtering rate and allows the process to occur at lower pressures [111]. At a low pressure, the mean free path increases and ejected target atoms maintain high energy when the arriving at the substrate. This is known a *ballistic sputtering* process.

There are two primary types of sputtering systems, DC and RF. In a DC system, a set potential is applied to the target as shown in Fig. 3.1. The target must be conductive to continually neutralize the Ar ions that strike the surface. An insulating target will not work in a DC system. A positive charge forms on the target surface from the Ar ions, as the ions build on the target surface and the plasma cannot be maintained [112]. For an insulating target, an RF system must be used. RF sputtering overcomes this issue by applying an alternating potential to the target. The power supply operates at a high frequency, typically 13.56 MHz, which pulses to a small positive potential [113]. At these high frequencies, ions are slower to respond to the change in potential and the electrons are attracted to and neutralize the target surface. This sustains the plasma. In RF sputtering, a power matching network is used to assure the applied power is not lost in the transmission line [111, 112].

This research uses multi-component pressed metal targets purchased from Kamis and Materion. The amount of energy required to remove material from the target depends on the material. A higher sputter yield indicates less energy is required to remove an atom [112]. When using an multi-component target, the resulting film maintains stoichiometry even though each constituent atom may have different sputtering yields [111]. The uniformity is maintained by the depletion of higher yielding atoms at the surface, increasing the ratio of the lower yielding element. This relative increase allows the balance of lower sputter yielding elements to occur [111].

The TANG sputtering system in the Oregon State University Materials Synthesis and Characterization (MaSC) cleanroom facility is used to create the AMTF in this research. The TANG utilizes 2 inch US-Inc MAK guns for the sputtering sources. It operates at a base pressure of 5 x 10^{-8} Torr. The films are sputtered at pressures between 3 to 15 mTorr using

Argon gas flowing at 20 standard cubic centimeters per minute. The power is varied between 50 W RF to 100 W RF and 35 W DC to 60 W DC.

3.2 Amorphous Metal Thin Film Characterization Techniques

A careful and consistent approach to thin film characterization is the basis of determining if an AMTF is compatible with the TIJ environment. First, the development and fabrication of a high temperature amorphous metal for TIJ relies on the ability to characterize the structure of the AMTF, especially the transfer from an amorphous state to a crystalline metal. Second, understanding of chemical stability and passivation mechanisms are needed for TIJ compatibility. This section details the experimental method and thin film characterization techniques used for structural determination and chemical composition. These techniques are used before and after an experimental procedure to determine physical changes in the thin film.

3.2.1 Annealing Techniques

Determination of the crystallization temperature requires a methodical annealing process. Samples are annealed at a starting temperature and then evaluated with x-ray diffraction (XRD) and atomic force microscopy (AFM). If the results show the film remains amorphous, samples are annealed at a higher temperature. This process is repeated until the XRD pattern and AFM surface roughness show results indicative of crystalline material. The film is stable up to the highest temperature where the XRD and AFM data support an amorphous structure.

Oxidation occurs when annealing a metal in the presence of oxygen. At lower temperatures, a thin surface oxide is created. As the temperature increases, the oxide penetrates into the film consuming more of the metal film. It is possible to oxidize the thin film where char-

acterization results are from the oxide and not the intended film. To prevent oxidation from influencing results, a controlled environment is desired. A vacuum sealed tube provides an oxygen limited environment to prevent the film from complete oxidation. All crystallization tests are performed in a sealed tube anneal. Kris Olsen in the Oregon State Chemistry department performed the testing, sealing the tubes at approximately 50 mTorr. Anneals are held at temperature for 15 minutes and are tested in increments of 100 °C until the crystallization temperature is found.

3.2.2 Oxidation Testing

Chemical stability testing is achieved through an atmospheric annealing study. Selected AMTF compositions and a Ta reference thin film are annealed at 300, 500, and 700 °C for numerous set times. After the annealing process, the thin film structure and surface will be evaluated for structural and mechanical stability through AFM, XRD, and scanning electron microscopy (SEM) characterization. Any surface oxide that forms will be evaluated for thickness via ellipsometry, x-ray reflectivity (XRR), and transmission electron microscopy (TEM) characterization. Finally, the chemical composition of the oxide will be analyzed through depth profiling x-ray photoelectron spectrometry (XPS) to determine the passivation mechanisms.

3.2.3 Atomic Force Microscopy

Originally created to examine the surfaces of insulating materials, atomic force microscopy (AFM) is an analysis technique which provides thin film surface feature information, such as root-mean-squared roughness and peak roughness of the film [105]. These features are typically the material grains and grain boundaries. An amorphous metal lack

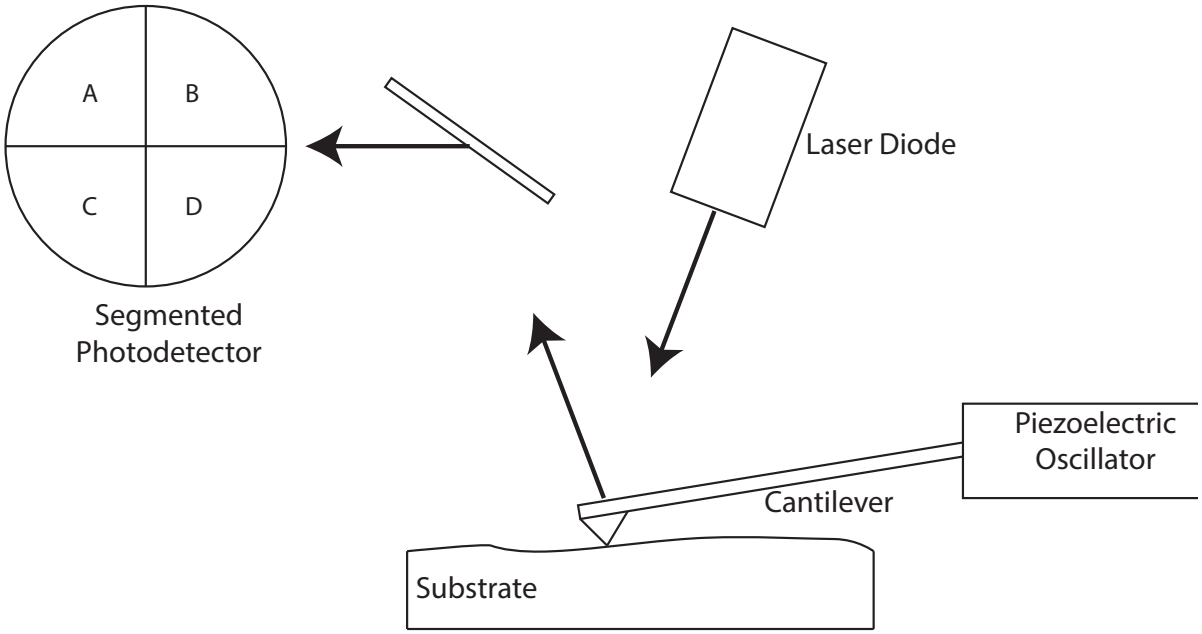

Figure 3.3: A schematic illustration of an AFM system.

these grains and has an atomically smooth surface. Many amorphous metals have reported less than one nanometer average roughness [19, 114].

An AFM system consists of a cantilever with a sharp tip, a piezoelectric oscillator, a laser diode and a segmented photodector, as seen in Fig. 3.3. The cantilever is small and narrow, usually 100 μm long, 20 μm wide, and 0.1 μm thick, made from silicon or silicon nitride [105]. The cantilever's tip moves along the surface with a known force between itself and substrate controlled by the piezoelectric oscillator. The laser diode reflects light from the tip of the cantilever to the photodector. As the tip moves across the surface, the reflected light moves to different quadrants of the photodector as it is deflected by surface peaks or valleys. AFM can detect sub-nanometer changes in the surface of the film [115].

There are three modes of operation: contact, non-contact, and tapping mode. In contact mode, the tip is put into contact with the surface of the film. It creates a topographic map

of the surface as it moves along the the surface through the detection of the laser, as described above. This method damages the tip quickly and requires constant tip replacement. In non-contact mode, the tip is brought close to the surface to sense van der Walls forces from the surface. Due to the weaker forces, the tip is provided a small oscillation and an AC detection method is used to provide the measurement. Non-contact mode provides lower resolution than contact mode [105]. Finally, tapping mode taps the surface by lightly placing the tip into contact with the surface, then lifts the tip away from the surface, and moves to the next surface location. The piezoelectric oscillates the cantilever at its resonant frequency, generally 50 to 500 kHz, and limits the oscillating amplitude from a feedback loop of the force between the tip and the surface. The amplitude of the oscillation provides the topographical information of the surface. If there is a depression, the amplitude increases. If there is a peak, the amplitude decreases. The tapping prevents the tip damage and provides better resolution than the non-contact mode.

The AFM measurements in this work are taken using an Asylum MFP-3D AFM system in the Oregon State University Material Science department courtesy of Dr. Brady Gibbons. Unless otherwise specified, the measurements are performed in contact mode with silicon Vista Probe tips.

3.2.4 X-ray Diffraction

X-ray diffraction (XRD) is an analytical technique utilizing scattered x-rays to determine the structural properties of a material. Since the wavelength of x-rays (Cu Kα λ = 1.54 $\mathring{A}$ [9]) is comparable to the inter-atomic spacing of atoms, they are used to determine structure properties. An impinging x-ray give rise to one of three processes to conserve kinetic energy when interacting with a material. X-ray energy can inelastically create photoinozia-

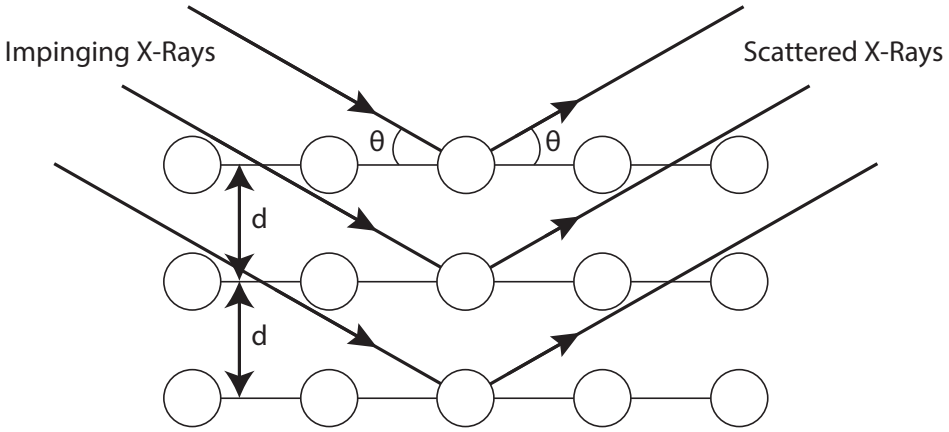

Figure 3.4: A schematic illustration of x-rays scattered from a plane of atoms.

tion, energy can inelastically transfer to an electron, or it can undergo Thomson scattering from an atom. Thomson scattering is an elastic scattering event and is crucial to the XRD measurement [9]. XRD detects the intensity of the Thomspon scattered x-rays diffracted at different angles.

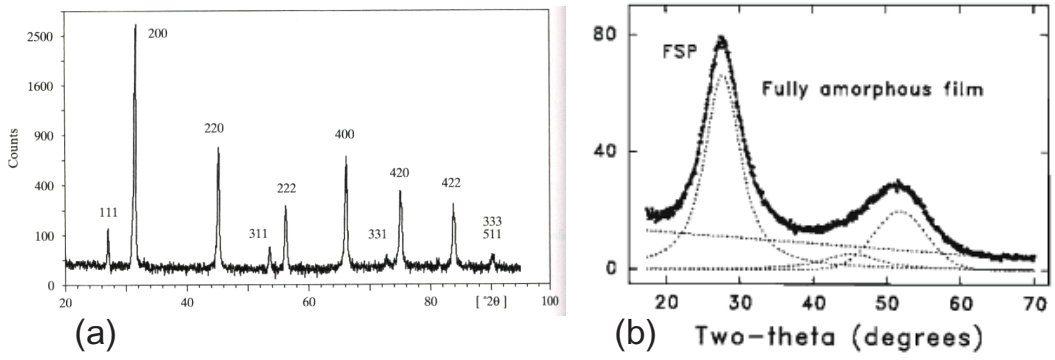

Figure 3.5: (a) A crystalline XRD diffraction pattern of a NaCl sample [8]. (b) Characteristic diffraction pattern of an amorphous silicon sample [9].

Figure 3.4 shows a two dimensional pattern of atoms where θ is the angle of the impinging and scattered x-rays, and *d* is the spacing between atomic planes in reciprocal lattice space. At different angles of θ, an x-ray travels different distances in the material before reflecting (scattering) from a plane of atoms. The difference in the path length changes the x-ray phase as it leaves the material resulting in constructive (in-phase) or destructive (out of phase) interference. A special case of *d* and θ allow for constructive interference, creating peaks in the diffraction pattern of a material. This can be described by Bragg's Laws as,

$$2 \times d \times sin(\theta) = n \times \lambda, \tag{3.1}$$

where θ is the incident angle, *d* is the separation between planes and λ is the wavelength of the incident x-ray. This is similar to the diffraction of light through a diffraction grating [8]. Constructive interference gives rise to peak intensities in an XRD pattern.

An x-ray diffraction pattern depends upon the material's atomic structure. Figure 3.5 (a) depicts an example XRD pattern of a crystalline structure. Each peak in the measurement intensity corresponds a Bragg reflection from a crystal plane. Since the crystal planes are well defined, diffraction patterns result in sharp peaks due to strong reflections. On the other hand, Fig. 3.5 (b) is an XRD pattern for an amorphous silicon sample where the peaks are broad and over multiple values of θ creating a bump. In an amorphous structure, there is no long range repeating atomic structure creating atomic planes. Atoms are arranged around a central atom creating a bonding sphere. This bonding arrangement gives rise multiple reflections with the center of the broad hump corresponds to the average nearest neighbor distance in the bonding sphere [9]. In Fig. 3.5 (b), the peak at two-theta of 49° represent the nearest neighbor in a bonding sphere and the center of the peak at two-theta of 27.4° is the second nearest neighbor.

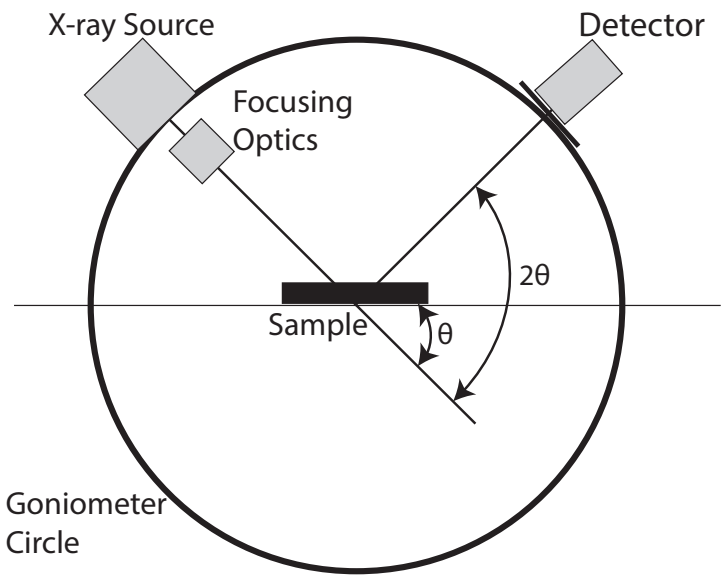

Figure 3.6: A schematic representation of an XRD system. The x-ray source and detector can both independently rotate around the sample to change the angle of incidence.

Figure 3.6 shows a typical XRD system setup and components. The system includes an *x-ray source*, *focusing optics*, a *substrate stage*, and a *detector*. The x-ray source is a metal plate, typically copper, and a cathode metal filament sealed in high vacuum. The filament creates electrons which are accelerated to the copper plate by a field, generating Kα x-rays. The focusing optics conditions the x-ray beam to focus onto the substrate placed on the substrate stage. The x-rays diffract from the sample and are picked up by the detector which measures the x-ray intensity by number of counts. Finally, two high-precision goniometers are used to move the detector and source independently, changing the incident angle and detected angle, represented in Fig. 3.6 by the goniometer circle. The focusing optics provides conditioning of the generated x-rays to change the measurement geometry. The substrate stage holds the substrate determining the substrate plane for analysis. The detector measures the intensity of the diffracted x-rays.

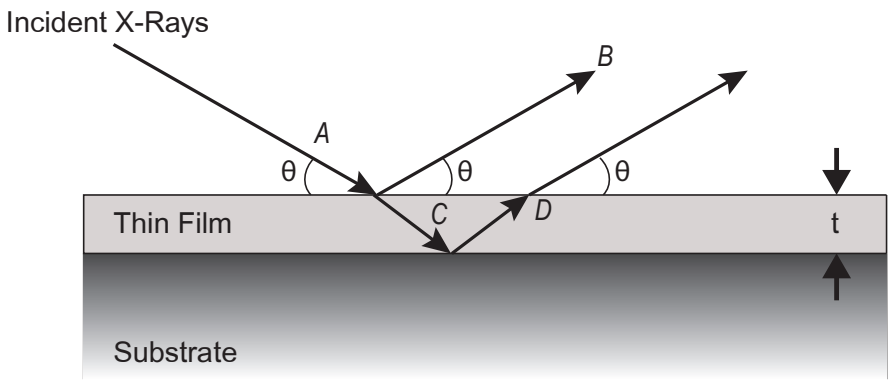

Figure 3.7: Schematic representation of reflected and refracted x-rays in a thin film during a XRR measurement [9].

A typical measurement sets the incident and detected angles equal as they sweep a range of angles. This is known as a θ-2θ measurement and is typically used to characterize bulk powder samples and single crystals. For thin films, x-rays penetrate through the sample film into the substrate resulting in difficulties in deconvoluting signals from the thin film and the substrate. A grazing incident measurement keeps the angle of incident constant at a small value and sweeps the detector angle. At a low incident angle, the x-rays graze the film and penetrate the substrate less, providing better thin film results [9]. The Rigaku Ultima IV x-ray diffractometer and Rigaku R-Axis Rapid diffractometer systems were used to obtain the XRD data for this work.

3.2.5 X-ray Reflectivity

X-ray reflectivity (XRR) is a thin film characterization technique used to calculate physical properties of a thin film structure. Figure 3.7 is a schematic representation of an

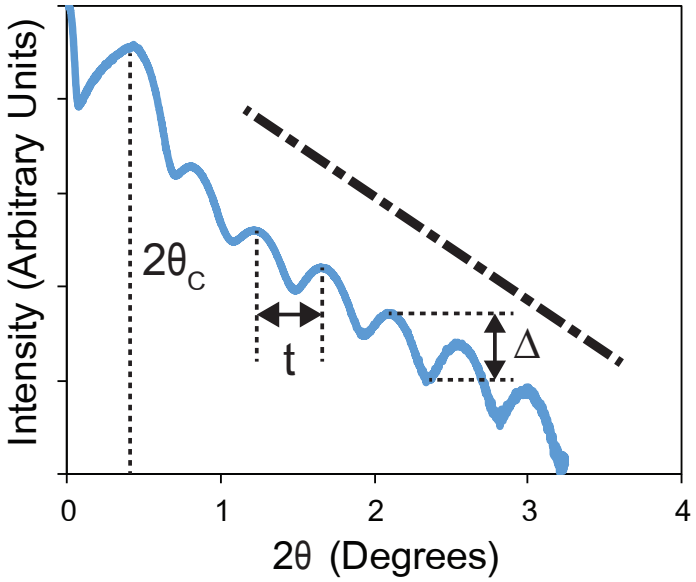

Figure 3.8: Example XRR measurement data of a 20 nm Al_2O_3 thin film on a silicon substrate annotated with the critical features, such as $2\theta_C$, that are used to model thin-film density, thickness, and roughness [9].

x-ray behavior in a XRR measurement of a single thin film on a substrate. At values of 2θ smaller than two times the critical angle ($2\theta_C$) all incident x-rays are reflected from the thin film surface, as shown by arrow B in Fig. 3.7. As 2θ increases to values greater than $2\theta_C$, x-rays begin to refract into the film, as shown by arrow C in Fig. 3.7. These x-rays are subsequently reflected by the substrate surface and exit the thin film, as shown by arrow D in Fig. 3.7. The phase of x-ray D is different than that of x-ray B due x-ray D traveling some distance through the thin film. At different angles of 2θ the phase difference between x-rays B and D occurs in a multiple of the incident x-ray wavelength [9, 116]. This creates constructive interference in the measurement data. The angles at which constructive interference occurs is depends upon the physical properties of the thin film stack, such as layer thickness, density, and interface roughness. The measurement data can be used to model each of these physical properties for each layer in the thin film stack.

Figure 3.8 is representative XRR measurement data from a 20 nm Al_2O_3 thin film on a silicon substrate. From 0 to 0.45°, indicated by the vertical dashed line in Fig. 3.8, the intensity increases due to the reflection of x-rays off of the film's surface [9, 116]. The dashed line indicates $2\theta_C$. The value of $2\theta_C$ provides the necessary information to calculate the top layer thin film density. Past $2\theta_C$ x-rays refract into the film resulting sharp drop in intensity that transitions into multiple oscillations in the intensity amplitude. The distance between oscillations in Fig. 3.8, indicated by t, is related to the thin film thickness. The difference in magnitude of the oscillations, depicted as Δ in Fig. 3.8, is influenced by the roughness and difference in density between the thin film and the substrate [116]. The slope of the measurement, indicated by the dashed line from 1.5 to 3.5° in Fig. 3.8, is dependent on the thin film roughness. As roughness increases, the magnitude of the slope correspondingly increases [9, 116, 117].

The measurement system described in Fig. 3.6 is used to carrier out an XRR measurement. The measurement is done in a θ-2θ configuration where the x-ray source and detector are set to the same angle and measurements are typically performed between 0 to 8°. The Rigaku Ultima IV x-ray diffractometer system was used to obtain the XRR data for this work. The data was modeled in Rigaku GlobalFit modeling software.

3.2.6 X-ray Photoelectron Spectrosocopy

X-ray photoelectron spectroscopy (XPS) is a surface analysis technique used to quantify the elemental composition and atomic chemical state of atoms at a material's surface. XPS uses x-rays to create photoemission of an atom's core electron, i.e., eject an electron from its core orbital. Figure 3.9 (a) is a schematic depiction of an incident x-ray creating photemission of a core *1s*, or *K* shell, electron in a XPS measurement. In Fig. 3.9 (a), a high

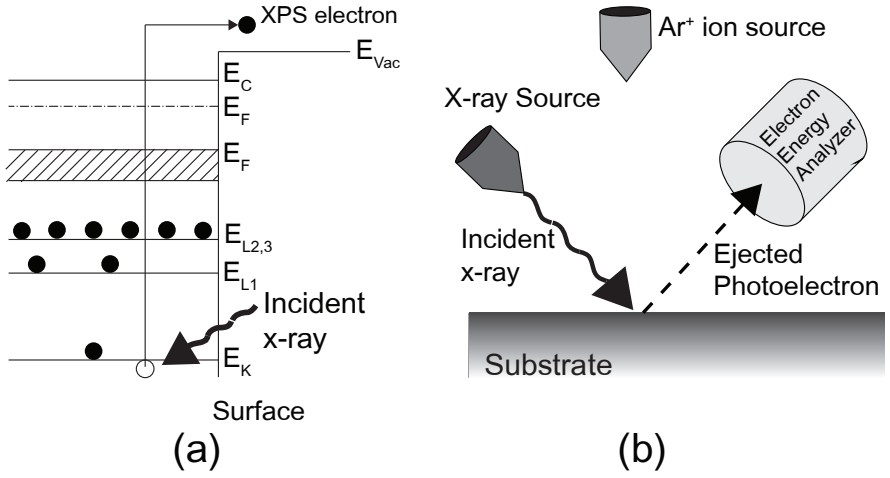

Figure 3.9: (a) X-ray photoionization of a *1s* (*K shell*) electron in a semiconductor for a XPS measurement. (b) Typical components comprising an XPS system.

energy x-ray strikes the film with enough energy to overcome the binding energy of the *1s* electron. The photoemitted electron leaves the surface and is ejected into the XPS detector at a given kinetic energy. The electron binding energy, E_B, can be calculated from the its kinetic energy, E_K, as follows:

$$E_B = h\nu - E_K - W \tag{3.2}$$

where $h\nu$ is the photon energy and W is the work function of the spectrometer [105, 118]. A plot of binding energy versus measured intensity is used to identify elemental composition and chemical state by comparing to reference patterns that are unique to each atom [105, 118].

XPS is a surface technique since only electrons ejected near the surface retain their kinetic energy from the sample to the detector. Electrons ejected from atoms deeper than 0.5 - 5 nm lose energy due to inelastic scattering as they travel towards the surface [105]. In

order to provide a compositional depth profile, the film is alternately sputtered followed by an XPS measurement through the depth of the thin film.

Figure 3.9 (b) is a schematic of the main components in a XPS system. The system consists of a high vacuum chamber (not shown), a x-ray source, an electron energy detector, and an ion source. First, a high vacuum environment must be achieved in order for the electrons to travel from the surface of the material to the detector without scattering. Next, a x-ray source is used to generate the incident x-rays needed to create photoemission. A typical x-ray source in a XPS system involves Al Kα emission, yielding an energy range between 0 - 1350 eV [118]. An electron energy analyzer is then used to measure the energy of the ejected electrons. Finally, the system may be equipped with an ion source, typically involving an Ar^+ ions, to facilitate depth profiling measurements.

XPS measurements were accomplished using a PHI Quantera Scanning ESCA by Dr. William Stickle at the HP Corvallis facility. The spectrometer was equipped with a monochromatic Al X-ray source having a photon energy of 1486.6 eV. The data were charge-corrected to carbon 1s at 284.8 eV. The binding energy (BE) scale was calibrated using the Cu $2p_{3/2}$ feature at 932.7 $\pm$ 0.05 eV and Au *4f* at 84.0 $\pm$ 0.05 eV. Composition was determined using standard elemental relative sensitivity factors corrected for the transmission function of the analyzer. Sputter depth profiles were acquired by alternately sputtering and acquiring spectral data. Samples were sputtered using a 2-kV Ar^+ ion beam with a sputter rate of 5 nm min^{-1} relative to SiO_2. The sputter depth-profile data were reduced using a linear least-squares method to separate overlap of the tantalum *4f* and the oxygen *2s* signals and to assign the chemical state of silicon to silicide or oxide [119].

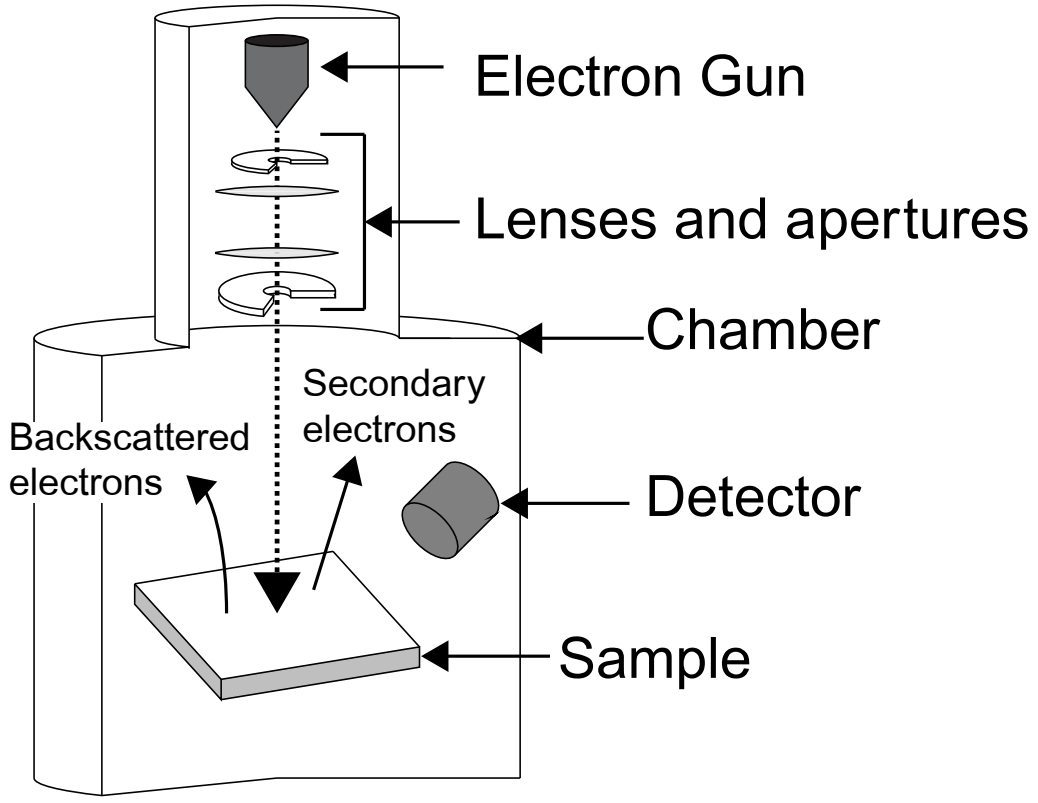

Figure 3.10: Components of a scanning electron microscope, including the electron gun, focusing lenses and apertures, detectors, and samples with example emitted electrons

3.2.7 Scanning Electron Microscopy (SEM)

Scanning electron microscopy (SEM) is a characterization technique that enables increased magnification and improved depth of focus in comparison to an optical microscope. A SEM is capable of achieving a 1 nm resolution through using high energy electrons with wavelengths of $\sim$0.055 to 0.0071 nm (in comparison to 400 nm of light). In order to create the appropriate wavelengths, electrons are accelerated at voltages between 500 V - 30 kV [120]. An increased depth of focus can be envisioned as the ability to make small features appear more three dimensional which allows surface features to be easily detectable [120]. A

SEM is used in materials science to analyze material properties such as grain size and fatigue studies. A SEM is also used in the microelectronics industry to measure device dimensions and for failure analysis studies.

Figure 3.10 is a schematic depiction of the major components in a SEM. The system must be in a high vacuum environment to enable electrons to travel between the source, sample, and detector without being scattered. An electron gun, commonly a tungsten hairpin filament or lanthanum hexaboride source, is used to generate and accelerate electrons for imaging. The generated electrons are sent through a series of lenses, apertures, and scanning coils to focus the electrons into a rastared beam. This electron beam is scanned across the surface of the sample and interacts with the material. This interaction generates secondary electrons and backscattered electrons. These electrons are then detected by the appropriate detector. Typically, secondary electrons are detected by an Everhart-Thornley detector and the backscattered electrons are detected by a backscattered detector [120]. The information from the detector is used to generate an image to a screen for analysis. While scanning the electron beam on a sample, electrons build up on the surface and need a path to discharge these electrons. This can create imaging difficulties for insulating materials, since there is no easy way to dissipate the charge. Therefore, insulating materials are usually prepared with a thin conductive coating to facilitate discharge these electrons.

Similar to an SEM, a focused ion beam (FIB) provides capabilities such as patterning, as well as imaging. A FIB works in a similar manner as a SEM, but with an ion source, such as a gallium ion source (Ga^{+}), in place of an electron gun. A FIB typically operates at energies from 25 to 50 kV [120]. Imaging with a FIB may provide different contrasts when observing features, but care must be taken not to etch the sample when using a FIB for

imaging. A FIB also provides the capability to precisely pattern small dimensions with high accuracy, enabling cuts on the order of 20 nm [120]. FIB patterning is commonly used to cut into a materials surface to create a cross-sectional image of a sample. Some systems may have both an electron beam and a FIB, creating a dual beam system. A dual beam system adds further advantages such as the ability to deposit materials while running in situ imaging of the deposition [120]. A dual beam system provides the patterning and metal deposition capability needed to prepare samples for transmission electron microscope (TEM) analysis.

In this work, SEM characterization is used to prepare samples for TEM and to characterize TIJ resistors, as described in Section 3.3.2. The TEM sample preparation includes in situ deposition of protection layers (e-beam carbon and ion-beam Pt), patterning the lift out sample using a Ga^{+} ion source, mounting the sample to the appropriate TEM grid, and thinning the sample to $<$100 nm for TEM. SEM analysis of TIJ resistors provides high resolution images allowing for characterization of the device dimensions, confirming cavitation damage, and performing surface analysis after testing. This work was performed on a FEI Quantra 3D or a FEI Helios system at the Oregon State University electron microscopy facility with assistance from Dr. Pete Eschbach and Teresa Sawyer.

3.2.8 Transmission Electron Microscopy (TEM)

Transmission electron microscopy, or microscope, (TEM) is used for ultra-high resolution imaging of materials to enable atomic resolution imaging of a sample. A TEM transmits high energy electrons, 200 or 400 kV, through a thin sample to a detector to generate an image. Figure 3.11 is an illustration of the components in a TEM system. A TEM operates in an ultra-high vacuum environment to prevent electrons from scattering from anything other than the sample. At the top of the TEM column is an electron source to generate electrons which

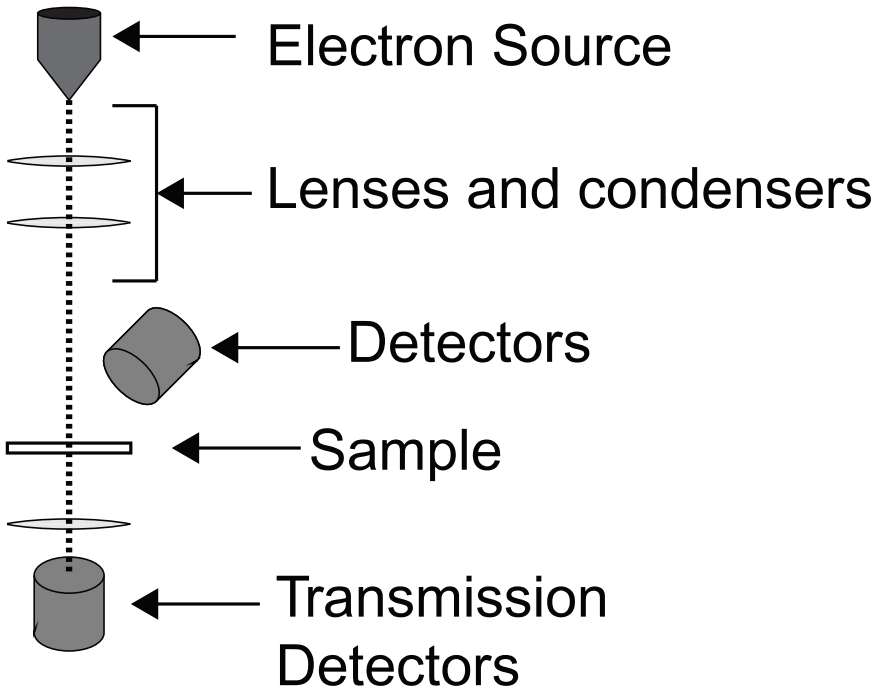

Figure 3.11: A TEM system showing the orientation of key components such as the electron source, lenses, sample, and detectors.

are accelerated through a high voltage column toward the sample. Next are the condensers, apertures, and lenses which are used to create a stationary electron beam that is focused into a radius of a few microns. These stages form the beam that hits the sample stage. The sample stage enables movement of the sample in and around the static beam in order to image different areas of the sample. Additional lenses, apertures, and detectors are position below the sample.

There are different types of transmission detectors on a TEM which enable different analytical techniques. Bright field images are formed by detecting electrons that have passed through the thin film, enabling ultra-high resolution images showing crystal structures and planes. In a bright-field image, low electron density atoms project bright areas and high elec-

tron density atoms create darker images. Transmitted electrons can also be detected using an annular detector that allows for dark field imaging. This provides diffraction analysis, such as selective-area diffraction (SAD) and convergent-beam diffraction (CBED), where different diffraction patterns are created from a material's atomic structure [121]. Finally, electrons passing through the sample may be analyzed by an electron energy-loss spectrometer (EELS). EELS experiments may be used for quantitative compositional analysis and structural information [122].

A modern TEM may also be equipped with a scanning electron capability, creating a scanning transmission electron microscope (STEM) system. In STEM, a ~ 0.2 nm diameter electron beam of a is rastered across the sample [121]. A backscattered detector is used to create ultra-high resolution imaging of the sample. Commonly, an energy dispersive x-ray detector is used in a STEM system, allowing for atomic mapping of a material at fine resolution. This enables elemental profiling through the depth of a thin film.

Figure 3.12 depicts typical images obtained for this dissertation. Figure 3.12 (a) is an ultra-high resolution image of an interface between a thermally grown SiO_2 on a single crystal silicon substrate. The left side of Fig. 3.12 (a) shows the lack of atomic order in the SiO_2 in comparison to the right side where the lattice of the single crystal makes a clear pattern. Figure 3.12 (b) is a convergent beam diffraction pattern (CBED) of the amorphous SiO_2 region shown in Fig 3.12 (a). The broad diffuse hallow pattern is typical of an amorphous structure. Figure 3.12 (c) is a CBED pattern from the single crystal silicon shown in Fig. 3.12 (a). The bright spots in the CBED pattern is due to the constructive interference from the equal atomic spacing in a single crystal lattice.

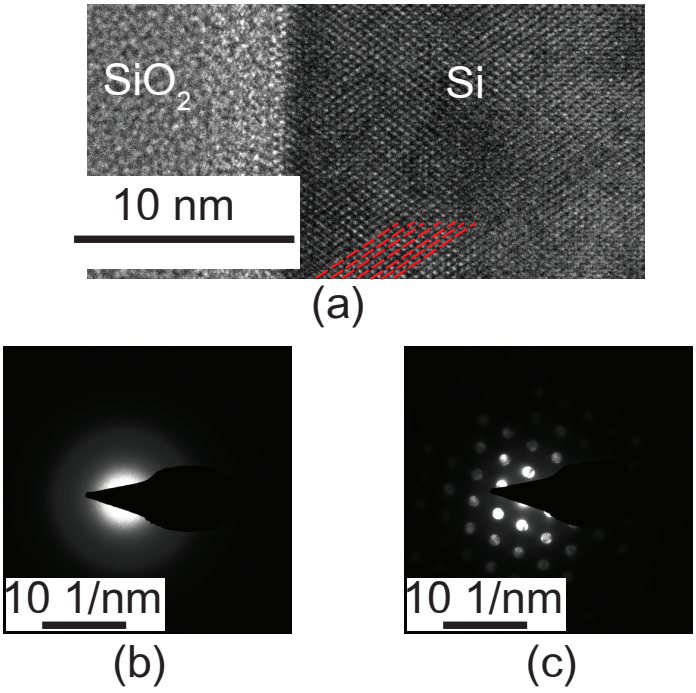

Figure 3.12: (a) A TEM image at the interface of thermally grown amorphous SiO_2 (left) on a single crystalline Si substrate at 730 kx magnification. The Si lattice and crystalline grains are highlighted by the dashed red lines in the Si. (b) Convergent beam electron diffraction (CBED) pattern of amorphous SiO_2 with the halo pattern indicative of an amorphous structure. (c) A CBED pattern from a single crystal silicon substrate with bright spots from constructive interference indicative of a single crystal lattice.

In this work, a FEI Titan 80-200/ChemiSTEM TEM at the Oregon State University Electron Microscopy Facility was used. TEM analysis was used for high resolution imaging and CBED studies to analyze the structure of as-deposited and annealed AMTFs. This provides additional evidence for the amorphous structure and allows further for analysis in crystallization studies. Additionally, oxidation studies utilized high resolution imaging and STEM elemental analysis to elucidate the oxidation behavior of the AMTFs. Finally, TEM is used to analyze the interface between the metals and insulator in metal-insulator-metal devices.

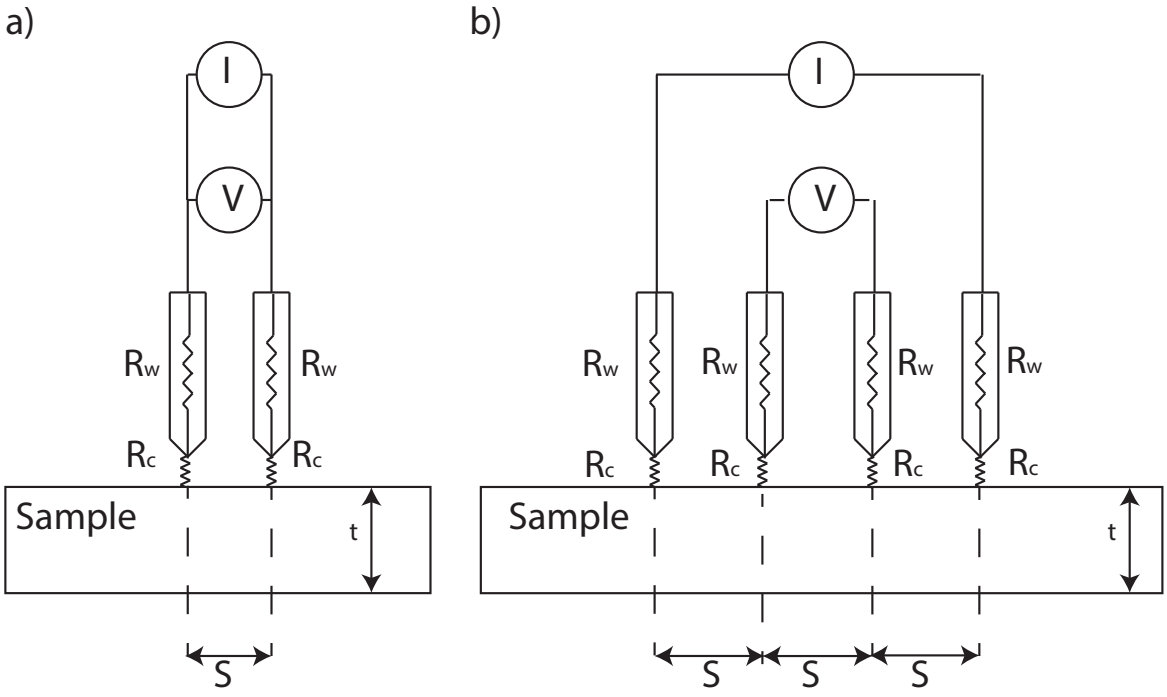

Figure 3.13: (a) A two-point resistance measurement and (b) a four-point probe system where I is a current source, V is a voltage probe, R_w represents the wire's resistive component, R_c represents the contact resistance.

3.2.9 Four-Point Probe

A four-point probe measurement is a rapid technique which provides valuable material information, such as resistivity and sheet resistance of a thin film. Resistivity describes the electrical conduction property of a material. Typically, resistivity of an amorphous metal is can be two to ten times higher compared to its crystalline components [4]. Sheet resistance is a thin film measurement describing the overall film resistance in units of Ohm per square ($\frac{\Omega}{\square}$). The sheet resistance also provides valuable information regarding film thickness and can serve as a diagnostic tool to monitor deposition variation.

A four-point probe measurement offers a more accurate resistance assessment compared to two-point measurements since it eliminates errors associated with external resis-

tances. Basic aspects of two-point and co-linear four-point probe measurements are shown in Fig. 3.13. In the two-point measurement approach shown in Fig. 3.13 (a), the voltage drop across a wire (R_w) and a contact (R_c) are in-series with the current source (I) and constitute a significant contribution to the measured voltage (V). This makes it difficult to make an accurate resistance measurement of the sample. On the other hand, a co-linear four-point probe measurement as shown in Fig. 3.13 (b) uses two separate pairs of contacts to source current and measure the voltage. The addition of the two probes for a voltage measurement makes the contribution of R_w and R_c to the measured voltage insignificant in comparison to the thin film [105]. This leads to improved accuracy in the resistance measurement of the sample. Assuming the probes are equally spaced, resistivity can be calculated as,

$$\rho = 2 \times \pi \times s \times \frac{V}{I} \tag{3.3}$$

where V is the measured voltage, I is the current sourced through the sample and s is the probe spacing. For a thin film measurement, the sample thickness is much less than the probe spacing and a correction factor to Equation 3.3 is required [105]. The thin film resistivity is shown in Equation 3.4,

$$\rho = \frac{\pi}{ln(2)} \times t \times \frac{V}{I} \tag{3.4}$$

where V is volts, I is the current, t is the sample thickness and $\frac{\pi}{ln2}$ is the correction factor. Using the four-point probe et is possible to calculate sheet resistance [$\frac{\Omega}{\square}$] as

$$R_{SH} = \frac{\pi}{ln(2)} \times \frac{V}{I} \tag{3.5}$$

Sheet resistance measurements provides the means to determine the film thickness from a sample with a known resistivity. Using Eqn. 3.4 and Eqn. 3.5 allows the thickness to be

solved as

$$t = \frac{\rho}{R_{SH}}. \tag{3.6}$$

The four-point probe measurements were performed on a Jandel RM2 system in the Oregon State University Cleanroom MaSC facility. The Jandel model is a co-linear setup as shown in Fig. 3.13 (b). Thickness measurements from a profilometer are used to determine resistivity from Eqn. 3.4. If thickness measurements can not be obtained, sheet resistance values are used to correlate film properties with deposition parameters.

3.2.10 Additional Techniques

While structural and electrical analysis of AMTFs is the main focus of this study, additional techniques are used to characterize thickness, oxidation growth and film composition. This information is used as supporting information of this work. A brief description of these techniques are as follows:

- Profilometery - Profilometry is used to determine film thickness and characterize the deposition rate. Kapton tape is placed on the substrate prior to deposition and removed post deposition, providing a thickness step in the film. The profilometer is a stylus tip that is dragged across the surface. As the tip moves up over the step, vertical deflection of the stylus tip allows for assessment of the film thickness [123]. All profilometry measurements are performed using an Alpha Step 500 surface profiler in the Oregon State University MaSC Cleanroom facility.

- Electron probe micro-analysis (EPMA) - EPMA provides elemental composition of a thin film. An electron beam bombards the film's surface, exciting core electrons. As another electron fills empty core states, x-rays are emitted providing a unique elemental

spectrum [105]. These x-rays are detected using a wavelength dispersive spectrometer (WDS) and compared to that of a reference sample for each element. From the unknown sample and the reference spectrums, a thin film composition can be determined . Since the electron beam penetrates several microns into the sample, EPMA analysis is best accomplished for thin film thickness approaching or exceeding 1 μm [105]. The measured component of the substrate can be properly accounted for by appropriate modeling or by using a substrate of a different elemental composition. All EPMA measurements are performed at the University of Oregon CAMCOR facility.

3.3 Thermal Inkjet Resistor Fabrication and Test System

This section describes the fabrication techniques used to make a TIJ resistor and the test bed developed for proof-of-concept application testing. A TIJ resistor is formed by patterning the resistor material between two low impedance traces. These resistors are subsequently tested by driving a short voltage pulse to provide sufficient energy to nucleate a bubble over the resistor material, as discussed in Sect. 2.1. The resistor material is evaluated before and after electrical testing to determine the material's stability.

3.3.1 Photolithography

Photolithography is a standard processing technique used in the microelectronic industry. In photolithography, a mask is used to transfer a pattern into a photosensitive material called photoresist. This allows for selective removal of materials, such as metals or oxides, in order to define traces, transistors, or other desired features. For this work, TIJ resistors and traces are fabricated via a two-step photolithography process utilizing both an etch and a

lift-off technique. A brief description of photolithography processing is presented, followed by integration details for building a TIJ resistor.

A photomask and high-energy light source are used to transfer a pattern into the photoresist. The photomask is a made of glass (or a transparent material) that contains opaque areas of a desired pattern. Typically the opaque areas are formed by a patterned chrome thin film. To transfer the pattern, the photomask is placed over the photoresist and exposed to a high energy light source, such as a 350 W mercury arc lamp [111]. Light passes through the transparent areas and is blocked by the opaque areas. Under the transparent areas, solvent is driven out of the photoresist due to the energy of the light. Driving out the solvents allows the phototresist to be chemically removed in the areas that are exposed to light

Figure 3.14 (a) to (d) is a graphical depiction of phtotolithography process steps. First, a liquid photoresist is applied and spread across the substrate by spinning it at high speeds, as shown in Fig. 3.14 (a). This process forms a uniform layer of photoresist across the substrate, as shown in Fig. 3.14 (b). The photoresist is subsequently soft-baked at an elevated temperature, as shown in Fig. 3.14 (b). The soft-bake drives out solvents and hardens the photoresist into a solid film. The substrate is aligned to the appropriate bottom layer, placed into direct contact with the photomask, and exposed to a light source. After exposure to the light source, the substrate is placed in a liquid developer solution. The developer removes areas of photoresist that were exposed to light and leaves unexposed areas on the substrate. This results with the remaining photoresist in the same pattern as the photomask, as seen in Fig. 3.14 (d). This creates a patterned substrate ready for the future etching.

Figure 3.14 (e) and (f) shows the etching process once the photoresist has been patterned. After patterning, the photoresist undergoes a hard-bake to allow it to be exposed to

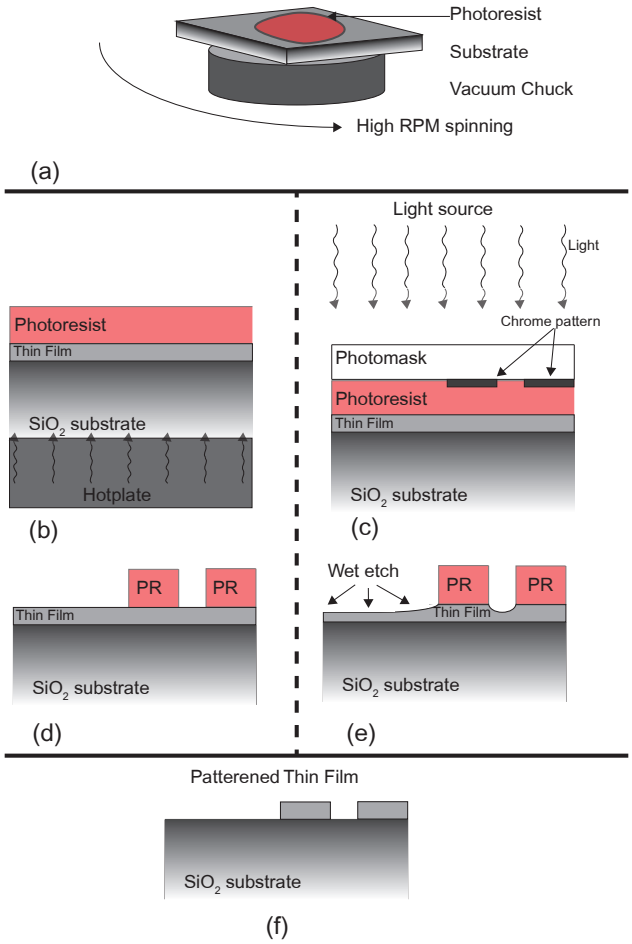

Figure 3.14: A photolithography and etch process to pattern a thin film. (a) Application and spinning of the photoresist to create a uniform layer on the substrate. (b) The soft-bake process to solidify the photoresist. (c) Alignment and exposure of the photoresist using a contact mask. (d) A substrate with patterned photoresist ready for an etch process. (e) The etch process removing exposed areas of the thin film. (f) A patterned thin film on a substrate after an etch process.

etchants. Once the substrate is patterned, a bath of the desired wet etchant solution is prepared. The wet etchant is selected to chemically remove the thin film to be patterned. The substrate is then submerged in the etchant bath and the etchant removes the exposed areas of the thin-film, as shown in Fig. 3.14 (e). Once all of the film is removed, the substrate is

removed from the bath, and photoresist is removed. This leaves the remaining material in the same pattern as the mask, as seen in Fig. 3.14 (f).

Material compatibility is a key factor in wet etch processing and process integration. Ideally, the lower or adjacent layers will not etch in the bath allowing for an etch stop [111]. This may not always be the case, and the wet etch solution may also attack other films in the device creating selectivity issues. If the etchant attacks other films in the stack, careful process development and timing is needed to prevent over-etching and etching of materials that are meant to remain.

Figure 3.15 shows the processing steps for a lift-off process. Similar to the etch process Fig. 3.15 (a) through (d) depict application and patterning of the photoresist. After the photoresist is patterened on the substrate, the desired thin film material is deposited onto the substrate, as seen in Fig. 3.15 (e). The photoresist is then removed by an appropriate solvent, as shown in Fig. 3.15 (f). Areas of the thin film that were deposited onto the photoresist are removed and only areas of the thin film deposited on the substrate remain. The thin film is patterned as the inverse image of the pattern on the photomask, as seen in Fig. 3.15 (g).

Lift-off processing is used for rapid material development and has key trade-offs versus the etch process. The two advantages are: 1) lift-off does not require a specific etch solution to be developed for a new thin-film material, and 2) etch selectivity is not relevant. The disadvantage of a lift off process is flagging, as seen in Fig. 3.15 (c). Flagging is due to material being deposited onto the sidewall of the photoresist, making a continuous film from the substrate to the top of the photoresist. When the photoresist is removed, the thin film on the sidewall may break, leaving an additional vertical feature.

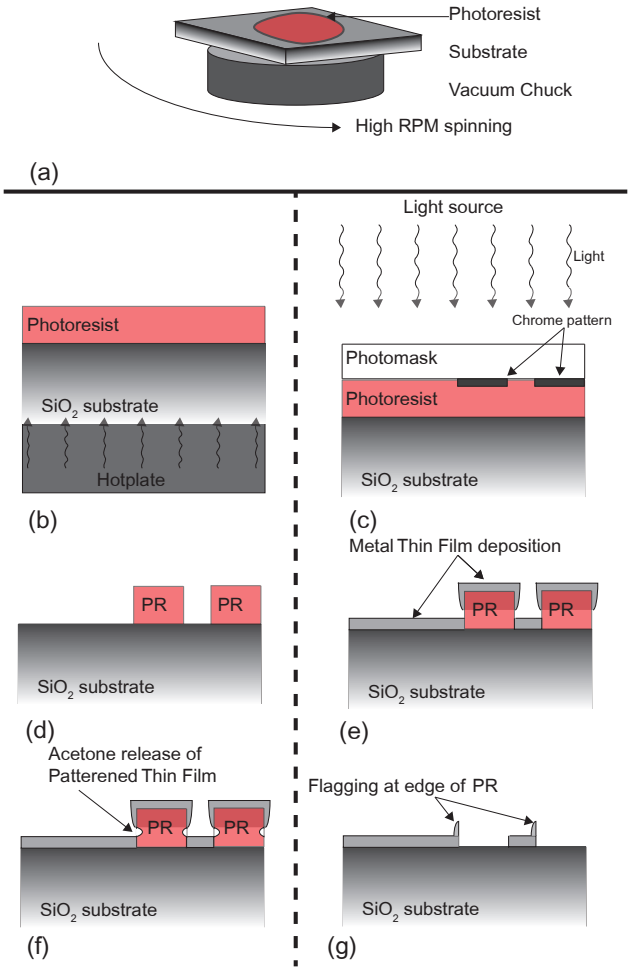

Figure 3.15: A photolithography and lift-off process to pattern a thin film. (a) Application and spinning of the photoresist to create a uniform layer on the substrate. (b) The soft-bake process to solidify the photoresist. (c) Alignment and exposure of the photoresist using a contact mask. (d) A substrate with patterned photoresist ready for a lift-off process. (e) Deposition of a thin film for the lift-off process. (f) Acetone dissolving the photoresist to remove the thin film from the patterned areas. (f) A patterned thin film on a substrate after a lift-off process depicting flagging.

The fabrication process used in this dissertation is shown in Fig. 3.16. First, S1818 photoresist is spun and patterned onto a Si substrate with 800 nm thermal SiO_2 for a lift-off process, as seen in Fig. 3.16 (a). Next, the AMTF resistor material and trace material are both sputtered onto the substrate without breaking vacuum, as seen in Fig. 3.16 (b). This prevents contact resistance problems due to the formation of a surface oxide between the two films.

Next, the photoresist is removed by dissolving the S1818 in acetone for 1 hour followed by a 5 minute sonication process, Fig. 3.16 (c). Photoresist is then spun on the substrate and aligned to the bottom layer to remove the trace material over the resistor, defining the resistor area, as shown in Fig. 3.16 (d). The trace material is etched in Transene Type A aluminum etchant at 50 °C. The AMTF acts as an etch stop and, thus, there is no selectivity issues. Finally, the photoresist is removed and the TIJ resistor and traces are formed as seen in Fig. 3.16 (e).

Eight resistors are patterned on each substrate. The AMTF resistor material is deposited to a thicknesses of $\sim$100 nm. The Al or AlCu is deposited to a thickness of $\sim$130 nm as the trace material. The AMTF material is patterned into a 30 by 30 μm device creating a $\sim$23 Ω resistor with an additional $\sim$1 to 3 Ω resistance due to the trace impedance. A substrate holder was fabricated to hold the substrate with pogo pins to interface the on chip devices to the TIJ firing circuit and test equipment as described next.

3.3.2 Thermal Inkjet Resistor Characterization and Test Procedure

To generate nucleation and deliver ink from a TIJ device, a short electrical pulse is used for joule heating of the the resistor, as described in Section 2.1. An arbitrary waveform generator (AWG) is used as an input to generate the voltage pulses to control each firing event. The AWG provides the ability to program a fixed pulse width to be delivered to the resistor a set number of times.

The AWG is unable to provide sufficient power for the firing events. Therefore an amplifying circuit is needed to supply the appropriate voltage. Figure 3.17 is a diagram of the firing circuit used to deliver the appropriate voltage to the TIJ resistor. A two transistor firing circuit is used to remove the applied voltage from the TIJ resistor between firing events, elim-

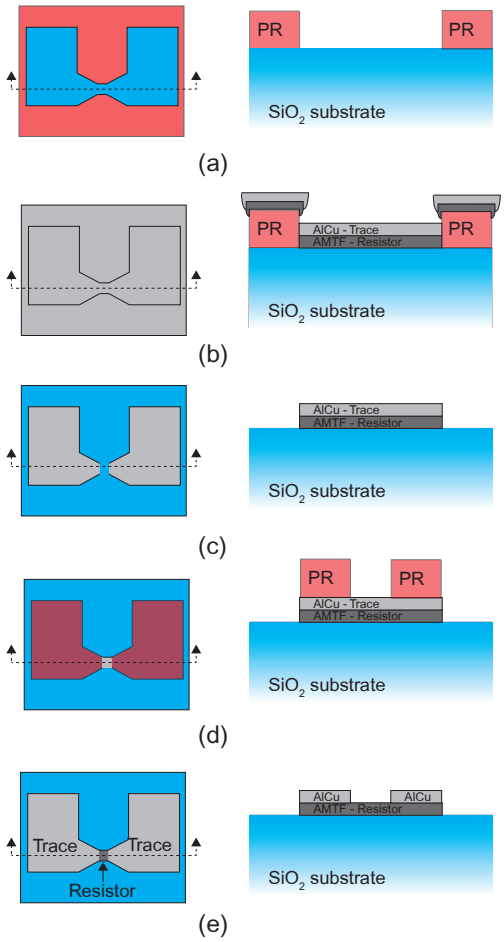

Figure 3.16: A top-down and cross-section illustration of the fabrication of a TIJ resistor. (a) Patterning the photoresist on a SiO_2 substrate for a lift-off step. (b) The substrate after the AMTF resistor material and trace material deposited prior to lift off. (c) The substrate after the lift-off process forming the trace and resistor patterns. (d) Patterned photoresist on the substrate to etch the trace material and form the TIJ resistor. (e) The final design of a TIJ resistor patterned between the traces.

inating any electrochemical effects between firing events. Two n-type field effect transistors (nFETs), Q1 and Q2, are used to provide the firing voltage to the TIJ resistor. The drain of Q2 is connected to a power supply set to the firing voltage, V_{Fire}. When Q2 is driven to the on state, V_{Fire} plus V_{ONQ2}, Q2 turns on, creating a firing event. The gate of Q2 is controlled by the drain of Q1. When Q1 is on, Q1's drain voltage is approximately at ground, and Q2 is off. A current-limiting resistor, R1, is installed to prevent a direct short between the power

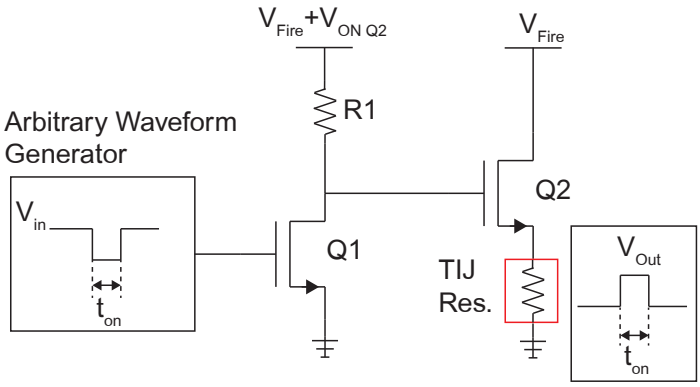

Figure 3.17: The test bed created to provide voltage pulses to a TIJ resistor in order to simulate the TIJ environment.

supply and ground. When Q1 is off, Q1's drain voltage is equal to the power supply, set to V_{Fire} plus V_{ONQ2}, and Q2 is turned to an on state. Thus, (Q1 off, Q2 on) creates a firing event. The gate of Q1 is connected to the AWG output. The AWG is used as an active low input to pulse the firing voltage.

The test bed electronics consist of an AWG, two power nFETs, a resistor, and an oscilloscope. A Tektronix 420 AWG was used as the input AWG. On Semiconductor NTD4963N-35G power FETs are used as the nFETS with a 100 Ω resistor as R1. The AWG pulses to input to deliver firing events with a pulse width of 3 to 10 μs at a 2 kHz frequency. The output of Q2 is connected to the substrate via pogo pins and 18MΩ deionized water is placed over the resistor. The firing voltages were monitored with a Tektronix DPO5000 oscilloscope to confirm the pulse width and shape.

In order to verify that a nucleation event has occurred, a high speed camera is used to capture the bubble formation. The high speed camera triggers the firing pulse and obtains an image of the resistor after a set time delay. Nucleation images are acquired sequentially through repeated firing of the resistor and incremental delays in image acquisition. The firing

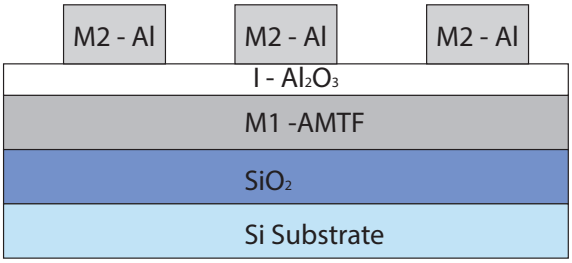

Figure 3.18: Cross-section of MIM devices fabricated with an Al_2O_3 insulator and shadow-mask Al top contacts deposited on to a silicon/silicon dioxide (SiO_2) substrate.

voltage is swept from 0.5 V to 10 V in 0.5 volt increments until nucleation is confirmed with the camera. The minimum voltage where nucleation occurs provides a measure of the minimum turn on voltage. A Princeton Instruments PI-MAX4 I-CCD high speed camera and an Olympus BX51WI microscope with a 60$\times$ water immersion objective are used to confirm nucleation of a vapor bubble.

Once a minimal voltage is found, two experiments are used to evaluate the stability of a resistor. The first experiment is resistor lifetime testing. In the lifetime testing, each resistor is pulsed until a catastrophic failure occurs. Failure of the resistor is determined as a resistance change of $>$ 40% increase in resistance in comparison to that the original resistance. The resistance is evaluated every 10,000 pulses in order to determine when the failure occurs. The second experiment investigates the material stability. Material stability testing is used to demonstrate the AMTF remains amorphous after pulsing half of the expected resistor lifetime. Optical microscopy, SEM is used to evaluate the surface of a tested AMTF resistor. TEM and electron diffraction are used to confirm the film remains amorphous.

3.4 MIM Device Fabrication and Electrical Characterization

This section summarizes the techniques used, in their respective processing order, to build a MIM device. Figure 3.18 shows a generalized structure for the MIM devices fabricated in this research. First, the AMTF bottom electrode (M1) is deposited via sputter deposition, as described in Section 3.1, onto a silicon thermal oxide substrate. Next the insulator, I, is deposited and prepared via atomic layer deposition (ALD) of Al_2O_3. Finally, the top electrode, M2 (aluminum), is deposited using thermal evaporation and a shadow mask.

It is the goal of this work to determine the stability of the metal-insulator interface after thermal processing. After the insulator deposition, the devices are annealed at various temperatures prior to the top contact deposition. This thermally stresses the device to simulate a thermal process. After fabrication and annealing, the interface stability is characterized through current-voltage measurements. Current-voltage characterization from an annealed device is compared to that of an as-deposited device to determine the device stability.

3.4.1 Atomic Layer Deposition

Atomic layer deposition (ALD) is used to provide a high-quality insulator for a MIM device. ALD forms pristine insulators, ideal for tunneling to occur. ALD is advantageous since it allows for a smooth, conformal, defect-free dielectric insulating layer [124]. An ideal ALD process involves saturated monolayer coverage. In practice, most ALD processes involve deposition of less than a single monolayer of material per cycle [125, 126].

Atomic layer control is accomplished though successive, self-limiting surface reactions [124]. Figure 3.19 illustrates the concept of the successive reactions. First, reactant A is introduced into a chamber until all of the surface sites are occupied, as seen in Figure 3.19 (a). Reactant 'A' is then flushed from the system, leaving only surface-absorbed material be-

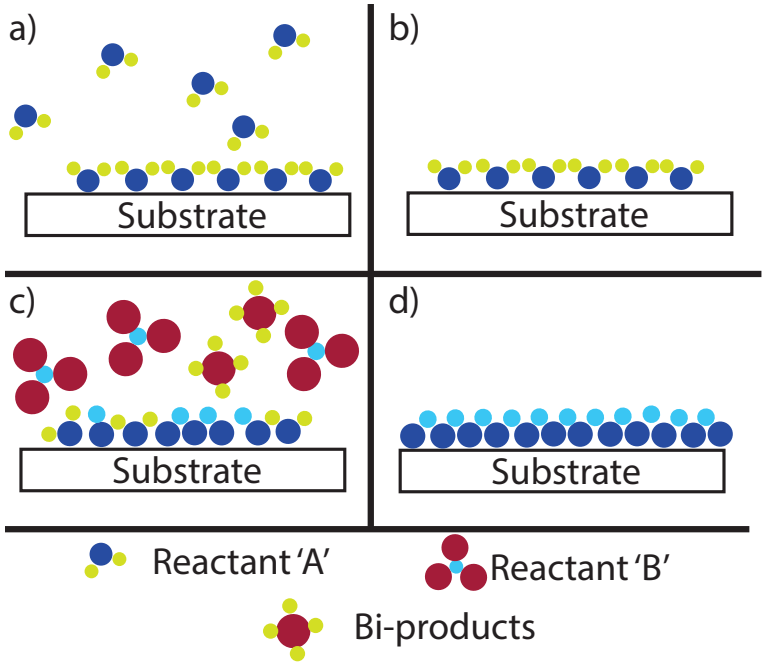

Figure 3.19: Self-limiting ALD reaction. a) Introducing reactant 'A'. b) Removing reactant 'A'. c) Introducing reactant 'B'. d) Removing reactant 'B' and byproducts.

hind, as indicated in Figure 3.19 (b). Next, reactant 'B' is introduced and reacts with reactant 'A' on the surface, leaving the desired film and creating byproducts, as given in Figure 3.19 (c). Finally, reactant 'B' and byproducts are purged from the system, as shown in Figure 3.19 (d). These steps are repeated successively until the desired thickness is achieved. The reaction and film growth per cycle are limited by the number of surface sites that are able to absorb the first precursor. This leads to a self-limited reaction and accurate thickness control for an ALD process.

Figure 3.20 shows the basic components of an ALD system, consisting of a loadlock, reactants, pulsing valves, and a vacuum reaction chamber. The system utilizes a loadlock to limit the introduction of contaminants into the main chamber. A dedicated reaction chamber is required for the deposition to take place. Each reactant has an individual pulse valve

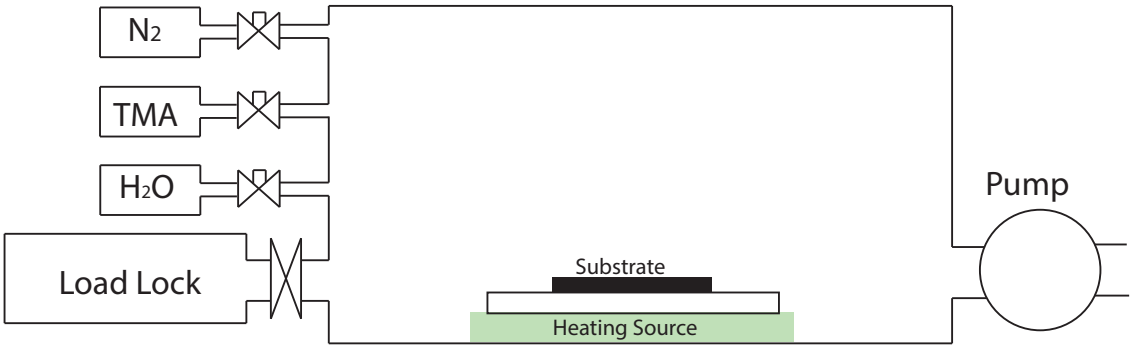

Figure 3.20: Components of an ALD system.

controlling flow of the reactant into the chamber. It is crucial that each reactant saturates the surface and is completely purged from the chamber. Thus, after each source is pulsed, vacuum pumping in conjunction with a nitrogen purge are used to flush out any excess material that is not absorbed at the surface. This ensures that the film grows on the surface (heterogeneously) and does not react in the gas phase (homogeneously). Continuous vacuum pumping with periodic nitrogen purges also flushes contaminants from the chamber. Finally, substrate heating is employed to enhance heterogeneous reaction rates and facilitate desorption of excess species.

ALD-deposited aluminum oxide is used as the insulator in the work reported here in. ALD is commonly employed for Al_2O_3 thin film deposition [124, 126]. Al_2O_3 deposition is accomplished with trimethylaluminum (TMA) as the metal reactant precursor and H_2O as the oxidizing reactant to form the dielectric, as given by $2Al(CH_3)_3 + 3H_2O \rightarrow Al_2O_3 + 3CH_4$, $AlOH^* + Al(CH_3)_3 \rightarrow AlOAL(CH_3)_2{}^* + CH_4$, and $AlCH_3{}^* + H_2O \rightarrow AlOH^* + CH_4$ where * indicates a surface species in the deposition process. This reaction has one of the highest reaction enthalpies of any ALD process, allowing high-quality films to be grown [124]. The Al_2O_3 thin films used in this research are deposited using the Beneq YP400 operated by

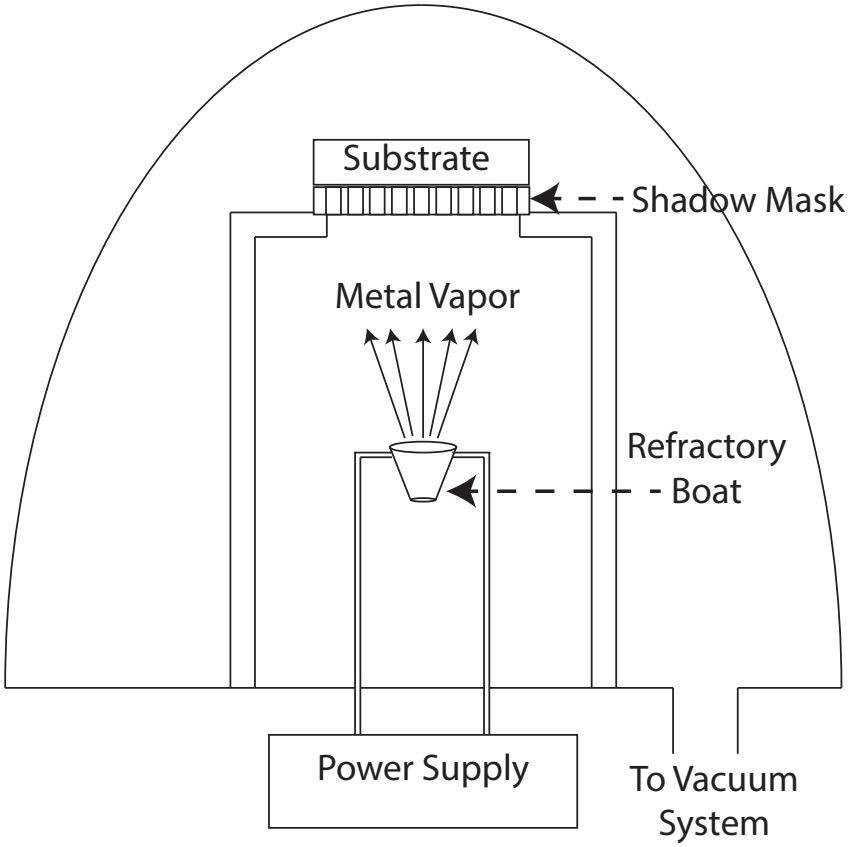

Figure 3.21: Components of a thermal evaporation system.

Amorphyx. Al_2O_3 films are deposited at temperatures between 285 - 300 °C on top of a AMTF bottom contact.

3.4.2 Thermal Evaporation and Shadow Mask

Thermal evaporation is a PVD vacuum process that utilizes thermal energy to bring a source material above its vapor pressure so that it sublimes or evaporates. The vapor pressure is the point at a given pressure, temperature and volume where a material transforms into the vapor phase [123]. Depending on the material, evaporation occurs from a liquid or solid state. Evaporation occurs from a liquid state when a material reaches its melting point prior to its vapor pressure. This occurs in most metals, including aluminum [113]. A material sublimes

from the solid source when the melting temperature is greater than the vapor pressure. Once in vapor form, the material travels from the source in a line-of-sight manner to the substrate. In this study, thermal evaporation is used to deposit top contacts for a MIM device.

Figure 3.21 shows the basic design and components of a thermal evaporation system. It consists of a refractory metal boat, a power supply, a substrate holder, and a vacuum system. A refractory metal boat is used as the resistive heating element and holds the source material. A refractory metal is used because of its robust thermal property, and can supply heat to the source appropriately without melting or reaching its own vapor pressure. This prevents contamination from the boat into the resulting film. The power supply provides current to heat the boat, which transfers thermal energy to the source heating it above its vapor pressure. The refractory boat is typically a cone shape to hold the material. In a wire boat, the surface tension holds the liquid melt together for the deposition [113]. The substrate holder is located at an appropriate distance from the source to achieve a uniform film thickness. This distance is determined by the diameter of the substrate; a larger substrate diameter requires more distance between the source and substrate to achieve uniform thickness [113]. Prior to deposition, a vacuum system pumps the chamber to a low pressure, about 2 to 4 * 10^{-5} Torr, to prevent any residual gas contaminating the film. A vacuum also provides an adequate mean free path, allowing the source material to transport to the substrate.

For this work, thermally evaporated aluminum using a shadow mask process is used as the top contact. A shadow mask is located between the substrate and source, preventing deposition from occurring in specific areas on the substrate, leaving the desired pattern. Figure 3.22 shows an illustration of the shadow mask used in this research. The pattern consists of 62.5, 125, 250, and 500 μm radius dots across the substrate. The shadow mask process is

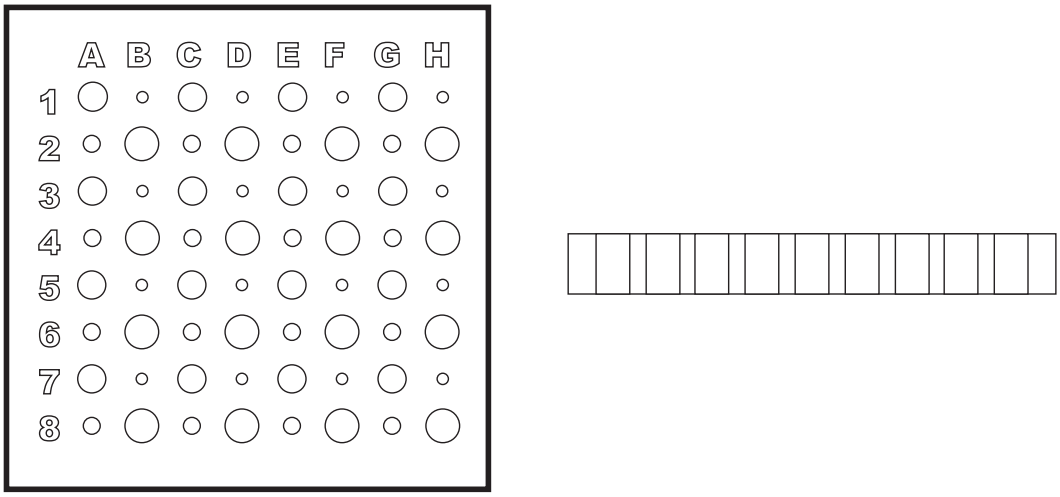

Figure 3.22: Shadow mask design.

not ideal due to shadowing effects. Shadowing arises from diffusion along mask edges from poor contact, creates larger devices with larger dimensions than desired, and creating sloped edges [123]. The aluminum contact is deposited using the Veeco Thermal Evaporation and Poloran Evaporator systems in the Oregon State University MaSC cleanroom facility. The deposition occurs at a pressure of $3 * 10^{-5}$ Torr and utilizes a tungsten wire boat.

3.4.3 I-V Electrical Characterization

MIM device performance is established by electrical assessment. Figure 3.23 is a log(I)-V curve for a ZrCuAlNi-Al_2O_3-Al MIM device. Starting at 0 V, a positive bias is applied and displacement and charging currents create a leakage current through the device, in the 10-100 pA range. As the applied voltage approaches 3 V, denoted in Fig. 3.23 as (a), there is a sharp increase in the current. This 'knee' occurs as the device turns on, establishing the turn-on voltage (V_{ON}). In this dissertation, V_{ON} is usually estimated as the applied voltage

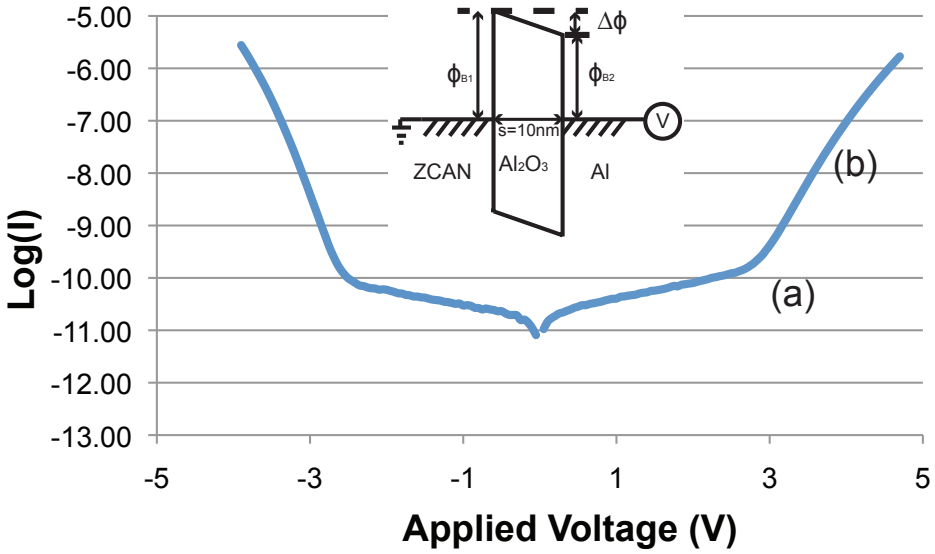

Figure 3.23: A plot of the logarithm of the current (*log(I)*) versus applied voltage (V) of the MIM device as indicated by the equilibrium energy band digram given in the insert. The knee in the current at ∼3 V labeled as (a) establishes the onset turn-on voltage for the positive sweep. The region labeled as (b) corresponds to the conduction mechnism, Fowler-Nordheim tunneling in this case, for the positive sweep.

at which the measured current is approximately an order of magnitude above the leakage current, e.g., 0.5 nA in Fig. 3.23. Beyond V_{ON}, a change current conduction mechanism begins to dominate the current-voltage response, resulting in a sharp increase in current, as shown in Fig. 3.23 (b). An applied negative voltage mirrors similar features across the y-axis, as seen Fig. 3.23.

The current conduction mechanism is a critical feature in a MIM device. The conduction mechanism is assessed through the various linearization techniques described in Section **??**. ALD Al_2O_3 is a high-quality insulator with a large barrier height. Thus, the ideal conduction mechanism through Al_2O_3 is Fowler-Nordhiem tunneling. A stable device can undergo the thermal process and exhibit no change in V_{ON} or the conduction mechanism.

DC I-V measurements are obtained using an Agilent 4155C Semiconductor Parameter Analyzer. Test parameters employed are a 'hold-time' of 200 ms, a 'delay time' of 100 ms, and a 'Medium' integration time. The sweep setting is set to 'double' to source voltages from 0 V to the maximum and return back to 0 V. In a MIM device measurement, the amorphous metal is the grounded contact and voltage is applied to the top Al contact. Contact to the bottom layer is made via scribing through the insulator, typically Al_2O_3, and soldering an indium contact to the bottom metal. Tungsten probes are used to contact devices.

4. MATERIALS CHARACTERIZATION OF HIGH-TEMPERATURE AMORPHOUS METALS

This chapter presents material characterization of amorphous metal thin films developed for TIJ and metal-insulator-metal devices. First, as-deposited thin films properties, including the structure of the thin film, are analyzed in order to confirm that the film is indeed amorphous. Next, deposition condition effects on thin film properties are discussed. Then, a thermal study to estimate the crystallization temperature is presented. Finally, oxidation study results are presented and compared to β-Ta.

4.1 Characterization of As-Deposited Thin Films

The compositions chosen for this study are $Ta_{40}Ni_{40}Si_{20}$, $Ta_{40}Mo_{40}Si_{20}$, $Ta_{40}Hf_{40}Si_{20}$, $Ta_{40}W_{40}Si_{20}$, $Ta_{30}W_{50}Si_{20}$, and $Ta_{30}W_{30}Si_{40}$. Thin films are deposited using RF magnetron sputtering, as described in Chapter 3. Each composition utilized its own multicomponent target, ordered from a commercial vendor. The targets are made to the desired stoichiometric film ratio through pressed metal powder fabrication. Kamis and Materion supplied the targets and confirmed target composition via x-ray diffraction of the powders.

Deposition conditions and a summary of as-deposited properties for thin films deposited from each target are presented in Table 4.1. The deposition conditions in Table 4.1 are the optimal conditions found through an experimental design of experiments. A discussion of deposition conditions corresponding to thin film properties is discussed in Section 4.2. All thin films sputter at rates between 6 and 10 nm-min^{-1} at their respective deposition conditions. Deposition rates are confirmed on films deposited between 200 and 500 nm thickness using an Alpha-step 500 Surface Profilometer.

Table 4.1: Summary of deposition conditions, rates, and as-deposited properties of amorphous metal thin films.

Target	**Power** $[Watts]$	**Pressure** $[mTorr]$	**Deposition Rate** $[nm-min^{-1}]$	**Composition**[4] $[at\%]$	**RMS Roughness**[5] $[nm]$	**Resistivity** $[\mu\Omega-cm]$
$Ta_{40}Ni_{40}Si_{20}$	100	10	6.0	$Ta_{42.6}Ni_{43.5}Si_{13.9}$	0.20	224±10
$Ta_{40}Mo_{40}Si_{20}$	100	10	8.9	$Ta_{43.4}Mo_{42.3}Si_{14.3}$	0.30	177±6
$Ta_{40}Hf_{40}Si_{20}$	100	10	9.8	$Ta_{43.7}Hf_{40.9}Si_{15.4}$	0.27	221±13
$Ta_{40}W_{40}Si_{20}$	100	10	7.7	$Ta_{45.3}W_{43.7}Si_{11.0}$	0.25	199±10
$Ta_{30}W_{50}Si_{20}$	100	15	8.1	$Ta_{35.4}W_{53.3}Si_{11.3}$	0.50	201±6
$Ta_{30}W_{30}Si_{40}$	100	10	7.6	$Ta_{41.7}W_{38.4}Si_{19.9}$	0.25	218±5

4.1.1 Compositional Analysis

Thin film compositions, obtained via EPMA, are listed in Table 4.1 for all of the materials used for this dissertation. The Si concentration in all of the thin films is found to be deficient in comparison to that of the target. This is attributed to Si being preferentially deposited off-axis onto the sputter chamber walls. Other researchers have previously reported that magnetron sputtering using a multicomponent target can result in a thin film composition different from that of the target [112, 127]. For example, sputtered WTi [128] and WSi [129] thin films are observed to exhibit a reduced concentration of the lighter element, Ti and Si, respectively, compared to that of the target. This is consistent with the sputtering trends observed herein.

[4] *Film composition estimated via EPMA, neglecting oxygen (<5%).

[5] RMS roughness values obtained from 200 nm thick films

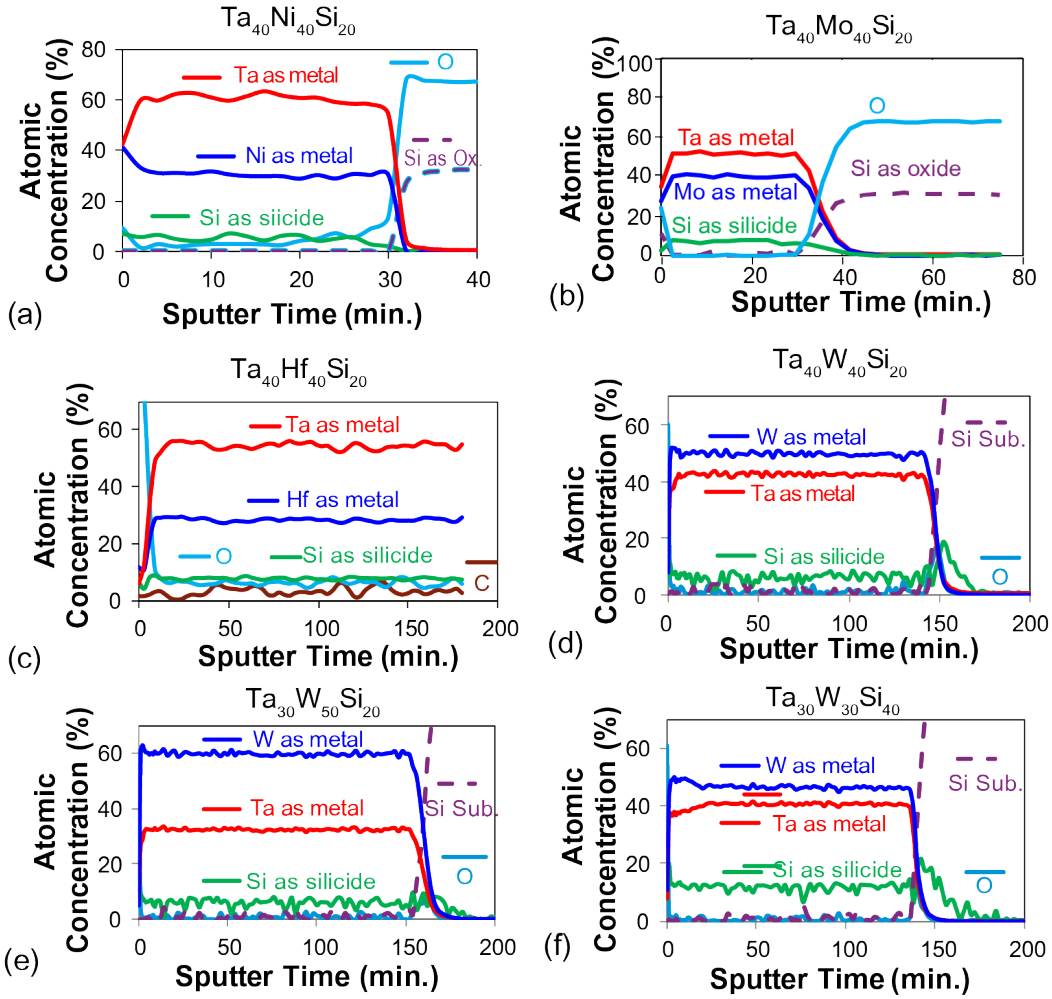

Figure 4.1: X-ray photoelectron spectroscopy (XPS) depth profile of (a) $Ta_{40}Ni_{40}Si_{20}$, (b) $Ta_{40}Mo_{40}Si_{20}$, (c) $Ta_{40}Hf_{40}Si_{20}$, (d) $Ta_{40}W_{40}Si_{20}$, (e) $Ta_{30}W_{50}Si_{20}$, and (f) $Ta_{30}W_{30}Si_{40}$ thin films showing uniform composition thorughout the bulk of the film. Each film is deposited at their optimized deposition conditions, as reported in Table 4.1. XPS analysis is performed by Dr. William Stickle of the HP Inc.

Figure 4.1 is an XPS composition and chemical-state depth profile of a 200-nm thick thin film from each of the targets. These profiles demonstrate that the elemental distribution of Ta, metal (Ni, Mo, Hf, or W), and Si is uniform throughout the bulk of the thin film. If any oxygen is present in the thin film, it is also distributed uniformly through the film, as seen in Fig 4.1 (c). Note that the atomic ratios in Fig. 4.1 cannot be compared directly to the

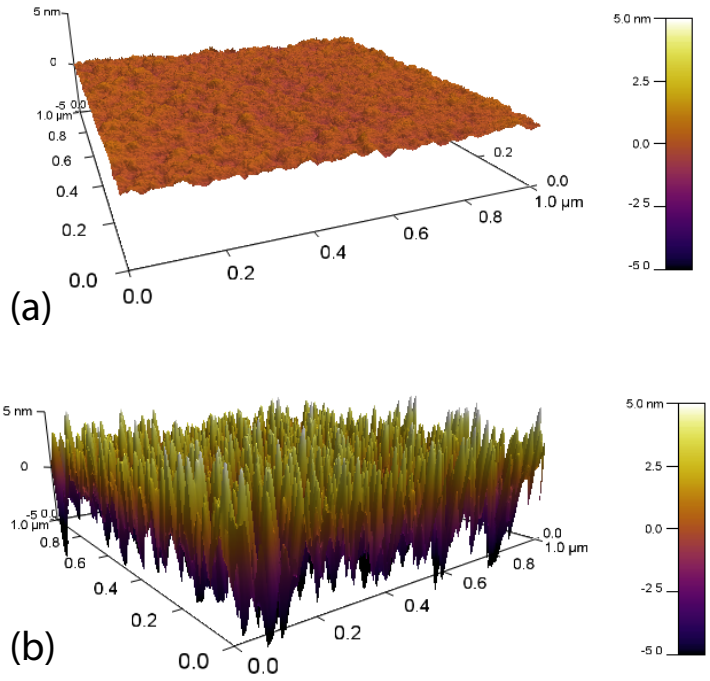

Figure 4.2: Atomic force microscopy (AFM) topography image of (a) an as-deposited $Ta_{40}W_{40}Si_{20}$ thin film 200 nm deposited at 100 W RF power and 10 mTorr, and (b) a Ta thin film provided by HP Inc.

composition established by EPMA, as the compositional depth profile has not been corrected for preferential sputtering.

4.1.2 Surface Morphology

An amorphous film has an atomically smooth surfaces due to the lack of grain boundaries. Figure 4.2 (a) is an AFM topology measurement of a 200 nm $Ta_{40}W_{40}Si_{20}$ thin film with a root-mean squared (RMS) surface roughness of 0.25 nm. Figure 4.2 (b) is an AFM topographic measurement from a crystalline tantalum thin film which has a RMS surface roughness of 2.1 nm. These images clearly demonstrate the atomically smooth nature of an amorphous thin film, in contrast to that of a crystalline film. The measured RMS surface

roughness of a 200 nm thin film deposited at its optimal condition for each material is listed in Table 4.1. The thin-film roughnesses are indicative of an amorphous film and each material possesses a RMS roughness under 0.5nm.

4.1.3 Electrical characterization

An amorphous metal typically exhibits a resistivity larger than its constituent elements [4]. Table 4.1 lists the measured bulk resistivity for as-deposited thin films for each material. The resistivity data supports the amorphous nature of the thin film. All films show resistivities approximately equal to 200 $\mu\Omega - cm$, which is larger than each of the constituent metal elements. The small variation between the materials is likely due to a small structural difference, creating a difference in mean free path, or due to the variation in electron concentration from each of the individual elements in the composition. Resistivity measurements are performed using a co-linear four-point probe and values are confirmed over a range of thin film thickness from 100 to 500 nm.

A temperature-dependent resistance measurement for $Ta_{40}W_{40}Si_{20}$, $Ta_{30}W_{30}Si_{40}$ and $Ta_{40}Ni_{40}Si_{20}$ thin films are shown in Fig. 4.3 (a) and (b). The thermal coefficient of resistivity (TCR) describes how the resistance of the film changes with increasing temperatures. As discussed in Section 2.3.1, an amorphous (crystalline) metal with a bulk resistivity above (below) 150 typically has a small negative (large positive) thermal coefficient of resistance. All of these thin film possess a negative slope, indicating a negative TCR. The TCRs for $Ta_{40}W_{40}Si_{20}$, $Ta_{30}W_{30}Si_{40}$, $Ta_{40}Ni_{40}Si_{20}$ thin films are -2.00×10^{-4}, -1.00×10^{-4}, and -1.49×10^{-4} K^{-1}, respectively. This range of TCR is small and negative, as expected for an amorphous metal thin film.

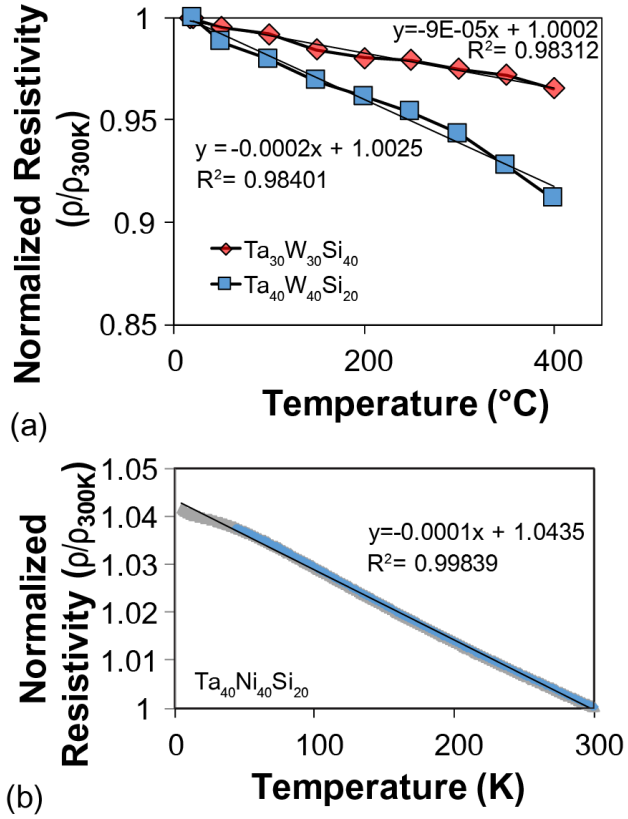

Figure 4.3: Normalized resistivity versus temperature measurements of (a) $Ta_{40}W_{40}Si_{20}$ and $Ta_{30}W_{30}Si_{40}$ thin films and (b) of a $Ta_{40}Ni_{40}Si_{20}$ thin film deposited at 100 W (RF) and 10 mTorr.

4.1.4 Structural Analysis

A diffraction pattern of an amorphous material should consist of one or more broad scattering features and a lack of sharp peaks from Bragg reflections. GI-XRD patterns for all thin films deposited at their optimal deposition conditions are shown in Fig. 4.4. All GI-XRD patterns are indicative of an amorphous thin film, possessing broad 2θ features from approximately 35 to 45° and 60 to 75°, which are attributed to diffuse scattering from a disordered atomic structure. The absence of any Bragg reflections or sharp, distinctive peaks indicates a lack of long-range crystalline order. Similarly, CBED analysis shows diffuse halos in the electron diffraction pattern, confirming the absence crystallization. CBED analysis of

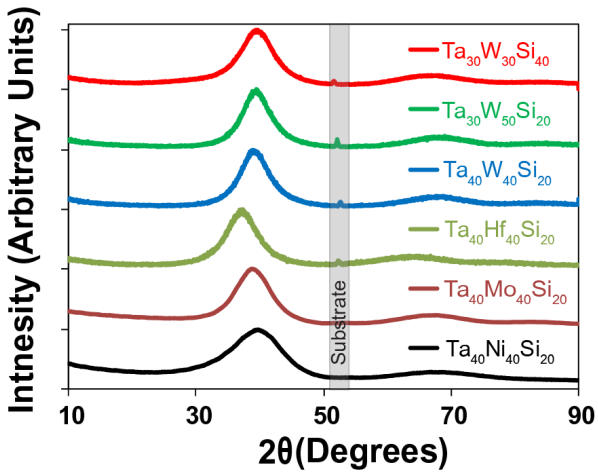

Figure 4.4: As-deposited x-ray diffraction (XRD) patterns for thin films deposited at optimal deposition conditions. A silicon substrate peak artifact is also identified.

$Ta_{40}Ni_{40}Si_{20}$, $Ta_{40}Hf_{40}Si_{20}$, $Ta_{40}W_{40}Si_{20}$, and $Ta_{30}W_{30}Si_{40}$ thin films are shown in Fig. 4.5. Similarly, the pattern for $Ta_{30}W_{50}Si_{20}$ shows diffuse halos, but also sharp spots. These spots represent nanocrystalline domains of WSi_2 [11] embedded in an environment of amorphous metal. From the high resolution TEM image and the lack of diffraction peaks in the GI-XRD pattern, we estimate the diameter of the nanocrystallites to be < 4 nm. Considering the small grain size and apparent low concentration of the crystallites, we consider the samples to be substantially amorphous.

4.2 Deposition Condition Effects on Thin Film Properties

As-deposited thin film properties are influenced by the deposition conditions. Changing power, pressure, substrate-to-target distance, target-to-substrate orientation, and other parameters effect the energy of the atoms arriving at the substrate, changing the film growth process. Modifying the thin film growth process leads to the ability to tune and modulate thin film properties, such as resistivity and RMS surface roughness.

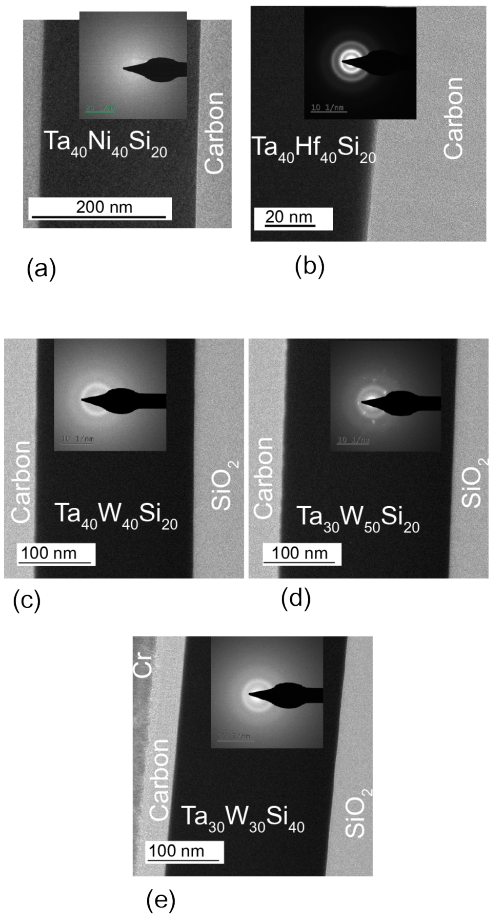

Figure 4.5: TEM cross section and convergent beam electron diffraction (CBED) pattern of (a) $Ta_{40}Ni_{40}Si_{20}$, (b) $Ta_{40}Hf_{40}Si_{20}$, (c) $Ta_{40}W_{40}Si_{20}$, (d) $Ta_{30}W_{50}Si_{20}$, and (e) $Ta_{30}W_{30}Si_{40}$ thin films. All diffraction analysis confirms the amorphous structure. $Ta_{30}W_{50}Si_{20}$ CBED pattern shows evidence nano-crystalline domains in the amorphous thin film. Imaging performed with assistance from Dr. Peter Eschbach at Oregon State University's Electron Microscopy Facility.

The influence of sputtering power and pressure on the thin film properties for the $Ta_{40}Mo_{40}Si_{20}$ system is summarized in Table 4.2. The trends found in this design of experiments is consistent with all of the multicomponent targets used in this dissertation. A design of experiments modifying power and pressure is used to determine the optimal sputtering conditions reported in the previous section, but the details are not presented here.

Table 4.2: Deposition rates and as-deposited properties of $Ta_{40}Mo_{40}Si_{20}$ thin films.

Power $[Watts]$	Pressure $[mTorr]$	Deposition Rate $[nm-min^{-1}]$	Composition $[at\%]$	RMS Roughness[6] $[nm]$	Resistivity $[\mu\Omega-cm]$
50	10	5.0	-	-	178
50	20	6.0	-	-	973
100	10	8.9	$Ta_{41.0}Mo_{39.8}Si_{13.5}O_{5.7}$	0.3	177
100	20	10.9	$Ta_{36.2}Mo_{35.5}Si_{13.7}O_{14.6}$	0.98	332

The deposition rate increases with increasing the power and pressure, as seen in Table 4.2. The increase in deposition rate with increasing power is expected and is consistent with sputtering theory. Increasing power increases the self-bias across the plasma sheath, accelerating ions to higher energies so that the sputter yield increases, thereby increasing the deposition rate. The small increase in deposition rate by changing the pressure from 10 mTorr to 20 mTorr is the second observation in this experiment. This is not expected according to conventional sputter theory. It is common for the deposition rate to decrease as the mean free path decreases, due to an increase in the process pressure. This is due to more collisions of the sputtered species, decreasing the impingement rate of sputtered species arriving at the substrate [112]. A possible explanation for the observed increase in deposition rate with increasing pressure could be the change in composition and increased oxygen concentration in the thin film composition, as discussed next.

Elemental composition, determined by EPMA, for thin films deposited at 10 mTorr and 20 mTorr are shown in Table 4.2. The elemental analysis includes oxygen incorporation.

[6]RMS roughness values obtained from 200 nm thick films

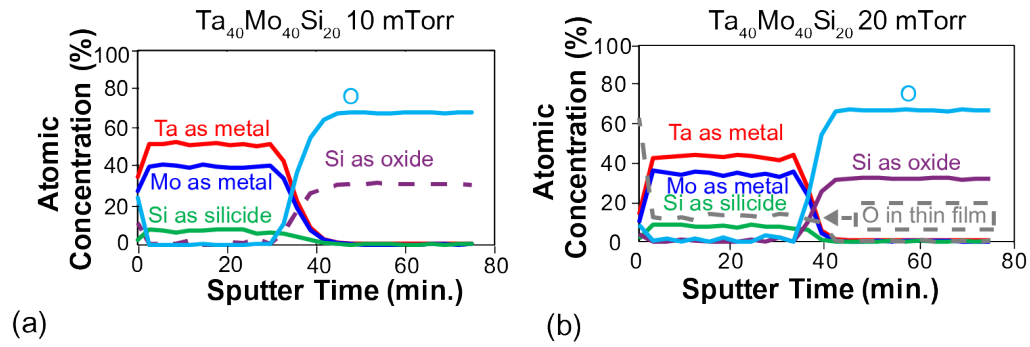

Figure 4.6: X-ray photoelectron spectroscopy (XPS) depth profile of (a) a $Ta_{40}Mo_{40}Si_{20}$ thin film deposited at 100 W RF and 10 mTorr, and (b) a $Ta_{40}Mo_{40}Si_{20}$ thin film deposited at 100 W RF and 20 mTorr. XPS analysis performed by Dr. William Stickle of the HP Inc.

Films deposited at a higher pressure have an increased incorporation of oxygen. There are many potential sources for oxygen incorporation into the thin film during the sputter processing. These include residual oxygen after reaching base pressure, oxygen introduced by the process gas lines, or oxygen from a system leak. As the system pressure is increased to reach 20 mTorr, the total partial pressure of oxygen also increased in the system. This increased the number of oxygen atoms that impinged on the substrate surface during the deposition, leading to an increase in the oxygen concentration. Also, at a higher pressure the residence time of the sputtered species increases. This causes the sputtered species to have multiple interactions in the chamber, increasing the probability of oxygen reacting in the system. An increase in either resident time or partial pressure can result in an increase in oxygen incorporation.

The XPS analysis of $Ta_{40}Mo_{40}Si_{20}$ films deposited at 100 W (RF) and 10 mTorr and 20 mTorr are shown in Fig. 4.6 (a) and (b), respectively. After penetrating through the surface, the elemental ratios remain constant throughout the bulk of a film. The depth profile supports the EPMA findings that lower pressure depositions have small amounts of oxygen ($\sim$5%)

and the higher pressure depositions have significantly more oxygen. Figure 4.6 (a) show no oxygen in the 5 mTorr depositions, while Fig. 4.6 (b) shows a significant quantity of oxygen in the 20 mTorr deposition. Most importantly, Fig. 4.6 (b) clearly shows that oxygen is uniformly distributed throughout the bulk of the film rather than just at the surface, as an oxide. This indicates that oxygen incorporation occurs as the film growths during deposition. These ratios cannot be compared directly with the Table 4.2 data as these depth profiles are not corrected for preferential sputtering.

The measured surface roughness of thin films deposited at 100 W (RF) power is presented in Table 4.2. This table indicates that the RMS roughness is dependent on the pressure the during deposition. The thin film deposited at a lower pressure exhibit a low RMS roughness, under 0.5 nm. Films deposited at a higher pressure of 20 mTorr have increased RMS roughness, near or above 1.0 nm. This increase in roughness could be due to incorporation of oxygen into the film or a change in the adatom energy of the arriving species. An increase in pressure leads to a decreased mean free path of a sputtered species. The mean free path λ is given by

$$\lambda = \frac{1}{\sqrt{2}\pi d_0^2 n}, \tag{4.1}$$

where d_0 is the diameter of the atom, and n is gas concentration of atoms at a given pressure [111]. The mean free path of a thermalized Ar atom at 10 mTorr is 0.77 cm, assuming an atomic radius of 0.30 nm. The mean free path of the same atom at 20 mTorr is 0.39 cm. In general, most sputtered atoms require about 10 to 25 collisions to become thermalized [130]. At a 10.15 cm spacing between the target and substrate, an atom undergoes approximately 13 collisions at 10 mTorr and 26 collisions at 20 mTorr. At the lower pressure there appear to be enough energetic atoms to create a smoother film, effectively peening the surface.

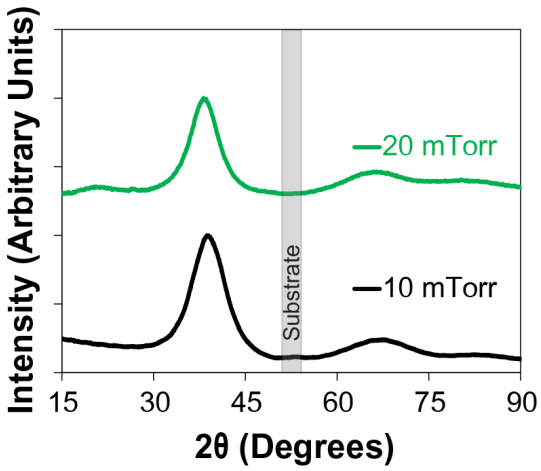

Figure 4.7: As-deposited x-ray diffraction (XRD) patterns for $Ta_{40}Mo_{40}Si_{20}$ thin films deposited at 100 W (RF) and 10 mTorr and 20 mTorr. A silicon substrate peak artifact is also identified.

The effects on $Ta_{40}Mo_{40}Si_{20}$ thin film resistivity by changing the power and pressure are listed in Table 4.2. Analysis of Table 4.2 leads to the conclusion that the thin film resistivity depends primarily on the deposition pressure. Films deposited at a higher deposition pressure have larger resistivities. This is likely due to an increase in oxygen concentration in comparison to the same material deposited at a lower pressure. Figure 4.6 (a) shows a low oxygen concentration throughout a $Ta_{40}Mo_{40}Si_{20}$ film deposited at 100 W (RF) power and 10 mTorr pressure. Table 4.2 shows that the resistivity of this $Ta_{40}Mo_{40}Si_{20}$ film is 177 $\mu\Omega - cm$. Alternatively, Fig. 4.6 (b) shows that oxygen is present uniformly throughout a film deposited at 100 W (RF) power and 20 mTorr pressure. Table 4.2 shows that the resistivity of a $Ta_{40}Mo_{40}Si_{20}$ film deposited at this conditions is 332 $\mu\Omega - cm$. This displays that the difference in resistivity is clearly due to oxygen incorporation into the thin film.

GI-XRD patterns for $Ta_{40}Mo_{40}Si_{20}$ films deposited at 10 mTorr and 20 mTorr are shown in Fig. 4.7. Both GI-XRD patterns are indicative of an amorphous thin film possessing

broad 2θ features from approximately 35 to 45° and 60 to 75°. The absence of any Bragg reflections or sharp, distinctive peaks indicates a lack of long-range crystalline order. While $Ta_{40}Mo_{40}Si_{20}$ XRD patterns do not significantly change with these changes in deposition conditions, this may not be the case for all of the materials and deposition conditions, i.e., thin films deposited at 30 mTorr may not possess an amorphous XRD pattern.

4.3 Thermal Studies

4.3.1 $Ta_{40}Ni_{40}Si_{20}$, $Ta_{40}Mo_{40}Si_{20}$, and $Ta_{40}Hf_{40}Si_{20}$ Thin Films

GI-XRD patterns of $Ta_{40}Ni_{40}Si_{20}$ thin films, heated in 100 °C increments in evacuated sealed tubes are presented in Fig. 4.8 (a). These XRD patterns exhibit no evidence of crystallization prior to 700 °C. As the temperature is increased to 700 °C, a broad feature, characteristic of diffuse scattering from a fully amorphous material, begins to change its shape. The nature of this change suggests that the formation and precipitation of nanocrystalline ordering is occurring within an amorphous matrix. As the temperature is increased to 800 °C, additional crystalline phases form, as indicated by the emergence of new distinct Bragg reflections; an amorphous fraction, however, remains at this temperature. The crystallization temperature of the $Ta_{40}Ni_{40}Si_{20}$ thin film is slightly less than that of a $Ta_{42}Ni_{38}Co_{20}$ bulk metallic glass, which has a crystallization temperature of 765 °C [90].

GI-XRD patterns for $Ta_{40}Mo_{40}Si_{20}$ thin films, annealed in 100 °C increments starting at 800 °C, are shown in Fig. 4.8 (b). The patterns contain no evidence of crystallization below 900 °C. As the temperature is increased to 900 °C, the broad amorphous feature begins to change shape, and crystalline peaks start to appear in the XRD pattern. As the temperature is increased to 1000 and 1100 °C, clear Bragg reflections are present, consistent with crystallization.

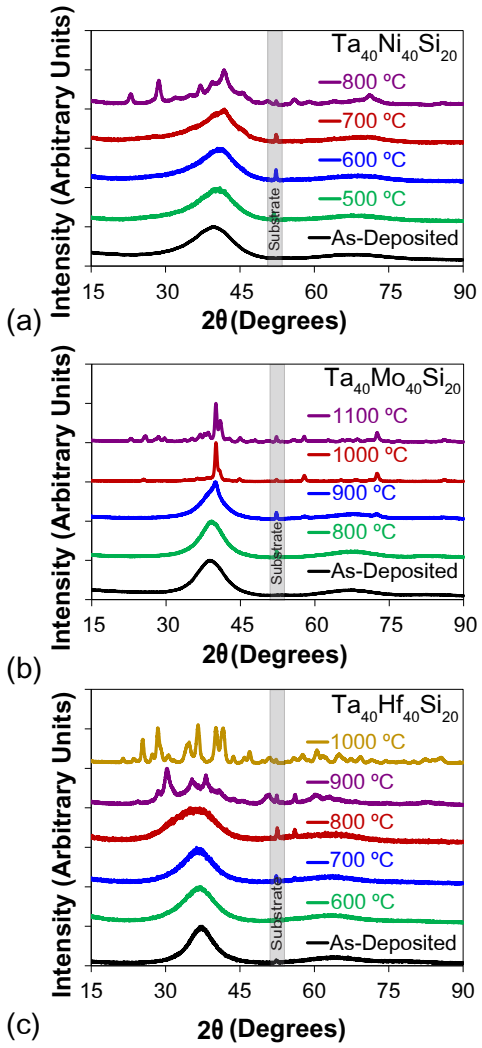

Figure 4.8: XRD patterns from (a) $Ta_{40}Ni_{40}Si_{20}$, (b) $Ta_{40}Mo_{40}Si_{20}$, and (c) $Ta_{40}Hf_{40}Si_{20}$ thin films as-deposited and after post-deposition annealing. The silicon substrate peak artifact at $\sim$52.5° is indicated.

GI-XRD patterns for $Ta_{40}Hf_{40}Si_{20}$ thin films, annealed in 100 °C increments starting at 600 °C, are shown in Fig. 4.8 (c). The patterns contain no evidence of crystallization below 600 °C. As the temperature is increased to 700 °C, the broad amorphous feature remains but a peak around 60 degrees appears. As the temperature is increased to 800 °C, the broad amorphous feature remains with the small feature at 60 degrees increases in intensity. As the temperature is increased to 900 °C, the broad amorphous feature begins to change shape, and

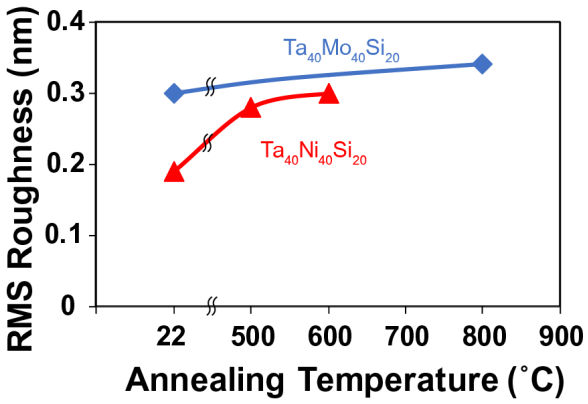

Figure 4.9: AFM roughness of $Ta_{40}Ni_{40}Si_{20}$ and $Ta_{40}Mo_{40}Si_{20}$ thin films after annealing at various temperatures prior to crystallization.

crystalline peaks start to appear in the XRD pattern. At 1000 °C, clear Bragg reflections are present, consistent with crystallization of the thin film.

Changes in surface roughness, caused by annealing below the crystallization temperature, are investigated by measuring the roughness of the thin film after annealing, as shown in Fig. 4.9. The measurements indicate a small increase in roughness of <0.1 nm after the annealing process. This shows that there is an insignificant increase in roughness, within that of the system noise. Roughness results after crystallization are not provided because of variation in results and delamination issues post crystallization. Prior to crystallization, the surface smoothness is minimally affected by the annealing treatment, demonstrating that these thin films can be used in applications in which a smooth surface is required, even after annealing to a relatively high temperature.

4.3.2 $Ta_xW_ySi_z$ Thermal Stability

GI-XRD patterns of $Ta_{40}W_{40}Si_{20}$, $Ta_{30}W_{50}Si_{20}$, and $Ta_{30}W_{30}Si_{40}$ thin films heated in 100 °C increments in evacuated sealed tubes are presented in Fig. 4.10. The $Ta_{40}W_{40}Si_{20}$ GI-XRD patterns shown in Fig. 4.10 (a) exhibit no evidence of crystallization prior to 1000

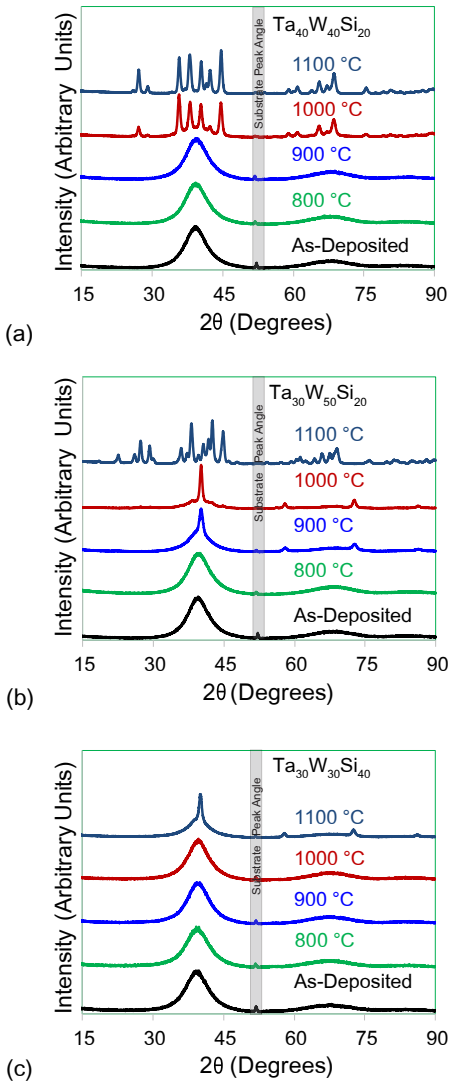

Figure 4.10: XRD patterns from (a) $Ta_{40}W_{40}Si_{20}$, (b) $Ta_{30}W_{50}Si_{20}$, and (c) $Ta_{30}W_{30}Si_{40}$ thin films as-deposited and after post-deposition annealing. The silicon substrate peak artifact at $\sim$52.5° is indicated.

°C. At 1000 °C, the broad scattering from the amorphous phase changes into sharp peaks due to the emergence of Bragg reflections from crystalline phases; an amorphous fraction, however, remains at this temperature. At 1100 °C, the amorphous contribution reduces as the Bragg reflection intensities increase due to crystal growth. Phase analysis shows that

the crystalline patterns at 1000 and 1100 °C originate from a Si_3W_5 crystal structure (see Appendix Fig. 8.2).

The $Ta_{30}W_{50}Si_{20}$ GI-XRD patterns shown in Fig. 4.10 (b) exhibit no evidence of crystallization below 900 °C, where crystalline peaks begin to arise from the amorphous matrix. As the anneal temperature increases to 1000 °C, the crystalline features continue to grow in intensity. The crystalline structure after both the 900 and 1000°C anneals correspond to tungsten or a solid solution of TaW, as shown in Appendix Fig. 8.3 (a) . After the 1100 °C anneal, the thin film undergoes a phase change into a mixed phase of Si_3W_5 with peaks at 22 and 30 degrees matching Si_2W (see Appendix Fig. 8.3 (b)). Note that a small amorphous fraction exists in the GI-XRD pattern after the 1000 °C anneal.

GI-XRD patterns for a $Ta_{30}W_{30}Si_{40}$ thin film are shown in Fig. 4.10 (c). The patterns contain no evidence of crystallization below 1100 °C. At 1100 °C, the broad amorphous feature develops Bragg reflections in the XRD pattern. The crystalline structure at 1100 °C matches that of tungsten or a solid solution of TaW (see Appendix Fig. 8.4). If the temperature were to be further increased, a silicide phase would likely form. The crystallization temperature of the $Ta_{30}W_{30}Si_{40}$ system (1000 - 1100 °C) is similar to that of quaternary amorphous metal systems based on Ta, W, Si, and C [24, 93], which is one of the highest crystallization temperatures found in literature. Meanwhile, the crystallization temperature of the $Ta_{40}W_{40}Si_{20}$ (900 - 1000 °C) and $Ta_{30}W_{50}Si_{20}$ (800 - 900 °C) thin films is slightly less than that of those other systems.

As seen in the crystallization process of both the $Ta_{30}W_{50}Si_{20}$ and $Ta_{30}W_{30}Si_{40}$ films, a fraction of the W and Ta metal first crystallizes, leaving behind a Si-rich amorphous matrix. As the temperature increases, Si is incorporated from the amorphous matrix into the

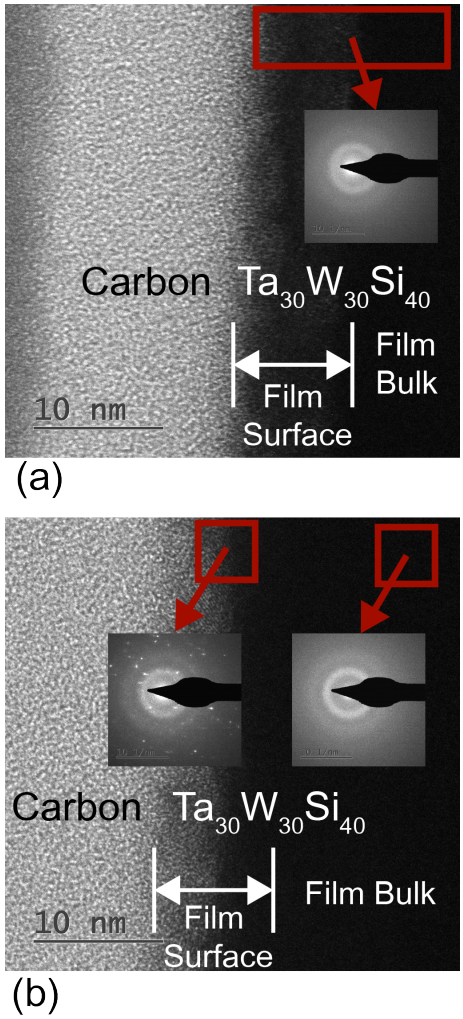

Figure 4.11: (a) TEM image a $Ta_{30}W_{30}Si_{40}$ thin film near the surface after a 1000 °C anneal with CBED pattern shown in the inset. (b) TEM image of a $Ta_{30}W_{30}Si_{40}$ thin film near the surface after a 1100 °C anneal with corresponding CBED patterns from the surface (left) and bulk (right) regions of the thin film. Note that an amorphous carbon preparation layer has been deposited on our thin films for FIB protection.

crystalline silicide. It is likely that the $Ta_{40}W_{40}Si_{20}$ crystallization process occurs in a similar manner, but over a narrower temperature range between 900 and 1000 °C.

A TEM image and CBED pattern of a $Ta_{30}W_{30}Si_{40}$ thin film surface after a 1000 °C anneal is shown in Fig. 4.11 (a). Diffuse rings present in the CBED pattern after the 1000 °C anneal confirm that the $Ta_{30}W_{30}Si_{40}$ thin film remains amorphous after the anneal at the

surface and throughout the entire bulk of the thin film. The surface of the film, labeled as film surface in Fig. 4.11 (a), becomes less dense after the anneal. This is indicated by the increased image brightness in comparison to that of the bulk of the film. The changes at the film surface could be due to the incorporation of residual oxygen in the sealed tube into the film during the anneal.

Figure 4.11 (b) is a TEM image and CBED analysis of a $Ta_{30}W_{30}Si_{40}$ thin film near the surface after a 1100 °C anneal. In the left CBED pattern of Fig. 4.11 (b), the crystalline nature of the film is confirmed at the film surface where bright diffraction reflections are present. Evidence of crystallization is also confirmed in the TEM image of the first 10 nm of the $Ta_{30}W_{30}Si_{40}$. The film surface shows orientation of crystalline grains which appear as distinct lines in Fig 4.11 (b) in the area labeled film surface, i.e., where the $Ta_{30}W_{30}Si_{40}$ film meets the carbon preparation layer. Similar to the 1000 °C anneal, the bulk of the film remains dense, as indicated by the dark regions in the TEM image in Fig. 4.11 (b). Additionally, the bulk of the film remains amorphous, as indicated by the diffuse halos in the right CBED image in Fig. 4.11 (b). The CBED analysis confirms that the $Ta_{30}W_{30}Si_{40}$ film remains amorphous to 1000 °C. Furthermore, the CBED and TEM analysis show that crystallization nucleates at the surface.

Figure 4.12 is a plot of surface roughness versus annealing temperature for three 200 nm thick $Ta_xW_ySi_z$ thin films. For all three thin films, the change in surface roughness is $<$0.2 nm prior to crystallization. The measured surface roughness is essentially that of the noise level of the instrument prior to crystallization. $Ta_{40}W_{40}Si_{20}$ films, which crystallize between 900 - 1000 °C, display a dramatic increase in RMS roughness from $<$0.5 nm to greater than 4 nm after annealing to 1000 °C. After annealing the film further to 1100 °C,

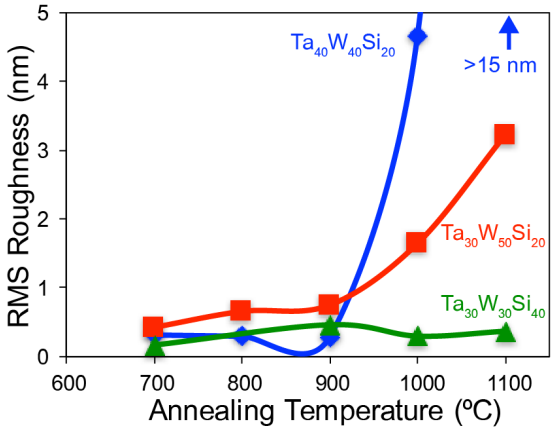

Figure 4.12: AFM roughness of $Ta_{40}W_{40}Si_{20}$, $Ta_{30}W_{50}Si_{20}$, and $Ta_{30}W_{30}Si_{40}$ thin films after annealing at various temperatures. Roughness increases upon crystallization.

the roughness increases to over 15 nm. The $Ta_{30}W_{50}Si_{20}$ thin film possesses a minimal increase in surface roughness of ∼0.3 nm after the 900 °C anneal. The diffraction pattern of the 900 °C sample retains a large amorphous contribution, indicating that a small amount of crystallization minimally changes the surface roughness. As the $Ta_{30}W_{50}Si_{20}$ thin film is annealed at a higher temperature, further crystallization occurs and the RMS roughness increases to ∼2 nm (1000 °C) and ∼3.2 nm (1100 °C). The $Ta_{30}W_{30}Si_{40}$ thin film trend is quite different, showing no significant change in RMS roughness even after crystallization is initiated at 1100 °C. As seen in Fig. 4.11 (b), only the near-surface portion of the $Ta_{30}W_{30}Si_{40}$ thin film has begun to crystallize 1100 °C, while a significant fraction of the film remains amorphous. This is further evidence of the superior thin film stability of the $Ta_{30}W_{30}Si_{40}$ thin film.

4.3.3 Discussion of Thermal Stability

Table 4.3 is a list of each material with its corresponding crystallization temperature. Crystallization temperature clearly correlates to the refractory nature of the constituent ele-

Table 4.3: Thin film materials developed in this dissertation and their corresponding crystallization temperature.

Material	**Crystallization Temp.** $[^{\circ}C]$
$Ta_{40}Ni_{40}Si_{20}$	600 - 700
$Ta_{40}Hf_{40}Si_{20}$	600 - 700
$Ta_{40}Mo_{40}Si_{20}$	800 - 900
$Ta_{30}W_{50}Si_{20}$	800 - 900
$Ta_{40}W_{40}Si_{20}$	900 - 1000
$Ta_{30}W_{30}Si_{40}$	1000 - 1100

ments. W possesses a melting temperature of 3422 °C, followed by Ta at 3020 °C, Mo at 2623 °C, Hf at 2231 °C, Ni at 1455 °C, and Si at 1414 °C. A 300 °C increase in crystallization temperature is achieved by moving from $Ta_{40}Ni_{40}Si_{20}$ to $Ta_{40}W_{40}Si_{20}$. Within the $Ta_xW_ySi_z$, optimizing the crystallization temperature requires further analysis.

The design guidelines state that more refractory constituent elements should achieve greater thermal stability. This guideline holds true when selecting the primary metals in the system, i.e., the crystallization temperature (T_X) of $Ta_{40}W_{40}Si_{20}$ >$Ta_{40}Mo_{40}Si_{20}$ >$Ta_{40}Hf_{40}Si_{20}$ >$Ta_{40}Ni_{40}Si_{20}$. However, when optimizing a material system, such as $Ta_xW_ySi_z$, a more refractory constituent element composition does not achieve greater thermal stability. This consideration suggests that the W-rich $Ta_{30}W_{50}Si_{20}$ would possess the highest thermal stability. However, it was found that W-rich $Ta_{30}W_{50}Si_{20}$ thin films crystallize at a 100 °C (200 °C) lower temperature than that of $Ta_{40}W_{40}Si_{20}$ ($Ta_{30}W_{30}Si_{40}$). A similar trend in which a W-rich amorphous metal crystallizes at a lower temperature than that of a Ta-

rich amorphous metal is reported by Ouyang et al. [93]. This trend may be due to a larger magnitude of the enthalpy of mixing of Ta-Si, -56 kJ^{-1}-mol^{-1}, compared to that of W-Si, -31 kJ^{-1}-mol^{-1} [85].

Finally, to maximize thermal stability, the design guidelines suggest that a critical metalloid content of 20% is needed in the thin film composition. The results of our thin-film study is consistent with this guideline. Increasing the silicon content in the sputter target from 20%, $Ta_{40}W_{40}Si_{20}$ (or $Ta_{30}W_{50}Si_{20}$) to 40%, $Ta_{30}W_{30}Si_{40}$ leads to an increased thin film composition of 20% Si. The $Ta_{30}W_{30}Si_{40}$ thin film possesses the highest crystallization temperature.

4.4 Oxidation Studies

The crystallization study revealed that all six amorphous metals possess adequately thermal stability for TIJ applications. The $Ta_xW_ySi_z$ system outperforms the other materials by more than 200 °C. Because of their superior thermal stability, $Ta_{40}W_{40}Si_{20}$ and $Ta_{30}W_{30}Si_{40}$ systems are the focus of the oxidation study. The oxidation study presented here consists of annealing thin films at 300, 500, and 700 °C for set times and evaluation of the structure and stability of the oxide in comparison to that of a Ta thin film.

An ideal amorphous metal grows a passivating oxide on the surface, thereby forming corrosion barrier. This type passivation is ideal for the TIJ environment. The oxidation study herein uses XRR and TEM to investigate how the oxide forms on the AMTF surface. Ellipsometry models are used to calculate the oxide thickness as it forms on the AMTF. GI-XRD and AFM are then used to confirm the structure and surface morphology of the oxide. Finally, XPS is used to determine the composition of the oxide.

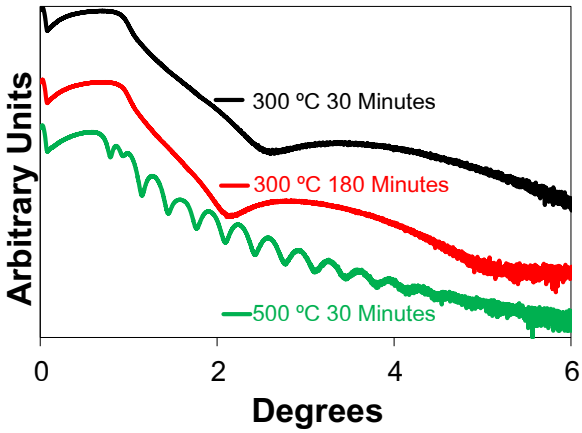

Figure 4.13: XRR patterns of $Ta_{30}W_{30}Si_{40}$ thin films after annealing at 300 °C for 30 minutes, 300 °C for 180 minutes, and 500 °C for 30 minutes in air.

4.4.1 Oxidation Process and Growth Rates

Figure 4.13 displays XRR patterns from $Ta_{30}W_{30}Si_{40}$ thin films annealed at 300 °C for 30 and 180 minutes and at 500 °C for 30 minutes. The XRR pattern of the thin films annealed at 300 °C are indicative of a thin oxide on top of the metal. As the annealing time increases from 30 to 180 minutes, an inflection point shifts from $\sim 3^\circ$ to almost $\sim 2.25^\circ$, indicating the presence of a slightly thicker oxide on the metal surface. After a 30 minute anneal at 500 °C, the critical angle shifts to $\sim 0.5^\circ$ and multiple interference fringes occur in the pattern. The shift in critical angle is due to the growth of a thicker, lower density oxide on the AMTF surface. The development of interference fringes is also due to the growth of a thicker oxide on the surface. These XRR patterns are evidence these amorphous metals passivate in an ideal manner amorphous metal with the growth of a uniform surface oxide.

To confirm formation of a surface oxide on the thin film, TEM cross-sections of annealed $Ta_{30}W_{30}Si_{40}$ films are analyzed. Figure 4.14 (a) is a $360k\times$ TEM cross-section of a $Ta_{30}W_{30}Si_{40}$ thin film after annealing in air at 300 °C for 180 minutes. A thin ~ 3 nm surface

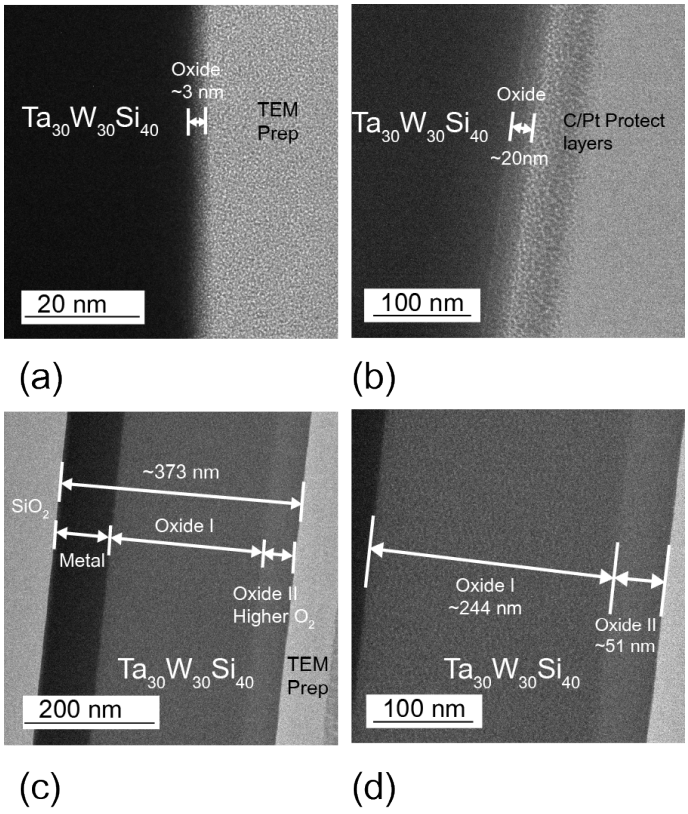

Figure 4.14: TEM images of the oxide growth on a $Ta_{30}W_{30}Si_{40}$ thin film after annealing in air at (a) 300 °C for 180 minutes (360$k\times$ magnification), (b) 500 °C for 15 minutes (66$k\times$ magnification), and (c) 700 °C for 15 minutes (40$k\times$ magnification). (d) A higher magnification TEM image (66$k\times$ magnification) of the oxide growth on a $Ta_{30}W_{30}Si_{40}$ thin film after annealing in air at 700 °C for 15 minutes explicitly showing the thicknesses of the two distinct oxides.

oxide forms after annealing at 300 °C for 180 minutes. Figure 4.14 (b) is a 66$k\times$ TEM image of a $Ta_{30}W_{30}Si_{40}$ thin film after annealing in air at 500 °C for 15 minutes. A 20 nm surface oxide is seen on the surface of the amorphous metal.

Figure 4.14 (c) and (d) are TEM cross-sections of a $Ta_{30}W_{30}Si_{40}$ thin film after annealing in air at 700 °C for 15 minutes. As the temperature increases to 700 °C, a more complicated oxide forms on the metal surface. Two distinct oxide regions are observed on the amorphous metal thin film surface, as seen in Fig. 4.14 (c). Figure 4.14 (d) is a higher magnification of these oxides with thickness measurements. A 51 nm thick lower density ox-

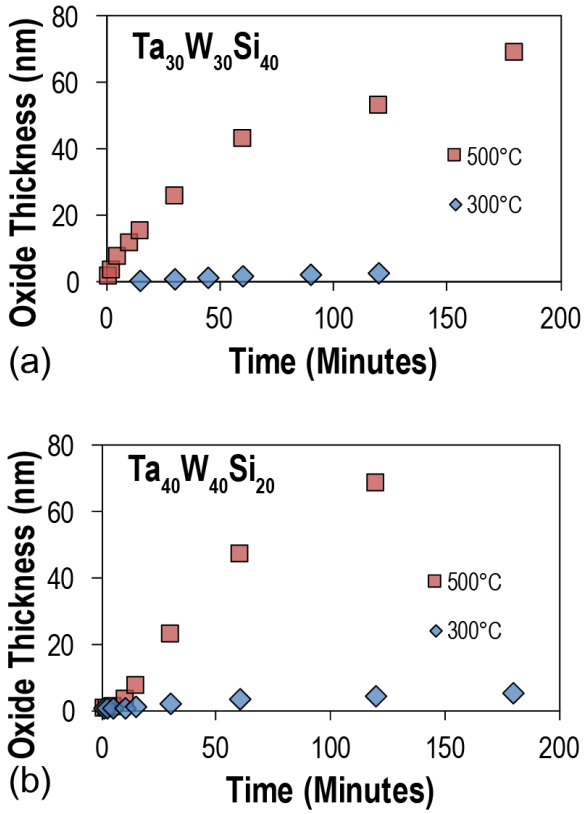

Figure 4.15: Oxide thickness, determined by spectroscopic ellipsometery of (a) $Ta_{40}W_{40}Si_{20}$ and (b) $Ta_{30}W_{30}Si_{40}$ thin films after annealing at various times and temperatures in air.

ide is at the top surface and the second oxide is measured to be 244 nm thick directly above the AMTF. The total thickness of the thin film has expanded by >150 nm due to the incorporation of oxygen. The formation of multiple oxide layers is discussed further in Sect. 4.4.3.

Figure 4.15 (a) and (b) are plots of oxide thickness versus annealing time for $Ta_{30}W_{30}Si_{40}$ and $Ta_{40}W_{40}Si_{20}$ thin films. At 300 °C, $Ta_{30}W_{30}Si_{40}$ is found to form a thin passivating oxide <5 nm thick. After an anneal at 300 °C for 180 minutes, a $Ta_{30}W_{30}Si_{40}$ thin film forms an oxide modeled to be 3.2 nm by ellipsometry, 2.34 nm by XRR, and measured as 3 nm by TEM. At 500 °C, a thicker oxide forms, as expected. After an anneal at 500 °C for 30 minutes the oxide growth is modeled as 25.71 nm with ellipsometry and 24.88 nm with XRR. After an

anneal at at 500 °C for 720 minutes, a 99 nm thick oxide can be modeled with ellipsometry (data point not shown in Fig. 4.15 (a)). For both the 300 and 500 °C anneals, as the annealing time increases, the growth rate decreases. This indicates that a passivating oxide is forming at these temperature, as desired for the TIJ application. Due to the more complicated nature of the oxide formed, it is difficult to estimate the oxide thickness at 700 °C with ellipsometry.

Figure 4.15 (b) is a plot of oxide thickness versus annealing time for $Ta_{40}W_{40}Si_{20}$ thin films. Similar to the $Ta_{30}W_{30}Si_{40}$ thin films, the 300 °C anneals form a very thin surface oxide that models <5 nm thick. As the temperature is increased to 500 °C, a thicker oxide grows on the surface and appears to saturate at a thickness of ∼70 nm. The $Ta_{40}W_{40}Si_{20}$ composition oxidizes at a slightly faster rate than that of the $Ta_{30}W_{30}Si_{40}$, but still possesses the desirable features of a passivating oxide.

4.4.2 Oxide Structure

Figure 4.16 (a) are GI-XRD patterns for thin films annealed at 300, 500, and 700 °C for 30 and 180 minutes. The GI-XRD patterns of the thin films annealed at 300 °C possess no change in comparison to the as-deposited films seen in Fig. 4.4. Only the broad features with peaks at approximately 40° and 66° from the amorphous metal are in the pattern. The GI-XRD pattern of the thin film annealed at 500 °C for 30 minutes is a close match to the as-deposited amorphous metal. After an anneal at at 500 °C for 180 minutes, new, broad XRD features develop peaks at ∼25° and ∼30°. As the temperature is increased to 700 °C the GI-XRD pattern significantly changes with broad peaks centered at 25°, 35°, and 60° 2θ.

The evolution of the GI-XRD patterns is attributed to the growth of a surface oxide. There is no difference between the GI-XRD pattern from the bare metal and those after annealing at 300 °C or 500 °C for 30 minutes since only a thin oxide grows (i.e., a ∼25 nm

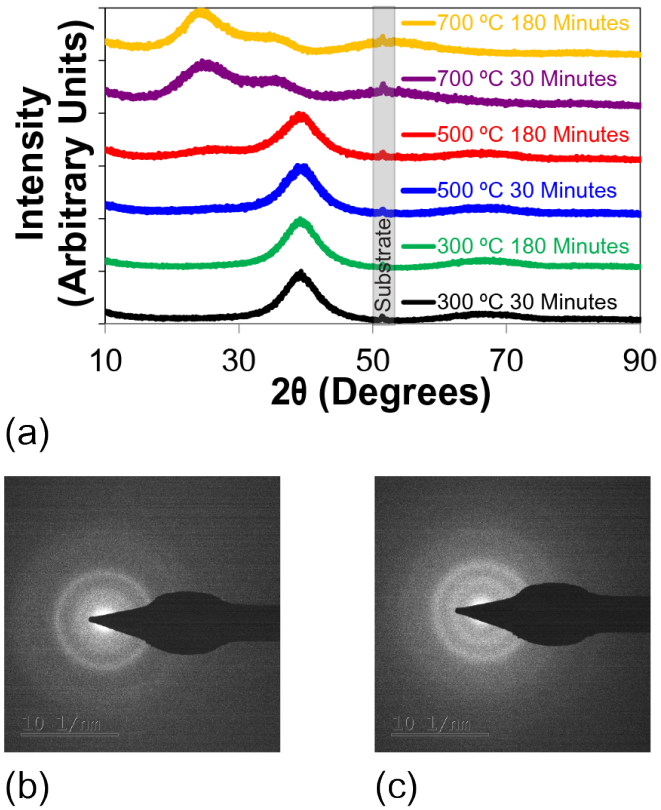

Figure 4.16: (a) GI-XRD patterns for $Ta_{30}W_{30}Si_{40}$ thin films after annealing in air at various temperatures and times. The silicon substrate peak artifact at ∼52.5° is indicated. Selected area electron diffraction (SAED) patterns from (b) the amorphous metal thin film and (c) Oxide I after annealing at 700 °C for 15 minutes, shown in the TEM image in Fig. 4.14 (c)

oxide contributes a small fraction of the scattering in comparison to the ∼200 nm thin film). After an anneal at 500 °C for 180 minutes, a 70 nm oxide begins to contribute to the GI-XRD pattern. Finally, after annealing at 700 °C, the metal thin film is almost consumed by the oxide and the GI-XRD pattern represents that of the resulting oxide. The two broad peaks at ∼25° and ∼30° 2θ correspond to scattering from amorphous SiO_2 and Ta_2O_5.

Selected area electron diffraction (SAED) is used to confirm the structure of the oxide and changes to the amorphous metal after the air anneals. Figure 4.16 (b) is a SAED pattern of the amorphous metal after an anneal at 700 °C for 15 minutes, as seen in Fig. 4.14 (c).

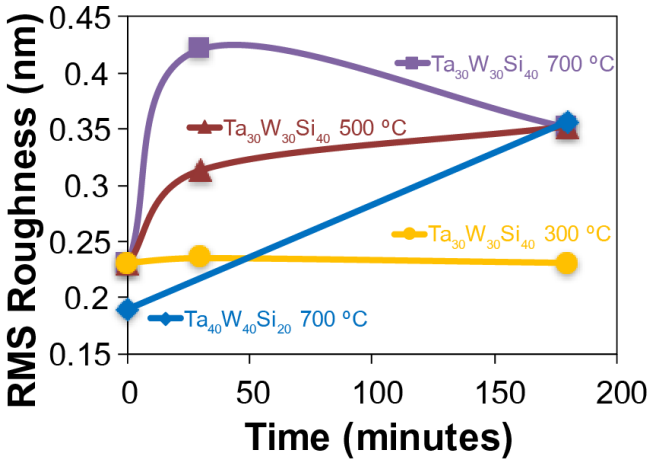

Figure 4.17: RMS roughness of $Ta_{30}W_{30}Si_{40}$ and $Ta_{40}W_{40}Si_{20}$ thin films after annealing in air at various temperatures and times.

The diffuse halos confirm the amorphous structure and are similar to that of the as-deposited CBED pattern in Fig. 4.5 (e). Figure 4.16 (c) is the SAED pattern of the Oxide I region formed after an anneal at 700 °C for 15 minutes, as seen in Fig. 4.14 (c) and (d). The diffuse halos are supporting evidence that an amorphous oxide is forming on the amorphous metal surface.

Figure 4.17 is a plot of RMS roughness versus annealing time for $Ta_{30}W_{30}Si_{40}$ thin films annealed at 300, 500, and 700 °C and for a $Ta_{40}W_{40}Si_{20}$ thin film annealed at 700 °C. There no change in surface roughness after annealing $Ta_{30}W_{30}Si_{40}$ at 300 °C. After the 500 and 700 °C anneals, all thin films exhibit a minimal change in surface roughness. This minimal change in surface roughness is evidence that an amorphous oxide is growing on the AMTF surface. Similar to the $Ta_{30}W_{30}Si_{40}$ system, the $Ta_{40}W_{40}Si_{20}$ thin films possesses minimal change in surface roughness after an anneal at 700 °C for 180 minutes, as seen in Fig. 4.17.

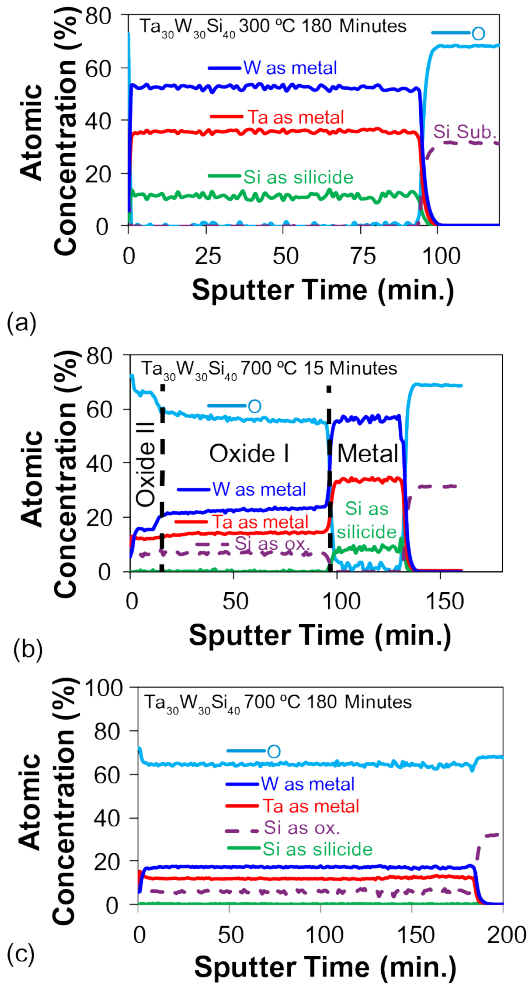

Figure 4.18: XPS elemental and chemical state depth profiles of $Ta_{30}W_{30}Si_{40}$ thin films after annealing in air for (a) 180 minutes at 300 °C, (b) 15 minutes at 700 °C, and (c) 180 minutes at 700 °C.

4.4.3 Oxide Composition

Figure 4.18 shows three XPS sputter depth profiles of $Ta_{30}W_{30}Si_{40}$ thin films annealed in air. Figure 4.18 (a) is an XPS sputter depth profile of a thin film annealed at 300 °C for 180 minutes. This profile is consistent with the formation of a superficial surface oxide and no oxygen penetration into the bulk of the thin film. Figure 4.18 (b) is a XPS sputter depth profile of a thin film annealed at 700 °C for 15 minutes in air showing the formation of three distinct regions labeled Oxide II, Oxide I, and the Metal region. Oxide II possesses the

highest oxygen concentration, Oxide I possesses a lower oxygen concentration, and Metal is the remaining unoxidized metal thin film. These three regions are consistent with the layers found in the TEM analysis, as seen in Fig. 4.14 (c). After a thin film is annealed at 700 °C for 180 minutes in air, the entire thin film is oxidized, as seen in Fig. 4.18 (c).

Four key observations are made from the chemical state analysis or the thin film annealed at 700 °C for 15 minutes as the example case. First, the surface oxide consists of all of the constituent elements in their respective oxidation states. Second, Si is in the oxidized state in all of the passivating oxides, i.e., Si is oxidized in both Oxide I and Oxide II. Third, Ta is only found to be in an oxidized state in the oxygen rich-region of the annealed film, i.e., Oxide II. Finally, W is not found to be in an oxidized state in any portion of the thin film. Thus, the passivation layer is a process involving (i) oxygen diffusion into the film, (ii) preferential oxidation of silicon, and (iii) subsequent oxidation of Ta.

The Gibbs free energy of oxidation for each of constituent element provides a framework to understanding the oxidation behavior just described. The Gibbs free energies of SiO_2, Ta_2O_5, and WO_3 are -68.2, -65.2, and -45.6 kCal-(gm-atom)$^{-1}$, respectively [131]. Thus, energetically formation of SiO_2 is first expected, followed by Ta_2O_5, and finally WO_3. As the initial passivation oxide grows in thickness, it creates a larger diffusion barrier for oxygen to penetrate into the bulk of the thin film. The larger diffusion barrier results in Ta oxidizing near the thin film surface and forming the second oxide layer.

4.5 Stability of Ta thin films

Sputtered Ta thin films are significantly rougher and display poorer thermal stability in comparison to the amorphous $Ta_{30}W_{30}Si_{40}$ thin films discussed herein. A 200-nm Ta thin

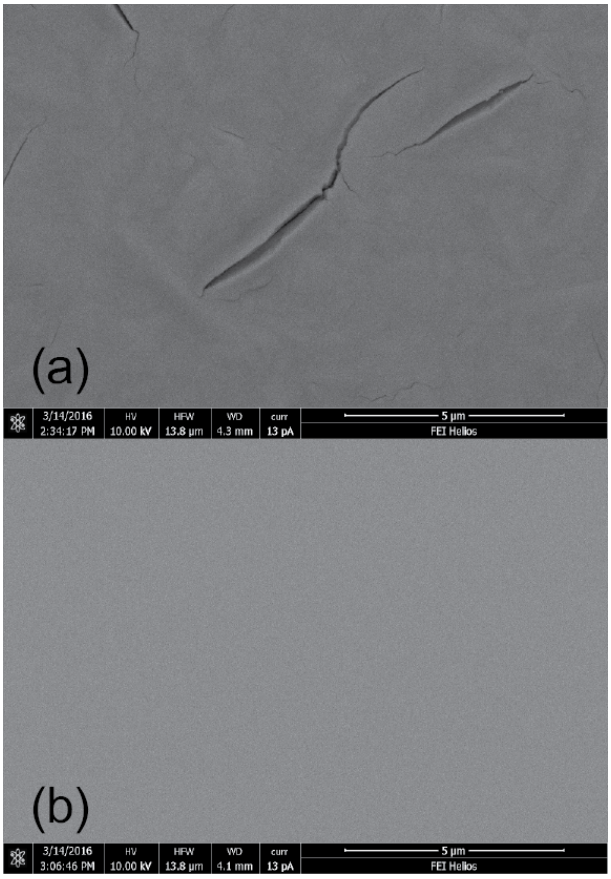

Figure 4.19: a) Surface of a 200 nm Ta thin film after a 700 °C anneal in air for 10 minutes, showing cracking of the surface. (b) Surface of a 200 nm $Ta_{40}W_{40}Si_{20}$ thin film after an anneal at 700 °C in air for 10 minutes, showing an undamaged surface.

film possesses an as-deposited roughness greater than 1 nm. Sputter deposition typically results in a Ta hexagonal β-phase thin film with a resistivity of 165 $\mu\Omega - cm$ (α-Ta possesses resistivity of 25 $\mu\Omega - cm$) [132]. β-phase Ta thin films begin to transition to the α phase near 700 °C, and complete this transition below 800 °C. After annealing at 700 and 800 °C, the RMS surface roughness approaches 2.0 nm and rises to 2.2 nm, respectively.

Sputtered Ta thin films also suffer from mechanical integrity issues after high temperature annealing in an oxidizing environment. This is seen in Fig. 4.19 (a), where cracking develops on the surface of a 200 nm Ta thin film after an anneal at 700 °C for 10 minute . In

addition to cracking, the Ta thin film becomes significantly rougher as it oxidizes with RMS roughness increasing to over 2 nm after annealing at 700 °C. The cracking of a Ta thin film during exposure to the high-temperature oxidizing environment frequently results in delamination from the substrate and/or complete degradation of the thin film into a powder. Similar Ta thin film instability trends have been reported by others [48] and can occur starting at 500 °C when annealing in air.

Figure 4.19 (b) is an SEM image of a $Ta_{40}W_{40}Si_{20}$ thin film surface after a 10 minute anneal at 700 °C. The amorphous thin film retains its ultra-smooth surface and mechanical integrity. The change in RMS surface roughness of a $Ta_{40}W_{40}Si_{20}$ thin film is negligible after the 700 °C anneal in an oxidizing environment. Similar results are found for $Ta_{30}W_{30}Si_{40}$ thin films.

4.6 Materials Analysis Summary

The $Ta_xW_ySi_z$ system possesses many advantageous properties in comparison to that of the conventional TIJ thin film material, i.e., thin film β-phase Ta. The as-deposited structure is confirmed to be amorphous through XRD, electron diffraction, and TEM analysis. A crystallization study found that $Ta_{30}W_{30}Si_{40}$ thin films are stable at temperatures up to 1000 °C. An oxidation study revealed that $Ta_xW_ySi_z$ passivation occurs through the creation of a stable amorphous oxide layer. This is desirable for TIJ applications. The passivation layer formed on $Ta_xW_ySi_z$ thin films is more stable compared to that of β-phase Ta thin films. This too is desirable for TIJ applications.

5. $TA_{30}W_{30}SI_{40}$ TIJ RESISTORS

This chapter presents the characterization of as-fabricated thermal inkjet (TIJ) resistors, nucleation studies for TIJ operation, and the materials analysis of amorphous metal thin film (AMTF) TIJ resistors after testing. First, as-fabricated properties of $Ta_{30}W_{30}Si_{40}$ resistors are presented, including device dimensions, SEM surface analysis, and electrical properties. Next, a nucleation study is presented. The nucleation study is used to determine the minimal firing parameters, i.e., voltage and pulse width, to create homogeneous nucleation. A lifetime assessment is performed to determine the number of pulses at a given power a resistor can withstand before failure at a given operating point. Finally, a set of TIJ resistors are tested to $\sim$60% of their lifetime and a materials analysis is performed. The materials analysis confirms the that AMTF remains amorphous after testing in the TIJ environment and retains its advantageous amorphous properties.

5.1 As-Fabricated Device Characterization

50$\times$ optical microscope images representative of as-fabricated 30 μm^2 devices are shown in Fig. 5.1. The TIJ resistor length (L) and width (W) are shown between the two Al traces. The $Ta_{30}W_{30}Si_{40}$ thin film is under the Al traces and patterned to wider dimension than that of the traces in order to avoid misalignment. Due to variations in mask dimensions and over-etching, the average device dimensions are $\sim$29.5 μm by $\sim$29.5 μm. Photo-mask imperfections, i.e., the jagged features at edges or 'mouse bites', are transferred into the actual device pattern. Particularly bad areas of mouse-bite features are indicated by '**' in Fig. 5.1 (c). These non-uniformities contribute to resistance variations between devices and

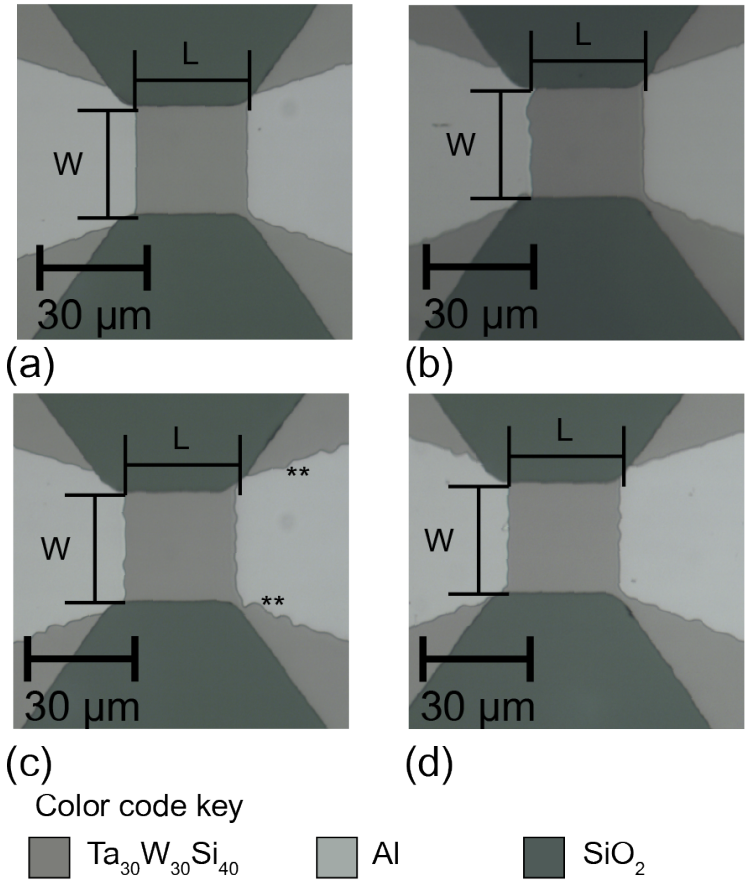

Figure 5.1: 50× optical microscope images of four as-fabricated TIJ resistors. Dark gray regions are the amorphous metal thin film, lighter gray regions are aluminum traces, and green areas are the SiO_2 substrate. The resistors length and width are indicated for each resistor.

may lead to non-uniform heating, resulting in hot spots for nucleation to initiate, as discussed in Sect. 5.2.

Figure 5.2 (a) and (b) are SEM images representative of an as-fabricated TIJ resistor. Measurements from Fig. 5.2 (a) confirm that the device dimensions are ∼29.5 μm by ∼29.5 μm. Figure 5.2 (a) also shows an example of flagging where an undersired portion of the amorphous metal remains, as seen at the top left of the image. Fig. 5.2 (b) is a higher magnification image of the resistor surface. While the thin film surface possesses no evidence of crystalline grains, some surface features are observed. These features are likely due the

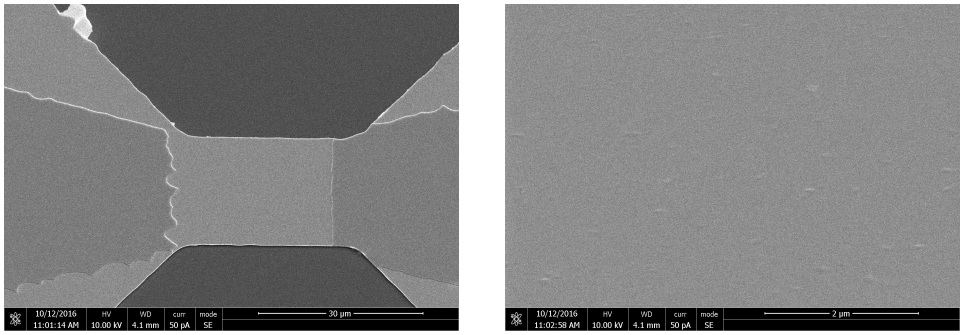

Figure 5.2: (a) A $5k\times$, 45° SEM image of an untested TIJ resistor. (b) A higher magnification, $20k\times$, 45° SEM image of the untested resistor surface showing some features due to process integration.

fabrication process. The liftoff process requires application and development of photoresist in areas of the substrate where the patterned AMTF remains. The development process and a plasma ash may not remove all of the photoresist from these areas. When the AMTF is deposited onto these areas, any surface features from residual photoresist on the substrate are transfered to the resistor surface. Due to these features, AFM analysis is not presented.

Figure 5.3 (a) is a plot of resistance versus distance from three transmission line measurements (TLM) used to confirm the resistivity of the patterned $Ta_{30}W_{30}Si_{40}$ thin film. The TLM measurements calculate the resistivity to be 219, 225, and 239 $\mu\Omega - cm$ for three sampled depositions. Two of these measurements, 219 and 225 $\mu\Omega - cm$, are in good agreement with the as-deposited thin film resistivity of 219 $\mu\Omega - cm$, as reported in Sect. 4.1. The third TLM possesses a higher resistivity, this could be due to a higher concentration of residual oxygen in the chamber at the time of deposition or a misaligned substrate location during the deposition.

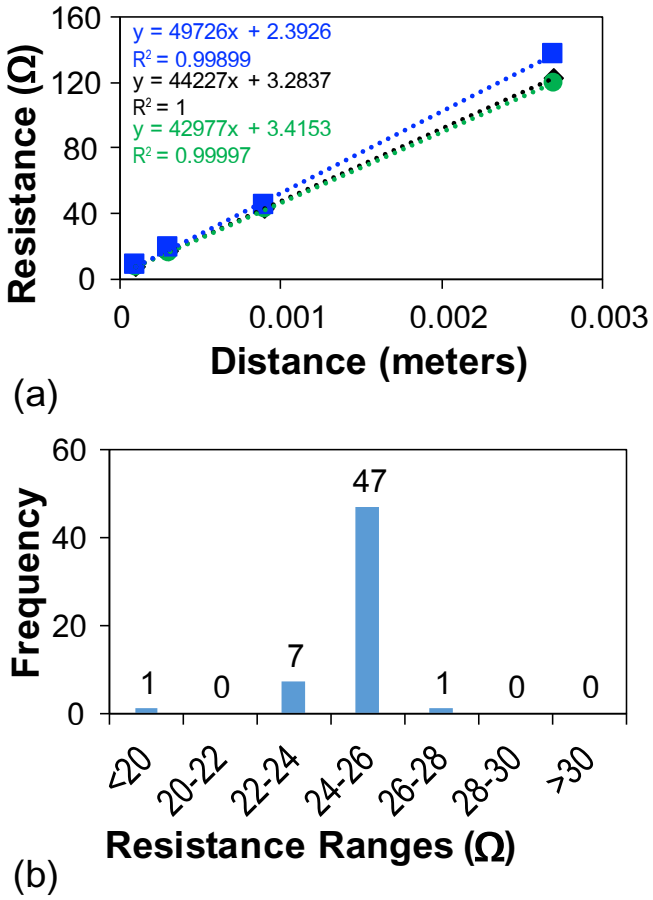

Figure 5.3: (a) Transmission line measurement (TLM) resistance versus spacing from three as-fabricated TLM structures used to calculate $Ta_{30}W_{30}Si_{40}$ resistivity. (b) Histogram of measured device resistance from 56 resistors and seven separate substrate depositions.

Figure 5.3 (b) is a histogram of resistance values measured from 56 as-fabricated resistors. The as-fabricated devices show little variation in resistance with an average resistance of 25.11 $\pm$ 0.71 Ω. The outlier at $<$20 Ω is due to a fabrication error and a portion of the aluminum trace shorting the resistor. The small variation in device resistance leads to less variation of the turn-on energy.

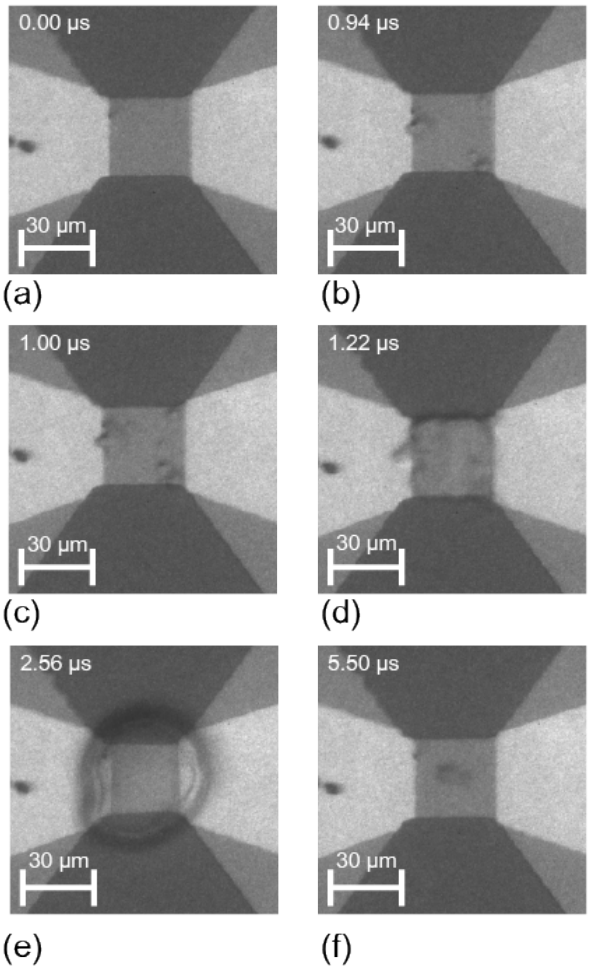

Figure 5.4: 60× water immersion microscope image series of a firing event generated from a 1.5 μs @ 5V input pulse. The series captures the bubble at (a) prior to the firing event, (b) the start of non-homogeneous nucleation, (c) the growth of non-homogeneous bubbles, (d) the merging of all nucleation points into homogeneous nucleation, (e) the time of maximum bubble size, and (f) the point of initial bubble collapse and cavitation.

5.2 Nucleation Study and Turn-On Energy Analysis

For the nucleation study, input pulse widths of 1.5, 3, 6, and 12 μs are used and the input voltage is increased by increments of 0.25 V until homogeneous nucleation is observed. A high-speed camera is used to observe if nucleation occurs at a set input pulse width and voltage in order to determine the minimum turn-on energy. The minimum turn-on energies found in the nucleation study are a 1.5 μs pulse width at a 5 V input (1.5 μs @ 5 V input

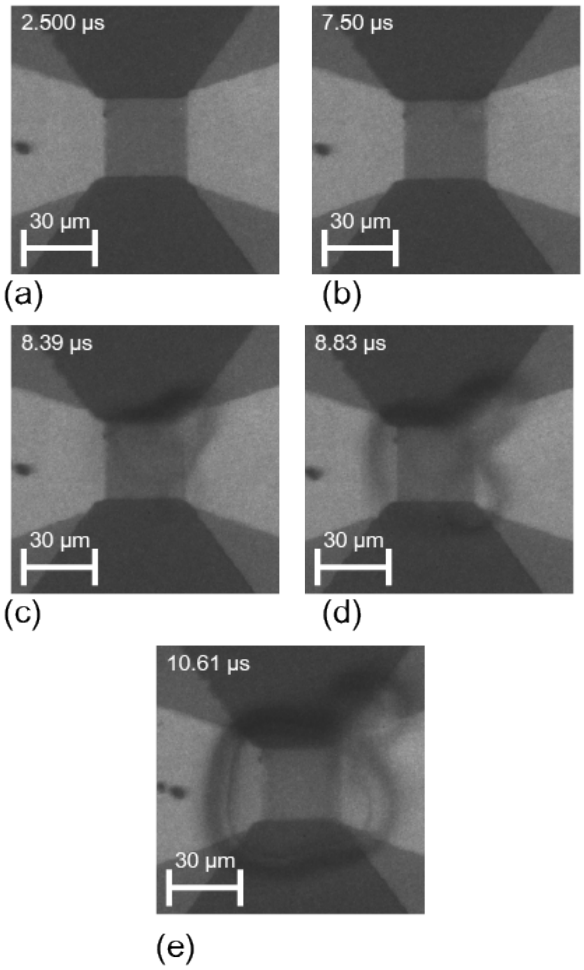

Figure 5.5: 60× water immersion microscope image series of a firing event generated from a 12 μs @ 3.5 V input pulse. The series captures the bubble at (a) prior to the firing event, (b) the start of non-homogeneous nucleation on the top right corner of the resistor, (c) the growth of non-homogeneous bubbles, (d) the merging of all nucleation points into homogeneous nucleation, and (e) the time of maximum bubble size.

pulse), 3 μs pulse width at a 4.25 V input (3 μs @ 4.25 V input pulse), 6 μs pulse width at a 4 V input (6 μs @ 4 V input pulse), and 12 μs input pulse width at a 3.5 V input (12 μs @ 3.5 V input pulse). The nucleation study is performed multiple times on the same device in order to eliminate the effects of variability that may influence the turn-on energy. A minimum turn-on energy is measured for five different devices in order to evaluate device-to-device variability.

Figure 5.4 is a series of images capturing bubble formation initiated from a 1.5 μs @ 5 V input pulse. A 1.5 μs input pulse width requires a minimum input voltage of 5 V to initiate homogeneous nucleation. Micro-boiling events, or the formation of several discrete bubbles, starts to occur at $\sim$1.0 μs with a 5 V input, as seen in Fig. 5.4 (b) and (c). Micro-boiling events occur at hot spots on the resistor surface, likely due to an increased current density or current crowding. The increased current density arises as a consequence of the physical layout of the resistor and/or mouse-bite features creating variations in the resistor dimensions. At $\sim$1.22 μs, into the pulse width, homogeneous nucleation occurs directly over the resistor surface, as seen in Fig. 5.4 (d). The maximum bubble size occurs at $\sim$2.56 μs, followed by bubble collapse at the center of the resistor after $\sim$5.5 μs, as seen in Fig. 5.4 (e) and (f), respectively.

Figure 5.5 is a series of images capturing bubble formation initiated from a 12 μs @ 3.5 V input pulse to initiate homogenous nucleation. A 12 μs input pulse width requires a minimum input voltage of 3.5 V. Using this lower input voltage results in an increase in pulse time to $\sim$7.5 - 8.39 μs for micro-boiling to initiate, as seen in Fig. 5.5 (b) and (c). Homogeneous nucleation begins to occur at a pulse time of $\sim$8.83 μs and occurs at the resistor, parts of the trace, and the substrate, as seen in Fig. 5.5 (d). This nucleation away from the resistor surface is likely due to the longer heating duration prior to nucleation, resulting in heat transfer to other areas near the device. The bubble reaches a maximum size at $\sim$10.6 μs after the pulse was initiated, as seen in Fig. 5.5 (e). The bubble vanishes $\sim$15 μs after the input pulse was initiated.

It is found that a larger (smaller) input voltage and shorter (longer) pulse width creates homogeneous nucleation more (less) rapidly and that the bubble lasts for a shorter (longer)

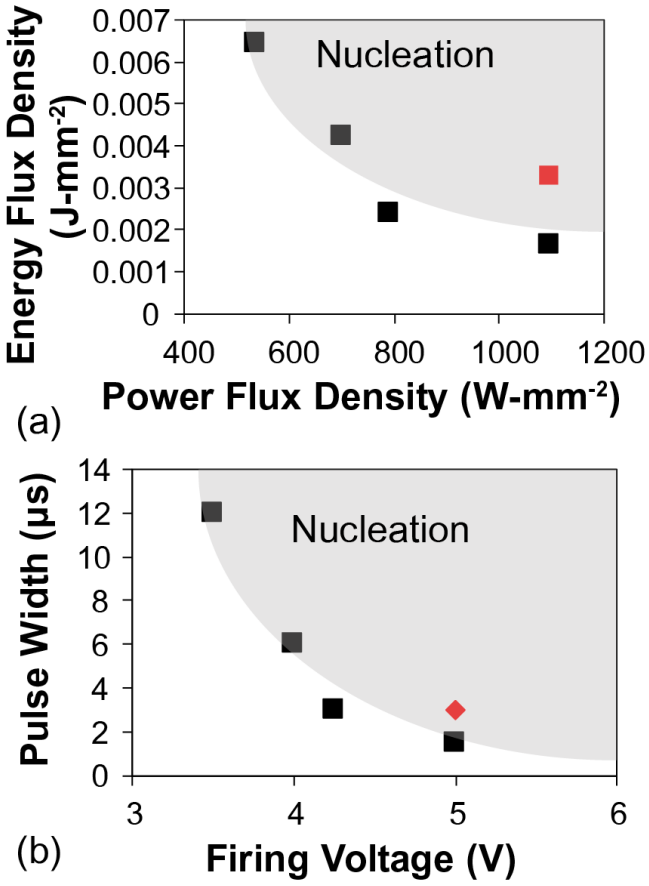

Figure 5.6: (a) A plot of energy flux density versus power flux density indicating the minimum energy needed to nucleate a homogeneous bubble. (b) A plot of input pulse width versus input voltage, indicating the minimum pulse width required for nucleation at given voltage. In both plots the shaded gray region indicates where nucleation occurs. The red marker is the minimum energy-power (pulse width-voltage) used in the lifetime testing.

duration, as expected. Bubble formation is quite different when using a different input voltage. A larger voltage creates a bubble directly over the resistor, as desired, while a smaller voltage creates a larger bubble due to an increased pulse width and associated peripheral heating. From this study, the bubble size can be compared in the x-and y-direction, but not in the z-direction. Thus, a determination of the actual bubble volume cannot be accomplished.

Turn-on energies determined in the nucleation study are converted to input energy flux density versus input power flux density, as shown in Fig. 5.6 (a). This normalization allows

for a comparison to other reports, such as those from Einat [133]. The input energy flux density versus input power flux density is similar to that reported by Eniat. For example, Einat reports an input power flux density of 800 $W-mm^{-2}$ requires 0.009 $J-mm^{-2}$ compared to the 0.0025 $J-mm^{-2}$ value shown in Fig 5.6 (b). This discrepancy likely arises from differences in losses in the system, such as differences in trace design, device layout, and/or the substrate thermal oxide thickness.

Figure 5.6 (b) is a plot of the input pulse width versus firing (input) voltage required for homogeneous nucleation. As the firing voltage decreases, a non-linear increase in pulse width is required in order to initiate nucleation. A 3 μs pulse width is used for lifetime testing. A 3 μs pulse width minimizes electrical signal non-idealities, i.e., overshoot or ringing of the input voltage, while limiting thermal losses to the system. The red markers shown in Fig. 5.6 (a) and (b) indicate, respectively, the minimum energy-power and voltage-pulse width points used for lifetime testing. This lifetime testing point is well above the minimum required for nucleation in order to be assured of bubble formation throughout the entire duration of the lifetime test.

5.3 Lifetime Analysis

A lifetime study is used to test the mechanical feasibility of using $Ta_{30}W_{30}Si_{40}$ resistors in a simulated TIJ environment. The test used in this study is known as an open-pool test. In the open-pool test conducted, a TIJ resistor is submerged directly into water. Thus, this test is performed without the use of a fluidic channel or of corrosive inks as in the case of a real TIJ device, as described in Sect. 2.1. The lack of a fluidic channel and ink ejection creates more severe cavitation damage compare to that of a real TIJ device. Thus, an open-pool

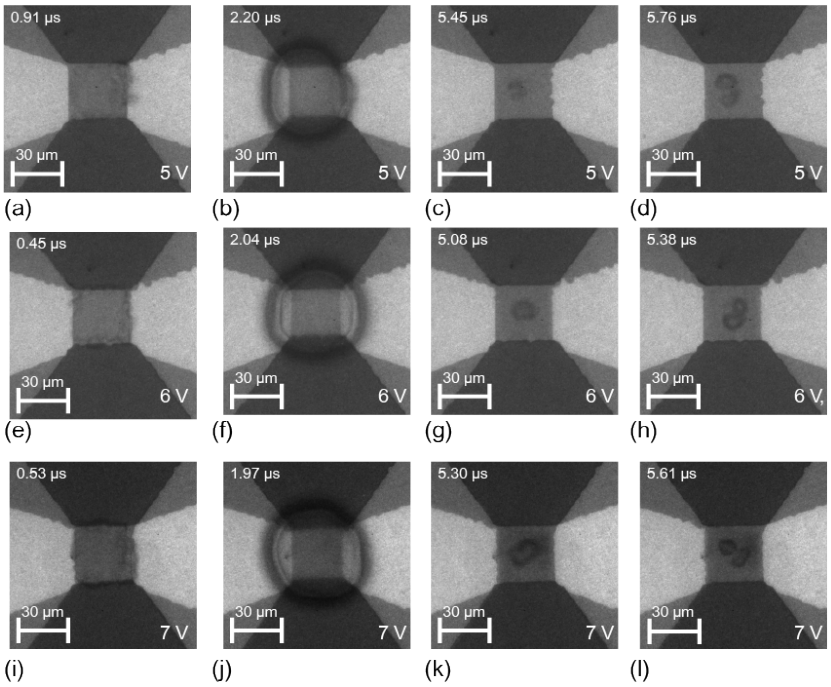

Figure 5.7: A series of images (captured using a high-speed camera) obtained during a resistor firing event during open-pool lifetime testing using a 3 μs @ 5V pulse when (a) homogeneous nucleation is initiated, (b) the bubble is at a maximum size, (c) the point of initial cavitation, and (d) the end of cavitation . A series of images of a resistor fired at 3 μs @ 6 V pulse width when (e) homogeneous nucleation is initiated, (f) the bubble is at a maximum size, (g) the point of initial cavitation, and (h) the end of cavitation. A series of images of a resistor fired at 3 μs @ 7 V pulse when (i) homogeneous nucleation is initiated, (j) the bubble is at a maximum size, (k) the point of initial cavitation, and (l) the end of cavitation.

lifetime test is not identical to that of testing a real TIJ device. Lifetime failure for a resistor in this open-pool test is defined as occurring when a resistor's resistance increases by 40%

The open-pool lifetime test utilizes unpassivated resistors. An unpassivated resistor puts the resistor in direct contact with the test fluid while voltage is applied to the resistor, thereby promoting an electrochemical reaction. This electrochemical reaction is not representative of a real TIJ device in which corrosive inks are used within a fluidic channel. 18 $M\Omega$ deionized water is used as the open-pool lifetime test fluid, thereby reducing but not eliminating the possibility of electrochemically induced degradation.

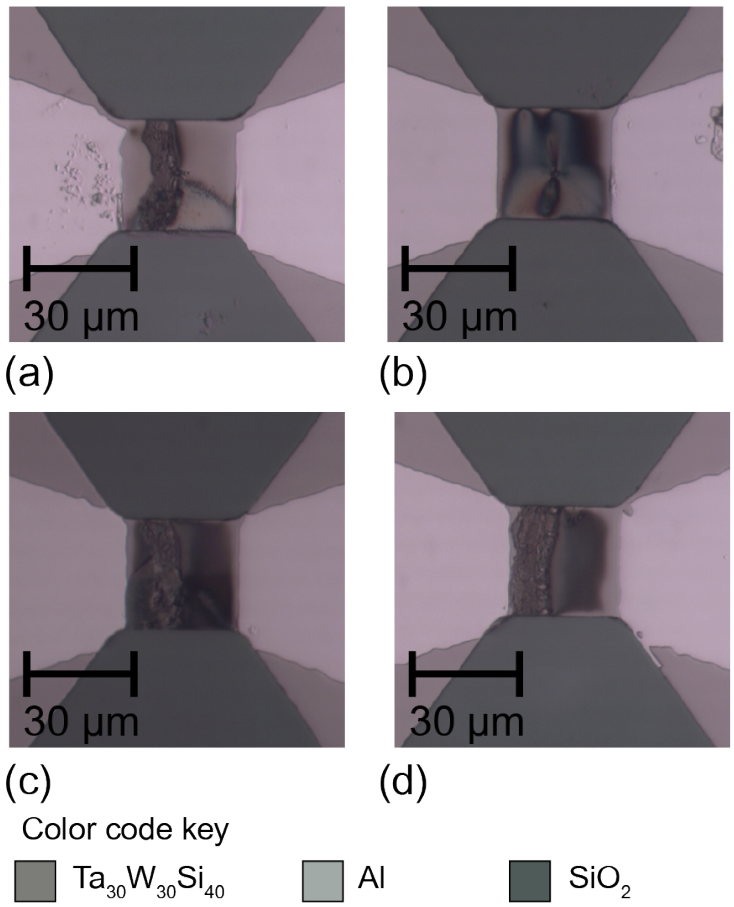

Figure 5.8: 50× optical images of a resistor fired until failure during open-pool lifetime testing using a 3 μs pulse width fired at an input voltage of (a) 5, (b) 6, (c) 6.5, and (d) 7 V.

Figure 5.7 displays a series of 60× optical images of a nucleation event using a 3 μs input pulse width and a 5 (a-d), 6 (e-h), or 7 V (i-l) input voltage. In each series, the bubble collapse and the concomitant cavitation damage occurs in the center of the resistor. Cavitation damage is expected to be observed near the center of the resistor. Typically, the eventual failure is initiated from this point for devices tested at 5 V and 6 V.

Figure 5.8 shows a series of 50× optical images of resistors after open-pool lifetime testing. All of the devices tested at 5 V and 6 V fail as a result of cavitation damage, as evidenced by the physical damage associated with creating a hole near the center of the

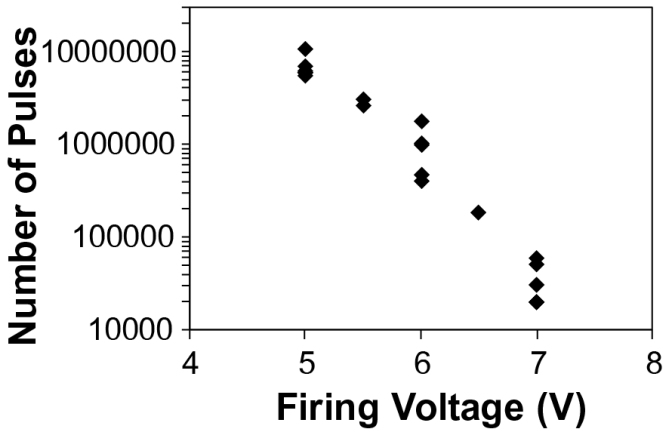

Figure 5.9: The number of pulses, or firing events, prior to failure (i.e., a 40% increase in resistance) versus the input voltage using a 3 μs input pulse width.

resistor. This damage essentially creates two parallel resistors, leading to changes in the heating dynamics, and thus resulting in a change in the location of the cavitation damage. This initial resistor damage spreads across the width of the resistor, leading to an open-circuit failure, as seen in Fig. 5.8 (a), (c), and (d). Figure 5.8 (b) iillustrates a failure that occurs after a 40% increase in resistance, but prior to an open-circuit failure. In this image, cavitation damage is observed near the center of the resistor and additional damage is seen forming below and above this point, i.e., the damage is beginning to spread across the width of the resistor.

As the input voltage increases, more oxidation is seen on the resistor surface, as evident from Fig. 5.8. Figure 5.8 (a) possesses a minimal change in surface color on the undamaged areas of the resistor. As the input voltage is increased to 6, 6.5, and then 7 V, the surface of the resistor changes to different shades of blue, as observed in Fig. 5.8 (b - d). This change in color is due to an increasing oxide thickness on the surface. This increased oxide may contribute to issues with the resistor overheating and decreased lifetime.

Figure 5.9 is a plot of the number of pulses sent to a resistor prior to failure versus the input voltage. The lifetime reaches over 10^7 pulses prior to failure when using a 3 μs @ 5 V input pulse. This long lifetime indicates that $Ta_{30}W_{30}Si_{40}$ is promising for TIJ applications. This lifetime is similar to other materials reported in the literature at similar power densities [50, 51, 53]. The test environment employed differs from that of a real TIJ device. As noted previously, the cavitation damage occurring in this open-pool lifetime testing experiment is believed to be more severe then that witnessed during typical TIJ resistor operation.

5.4 Material Stability Prior to Device Failure

The overall goal of the research discussed herein is to create an AMTF to be used as a TIJ cavitation plate and/or TIJ resistor with improved lifetime. It is believed that the AMTF should retain its amorphous microstructure during TIJ operation in order to achieve improved lifetime. In order to determine the stability of the amorphous structure, $Ta_{30}W_{30}Si_{40}$ TIJ resistors are tested to 60% of their expected lifetime at a given pulse width - voltage combination in the open-pool lifetime test environment. Using a set 3 μs @ 5 V, 6 V, or 7V input pulse, resistors are subjected to 4,000,000, 600,000, or 20,000 pulses, respectively. To evaluate the stability of the amorphous structure, optical microscopy and SEM are used to detect any signs of surface crystallization while TEM and CBED are used to characterize the atomic structure.

Figure 5.10 (a) and (b) are images of a resistor subjected to 4,000,000 pulses using a 3 μs @ 5 V input pulse in deionized water and in air, respectively. The resistor fired in deionized water has cavitation damage near the center of the resistor, as seen in Fig. 5.10 (a). The resistor fired in deionized water also possesses a non-uniform surface oxide and other

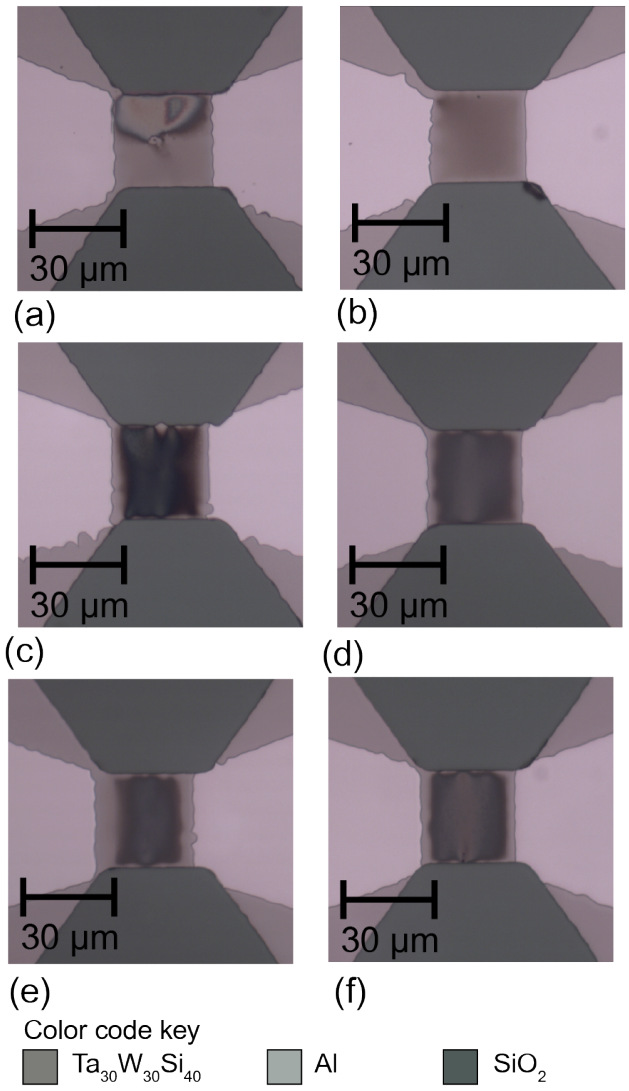

Figure 5.10: 50× optical images of a resistor fired to 60% of the resistor lifetime using a 3 μs @ 5 V input pulse in (a) deionized water and (b) air, 3 μs @ 6 V in (c) deionized water and (d) air, and 3 μs @ 7 V in (e) deionized water and (f) air.

surface features on the top half of the resistor. The features on the top half of the resistor are found to originate from Al, as shown later in the TEM analysis. The resistor fired in air has no signs of cavitation damage and a uniform surface oxide creating a slightly brown color on the resistor surface, as seen in Fig. 5.10 (b). Since the damage in the center of the resistor and

non-uniform features on the top half of the resistor are not present on the device fired in air, it confirms that these features are due to the water environment and not other thermal effects.

Figure 5.10 (c) and (d) are images of a resistor subjected to 600,000 pulses using a 3 μs @ 6 V input pulse in deionized water (c) and in air (d). Again, cavitation damage is seen near the center of the resistor tested in deionized water while the resistor tested in air displays no damage. Figure 5.10 (e) and (f) are images of a resistor subjected to 20,000 pulses using a 3 μs @ 7 V input pulse in deionized water (e) and in air (f). Both resistors in Fig. 5.10 (e) and (f) show no signs of cavitation damage. The lack of cavitation damage on the device tested using a 3 μs @ 7 V input pulse in deionized water is likely due to a significant decrease in the total number of pulses.

All of the resistors tested using a 6 and 7 V input voltage possess a significantly thicker surface oxide in comparison to those tested using a 5 V input voltage. The thicker oxide is characterized by the color of the resistor's surface changing to blue. The devices tested at higher voltage spend spend significantly less time at temperature. The thicker oxide on the 6 and 7 V resistors grows after being subjected to 600,000 and 20,000 pulses, respectively. Meanwhile the thinner oxide on the 5 V device is subjected to 4,000,000 pulses. This indicates the resistor's surface is reaching much higher temperature with the higher input voltage.

Figure 5.11 (a) presents an SEM image of the resistor tested using a 3 μs @ 5 V input pulse in deionized water at 5 $k\times$ and 20 $k\times$ magnification. The SEM image confirms that cavitation damage occurs near the center of the resistor. Figure 5.11 (b) shows an SEM image of the resistor tested using a 3 μs @ 6 V input pulse in deionized water at 5 $k\times$ and 20 $k\times$ magnification. Again, cavitation damage is found near the center of the resistor. The difference in cavitation damage between the resistor tested using a 6 V input pulse in comparison

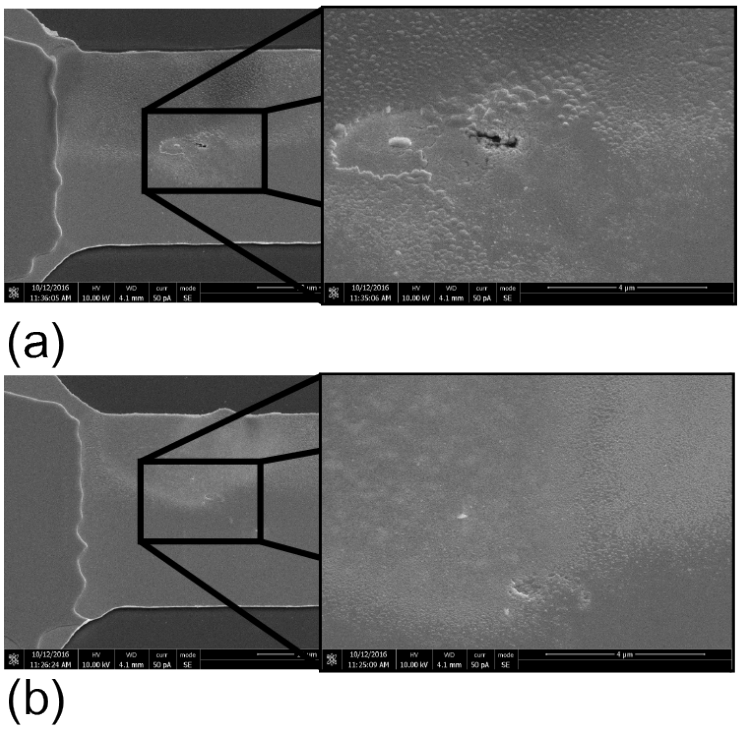

Figure 5.11: SEM images of a resistor and 20 $k\times$ magnification of the cavitation damage after operating to $\sim$60% of the resistor lifetime in deionized water using a 3 μs @ (a) 5 and (b) 6 V.

to that of the resistor tested using a 5 V input pulse is likely due to the difference in the total number of pulses, i.e., 4,000,000 compared to 600,000. The 6 V device underwent a fewer total number of pulses and possesses less severe cavitation damage, as seen in Fig. 5.11. The non-uniform Al surface features appear on the resistors tested at 5 V and 6 V. These features are less predominant on the resistor tested at 6 V in comparison to that of the resistor tested at 5 V, again, likely due to fewer number of test pulses, i.e., 4,000,000 compared to 600,000.

Figure 5.12 summarizes TEM analysis of a resistor subjected to 4,000,000 pulses using a 3 μs @ 5 V input pulse. Figure 5.12 (a) is a 81 $k\times$ TEM image of the entire thin film resistor, the surface oxide that develops during the open-pool test to 60% lifetime, and Al surface features also observed in optical and SEM analysis. In Fig. 5.12 (a), the AMTF resistor

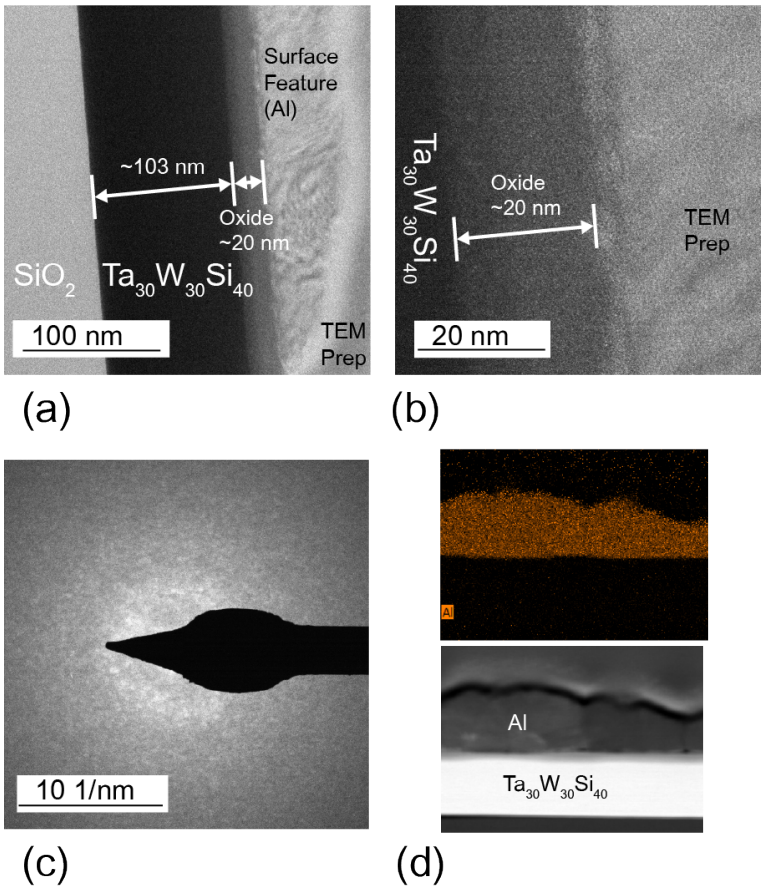

Figure 5.12: (a) TEM cross-section of a resistor after testing to 4,000,000 pulses in deionized water using a 3 μs @ 5 V input pulse. (b) Higher magnification TEM image of the amorphous metal and surface oxide. (c) CBED pattern of the amorphous metal showing that the film remains amorphous with broad scattering and no evidence of crystallinity. (d) STEM image of the resistor and Al feature on top of the resistor with EDS Al map confirming the feature composition.

remains unmodified, other than the development of the surface oxide. Scanning-tunneling electron microscopy (STEM) and energy dispersive spectroscopy (EDS) analysis revealed that the surface features are composed of aluminum and aluminum oxide, as seen in Fig. 5.12 (d). Al migration occurs during the 4,000,000 test pulses applied in the deionized water environment. Al-Cu traces are routed from the top of the device, which likely contributes to

the non-uniform distribution of Al on the top portion of the resistor, as seen in Fig. 5.11. In a real TIJ device, these features do not occur since the traces are passivated.

Figure 5.12 (b) is a 360 $k\times$magnification TEM image of the interface between the amorphous metal resistor and the oxide that forms on the metal surface. A 20 nm oxide forms on the surface of the amorphous metal. The higher magnification TEM image shows an abrupt transition between the oxide and the AMTF, similar to the results reported in Sect. 4.4. In the high magnification TEM image, no crystallinity is observed and the dense AMTF remains unchanged.

Figure 5.12 (c) is a CBED pattern of the amorphous metal thin film and surface oxide. The CBED pattern possesses broad scattering, indicative of an amorphous metal and possesses no polycrystalline features. This confirms that the AMTF remains amorphous after open-pool testing to 60% of the lifetime.

Figure 5.13 summarizes TEM analysis of a resistor subjected to 20,000 pulses using a 3 μs @ 7 V input pulse. Figure 5.13 (a) is a 81 $k\times$ magnification TEM image of the entire thin film and the surface oxide that develops during testing. After testing to 20,000 pulses, 77 nm of the 110 nm as-deposited thin film remains unmodified. The other 40 nm is consumed in the oxidation process in order to grow the 74 nm surface oxide. Figure 5.13 (b) is a 410 $k\times$ magnification TEM image of the interface between the amorphous metal and oxide that forms on the metal surface, as seen in Fig. 5.13 (a). There is an abrupt transition between the metal and oxide, as expected. The amorphous metal does not possess any crystalline features, while crystalline grains are seen in portions of the oxide.

Figure 5.13 (c) and (d) are CBED patterns of the $Ta_{30}W_{30}Si_{40}$ AMTF and surface oxide, respectively. The CBED pattern from the amorphous metal film possesses broad scatter-

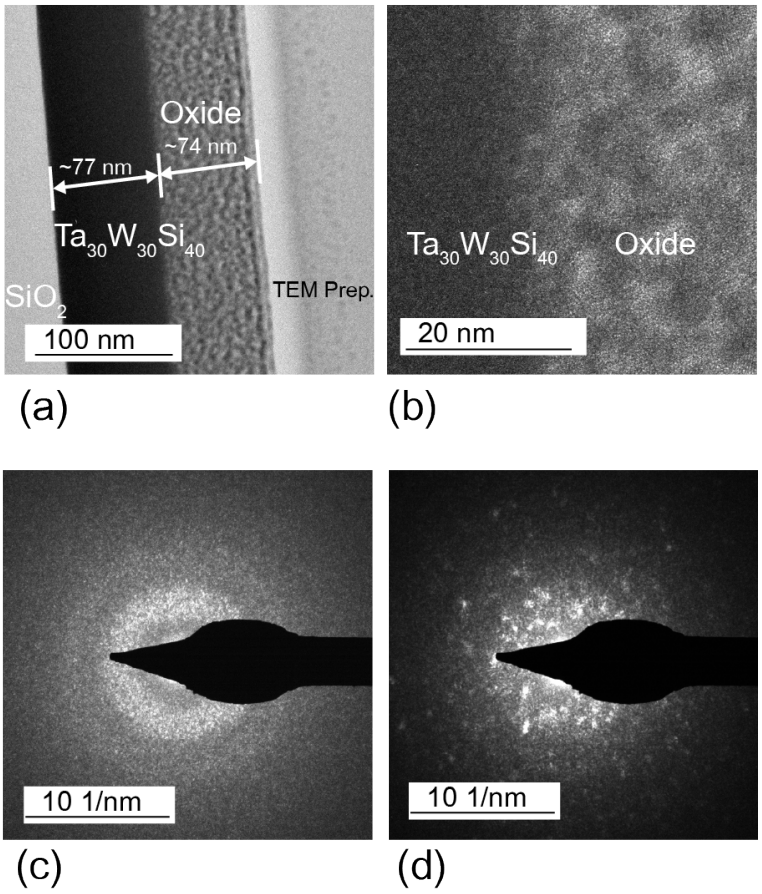

Figure 5.13: (a) TEM cross-section of a resistor after 20,000 pulses in deionized water using a 3 μs @ 7 V input pulse. (b) Higher magnification TEM image of the amorphous metal and surface oxide. (c) CBED pattern of the amorphous metal showing the film remains mostly amorphous after testing. (d) CBED pattern of the oxidized amorphous metal showing a polycrystalline structure in the oxide.

ing that is indicative of an amorphous metal, as seen in Fig. 5.13 (c). The oxide CBED pattern possesses bright points which are indicative of a polycrystalline film, as seen in Fig. 5.13 (d). This confirms that the amorphous metal remains amorphous after open-pool testing to 60% of the lifetime, as desired.

5.5 Summary

Patterned $Ta_{30}W_{30}Si_{40}$ TIJ resistor electrical properties are found to match those of the blanket film. Nucleation and lifetime testing found the $Ta_{30}W_{30}Si_{40}$ resistor nucleates as expected and is mechanically stable with respect to the expected TIJ environment. $Ta_{30}W_{30}Si_{40}$ TIJ resistors retain their amorphous microstructure after open-pool testing to 60% of their lifetime. Thus, $Ta_{30}W_{30}Si_{40}$ amorphous metal is a good candidate for use as a TIJ cavitation plate and/or TIJ resistor.

6. UNDERSTANDING MIM DIODE ELECTRICAL CHARACTERISTICS USING VARIOUS AMTF ELECTRODES

This chapter presents results of metal-insulator-metal (MIM) diode electrical studies. First, results from MIM diodes fabricated using a ZrCuAlNi bottom contact are presented and modeled. The Al-Al_2O_3-ZrCuAlNi MIM diode is a previously characterized reference system shown to display Fowler-Nordheim conduction [19, 20, 134]. Next, electrical characterization of MIM diodes fabricated using the new AMTFs developed for this research are presented. Finally, a discussion linking the effects of different bottom electrodes to existing models is presented.

6.1 Modeling ZrCuAlNi MIM Tunneling Diodes

Figure 6.1 (a) plots curves of $\ln(I/V^2)$ versus 1/V (a Fowler-Nordheim plot) for an Al-Al_2O_3-ZrCuAlNi MIM diode. $R^2>0.999$ indicates a strong correlation Fowler-Nordheim tunneling. This is in agreement with previous results found in literature [19, 20, 134].

Figure 6.1 (b) shows logarithm of current versus the applied voltage (log(I)-V) curves from the same Al-Al_2O_3-ZrCuAlNi diode, with simulated curves as dashed red lines. Simulations use the equation and model parameters found in Table 6.1. Injection from the Al-Al_2O_3 interface (negative polarity) yields a good simulation fit to the measured data, with curves overlapping for over an order of magnitude. Injection from the ZrCuAlNi-Al_2O_3 interface (positive polarity) results in a much poorer fit to the measured data. Thus, electron injection from the ZrCuAlNi-Al_2O_3 interface yields a poor fit to the Fowler-Nordheim equation while injection from the Al-Al_2O_3 interface provides an excellent fit.

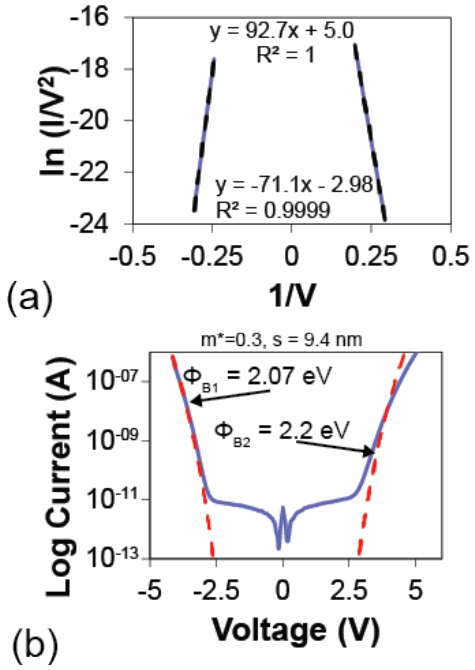

Figure 6.1: (a) $\ln(I/V^2)$ versus 1/V Fowler-Nordhiem plots with trendlines (black dashed line) for a Al-Al_2O_3-ZrCuAlNi MIM diode. (b) log(I)-V plot for a Al-Al_2O_3-ZrCuAlNi MIM diode with simulated curves shown as dashed red lines.

Figure 6.2 (a) is a TEM image of a Al-Al_2O_3-ZrCuAlNi MIM diode from Cowell *et al.* [19]. The Al-Al_2O_3 interface, between M1 and I, is abrupt with a clear demarcation between Al and Al_2O_3. This conforms to that expected for Fowler-Nordheim tunneling. In contrast, the ZrCuAlNi-Al_2O_3 interface, between I and M2, possesses a 1.6 nm thick native oxide at the interface. This native oxide forms either prior to or during Al_2O_3 insulator deposition. Figure 6.2 (b) is an energy band diagram corresponding to the TEM image. The Al-Al_2O_3 interface in the energy band diagram is abrupt while the ZrCuAlNi-Al_2O_3 interface possesses an interfacial native oxide. ZrCuAlNi oxidation studies suggest that the surface native oxide is dominated by Zr and Al oxides [136], but the electrical quality of this oxide is not known. The presence of a native oxide is not accounted for in the boundary conditions used to formulate the Fowler-Nordheim equation. Thus, the presence of an interfacial native

Table 6.1: Equations, simulation parameters, and linearized equations used for analyzing MIM diodes.

Simulated Equation [135]			
$J = \frac{C_1 \xi^2}{\phi_B m^*} \exp\left(\frac{-C_2 \phi_B^{\frac{3}{2}} \sqrt{m^*}}{\xi}\right)$			
Injecting Interface	ϕ_B	$\mathbf{m^*}$	**s**
	$[eV]$	$[unitless]$	$[nm]$
Al-Al_2O_3	2.07	0.3	9.4
ZrCuAlNi-Al_2O_3	2.2	0.3	9.4
Linearized Equation [105]			
$ln\frac{J}{\xi^2} = \left(-C_2 \phi_{ox}^{\frac{3}{2}} \sqrt{m^*}\right) \frac{1}{\xi} + ln\left(\frac{C_1}{\phi_{ox} m^*}\right)$			
Slope		$-C_2 \phi_{ox}^{\frac{3}{2}} \sqrt{m^*}$	
Intercept		$ln\left(\frac{C_1}{\phi_{ox} m^*}\right)$	
Simmons Equation [103, 110]			
$J = \frac{s^2 \times C_1 (V+\Delta\phi)^2}{\phi_B m^*} \exp\left(\frac{s \times -C_2 \phi_B^{\frac{3}{2}} \sqrt{m^*}}{V+\Delta\phi}\right)$			
$\Delta\phi = \Phi_{M1} - \Phi_{M2}$			

oxide is a likely reason why simulations of electron injection from the ZrCuAlNi-Al_2O_3 interface using the Fowler-Nordheim equation yield a poor fit to the experimental data. Due to these native oxide artifacts, only the negative polarity curves corresponding to electron injection from the Al-Al_2O_3 interface are considered in the subsequent analysis of MIM diode electrical characteristics.

A simulation of ϕ_B as a function of m^* is shown in Figure 6.3 in order to further underscore problems associated with interpreting I-V data involving electron injection from the ZCAN-Al_2O_3 interface. The slope and intercept equations found in Table 6.1 are used to generate the ϕ_B-m^* plots shown in Fig. 6.3. Figure 6.3 (a) shows ϕ_B-m^* plots corresponding to

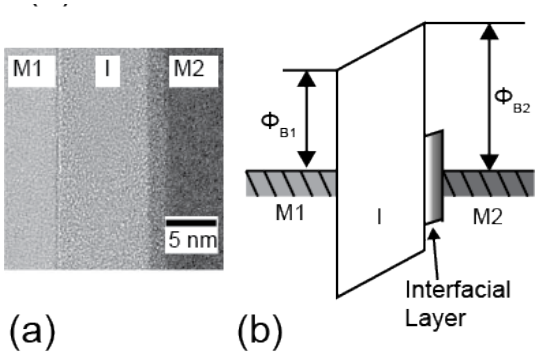

Figure 6.2: (a) TEM image of a Al-Al_2O_3-ZrCuAlNi MIM diode from Cowell *et al.* showing an abrupt Al-Al_2O_3 interface between M1 and I and the existence of a native oxide between M2 and I. (b) An equilibrium energy band diagram of the MIM diode with an interfacial oxide between the M2 and I.

electron injection from the Al-Al_2O_3 interface. The slope estimates of ϕ_B are within the range for the Al-Al_2O_3 interface, while the intercept estimates of ϕ_B are physically unrealistic by a factor of $\sim$10. Other authors have noted a similar trend in which with the intercept estimate is unreliable for predicting ϕ_B [137]. Similarly, Fig. 6.3 (b) shows ϕ_B-m^* plots corresponding to electron injection from the ZrCuAlNi-Al_2O_3 interface. Again, the slope estimates of ϕ_B are reasonable, while the intercept estimates of ϕ_B are off by over four orders of magnitude. This intercept estimator error is further support that electron injection from an interface possessing a native oxide is not adequately described by the Fowler-Nordhiem equation.

6.2 MIM Diodes Using Various AMTF Bottom Electrodes

Figure 6.4 shows log(I)-V curves corresponding to electron injection from the Al–Al_2O_3 interface for MIM diodes fabricated using $Pt_{50}Ta_{20}Si_{30}$, $Ta_{40}Ni_{40}Si_{20}$, $Ta_{40}W_{40}Si_{20}$, ZrCuAlNi, and $Ta_{40}Hf_{40}Si_{20}$ bottom electrodes. The Al-Al_2O_3 barrier is expected to be the same for of these all devices, but in fact, but the curves in Fig. 6.4 do not overlap. This

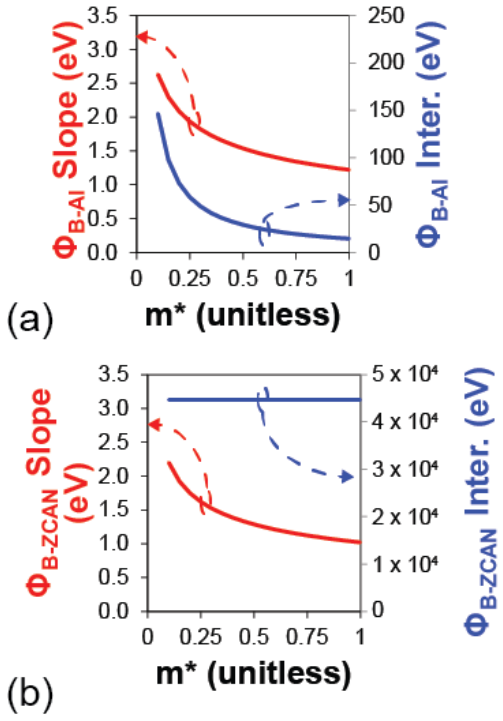

Figure 6.3: Simulations of $\Phi_{B-Al-Al_2O_3}$ versus m^* as obtained from the linearized slope and intercept equations given in Table 6.1 for (a) electron injection from the Al-Al_2O_3 interface and (b) electron injection from the ZrCuAlNi-Al_2O_3 interface.

variation in log(I)-V curves indicates that the bottom electrode has a significant impact on the electrical characteristics corresponding to electron injection from the top interface.

Figure 6.5 (a) shows Fowler-Nordheim plots for each of the curves from Fig. 6.4. The range of data used for the fit is shown by the dashed black lines in Fig. 6.4. R^2 near 1 demonstrates the applicability of Fowler-Nordheim tunneling. Figure 6.5 (b) shows the current density at an applied voltage of 3.7 V versus the test temperature. As shown in Fig. 6.5 (b), there is a minimal change in current density over the temperature range of 50 °C, demonstrating that the device current is relatively temperature independent. This is further evidence for tunneling.

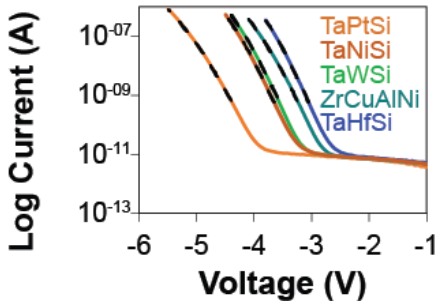

Figure 6.4: log(I) versus V curves for MIM diodes fabricated using $Pt_{50}Ta_{20}Si_{30}$, $Ta_{40}Ni_{40}Si_{20}$ $Ta_{40}W_{40}Si_{20}$, ZrCuAlNi, or $Ta_{40}Hf_{40}Si_{20}$ bottom electrodes. Dashed lines indicate the portion of the measured data used to generate Fowler-Nordheim plots. Only negative log(I)-V curves are shown, corresponding to electron injection from the Al-Al_2O_3 interface.

Table 6.2 lists the bottom contact material, slope and intercept from the Fowler-Nordheim plot, and Al-Al_2O_3 barrier ($\phi_{B-Al-Al_2O_3}$) estimated from the Fowler-Nordheim plot slope (assuming m^* = 0.3). Even though the Al-Al_2O_3 barrier is expected to be the same, the Fowler-Nordheim slopes and intercepts differ. There is a difference of $\sim$0.75 eV in the estimated $\phi_{B-Al-Al_2O_3}$ when using Fowler-Nordheim slopes from MIM diodes with different bottom electrodes. This inconsistency in parameters indicates that the Fowler-Nordheim equation as formulated cannot adequately explain the measured data associated with MIM diodes having different bottom electrodes.

Figure 6.6 (a) is an equilibrium energy band diagram showing the impact of dissimilar electrode work functions, as previously considered by Simmons and discussed in Section 2.11. This difference in electrode work functions is accounted for by a $\Delta\phi$ term in the Simmons equations shown at the bottom of Table 6.1. $\Delta\phi$ is a built-in potential which modifies the applied voltage required to reach the onset of Fowler-Nordheim tunneling compared to what it would in the ideal flat band case in which $\Delta\phi = 0$. This is illustrated in Fig. 6.6 (b). $\Delta\phi$ gives rise to a lateral shift to an I-V curve along the voltage axis.

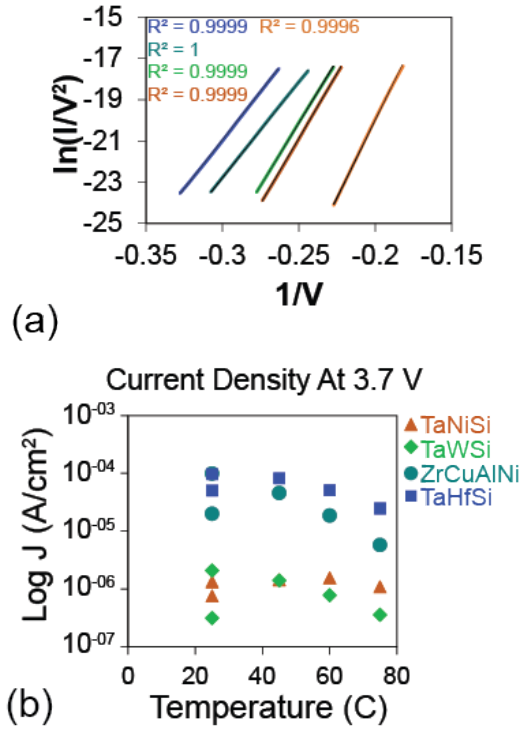

Figure 6.5: (a) $\ln(I/V^2)$ versus 1/V Fowler-Nordheim plots for Al-Al_2O_3-AMTF MIM diodes. (b) Current density at 3.7 V versus test temperature for Al-Al_2O_3-AMTF MIM diodes. AMTF = $Pt_{50}Ta_{20}Si_{30}$, $Ta_{40}Ni_{40}Si_{20}$ $Ta_{40}W_{40}Si_{20}$, ZrCuAlNi, and $Ta_{40}Hf_{40}Si_{20}$ bottom electrodes.

Figure 6.7 (a) shows two cases in which measured curves are adjusted using two different strategies for evaluating $\Delta\phi$. In Fig. 6.7, the left set of curves are obtained by choosing $\Delta\phi$ so that each curve overlaps the $Pt_{50}Ta_{20}Si_{30}$ measured curve. This is equivalent to assuming that $\Delta\phi = 0$ for the $Pt_{50}Ta_{20}Si_{30}$ curve (see Table 6.3). Alternatively, the right set of curves are obtained by choosing $\Delta\phi$ so that all of the curves align to the $Ta_{40}Hf_{40}Si_{20}$ measured curve (see Table 6.4).. After performing these $\Delta\phi$ corrections, the Fowler-Nordheim plots also overlap, as seen in Fig. 6.7 (b). Thus, accounting for the built-in potential associated with $\Delta\phi$ provides a correction to the measured I-V characteristics when injecting electrons from the Al-Al_2O_3 interface that accounts for the effects of varying the bottom electrode.

Table 6.2: Al-Al_2O_3-AMTF MIM diode bottom electrode, extracted slope and intercept from Fig 6.5, and estimated barrier $\phi_{B-Al-Al_2O_3}$. $\phi_{B-Al-Al_2O_3}$ barrier estimates are obtained from the slope value assuming an effective mass of 0.3 and insulator thickness of 9.4 nm.

Bottom Electrode	**Slope**	**Intercept**	$\phi_{B-Al-Al_2O_3}$ **Barrier Estimate** [eV]
$Ta_{40}Hf_{40}Si_{20}$	93.90	7.20	1.9
ZrCuAlNi	92.45	4.97	1.9
$Ta_{40}W_{40}Si_{20}$	120.84	10.1	2.27
$Ta_{40}Ni_{40}Si_{20}$	126.19	10.6	2.26
$Pt_{50}Ta_{20}Si_{30}$	149.42	9.9	2.63

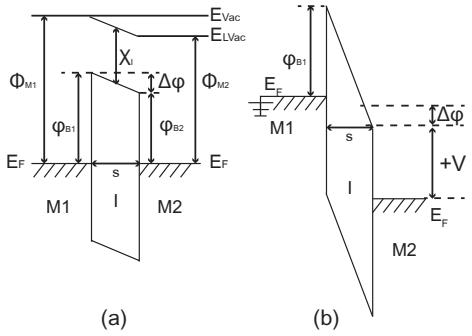

Figure 6.6: (a) An equilibrium energy band diagram for an asymmetric diode. The metal work function of the left electrode (M1) is greater than the metal work function of the right electrode (M2). (b) Non-equilibrium energy band diagram with a large positive bias applied to electrode M2 and M1 is at ground.

Tables 6.3 and 6.4 summarize $\Delta\phi$ correction trends when the I-V curves are aligned to the $Pt_{50}Ta_{20}Si_{30}$ or $Ta_{40}Hf_{40}Si_{20}$ measured curves, respectively. The first key take-away from a comparison of Tables 6.3 and 6.4 is that the work function trend of Table 6.4 is more reasonable than that of Table 6.3 since, for instance, the expected work function of Pt is 5.4 eV [138]. Although the $\Delta\phi$ correction procedure is capable of aligning measured I-V curves in a more physically satisfying manner, there does not appear to be any obvious strategy for uniquely determining which particular curve to use as a reference in which $\Delta\phi =$

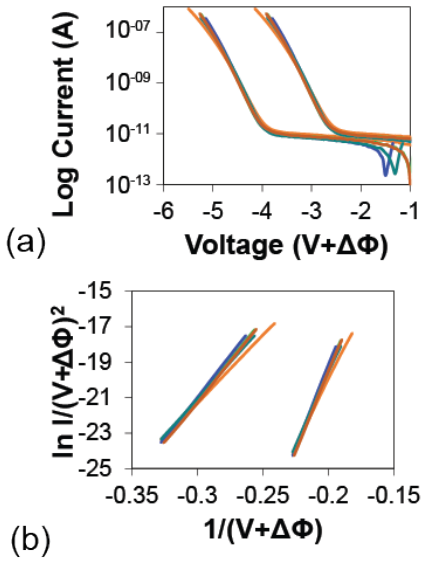

Figure 6.7: (a) log(I)-(V+$\Delta\phi$) plot corresponding to electron injection from the Al-Al_2O_3 interface for MIM diodes with an Al-Al_2O_3-AMTF stack. The AMTF bottom electrode is $Pt_{50}Ta_{20}Si_{30}$, $Ta_{40}Ni_{40}Si_{20}$, $Ta_{40}W_{40}Si_{20}$, ZrCuAlNi, or $Ta_{40}Hf_{40}Si_{20}$. $\Delta\phi$ adjusts measured currents to overlap with the $Pt_{50}Ta_{20}Si_{30}$ (left) or with the $Ta_{40}Hf_{40}Si_{20}$ (right) sweeps. (b) $\ln(I/(V+\Delta\phi))^2)$ versus $1/(V+\Delta\phi)$) Fowler-Nordheim linearization, confirming that the $\Delta\phi$ correction indeed aligns the curves.

0. The second key take-away from Tables 6.3 and 6.4 is that by including $\Delta\phi$ the variation in $\phi_{B-Al-Al_2O_3}$ as estimated from the Fowler-Nordheim slope is reduced by almost half of the original variation. Although the work function trends of Table 6.3 appear to be more reasonable then those of Table 6.4, the barrier estimates of Table 6.4 (2.62-3.05 eV) are closer to those reported in the literature (2.8-3 eV [139]) than those of Table 6.3 (1.68-1.92eV). Other researchers have previously reported that the slope of a Fowler-Nordheim plot provides a lower barrier estimate compared to those obtained from photoemission measurement [135].

6.3 Conclusions

$Pt_{50}Ta_{20}Si_{30}$, $Ta_{40}Ni_{40}Si_{20}$, $Ta_{40}W_{40}Si_{20}$, ZrCuAlNi, or $Ta_{40}Hf_{40}Si_{20}$ amorphous metals are used as bottom electrodes in MIM diodes in order to demonstrate the impact of the

Table 6.3: Al-Al_2O_3-AMTF MIM diode bottom electrode, $\Delta\phi$, bottom electrode estimated work function (WF), extracted slope and intercept from Fig 6.5, and estimated barrier when aligned to $Pt_{50}Ta_{20}Si_{30}$ curve. $\phi_{B-Al-Al_2O_3}$ barrier estimates are obtained from the slope value assuming an effective mass of 0.3 and insulator thickness of 9.4 nm.

Bottom Electrode	$\Delta\phi$ $[eV]$	WF $[eV]$	**Slope**	**Intercept**	$\phi_{B-Al-Al_2O_3}$ **Barrier Estimate** $[eV]$
$Ta_{40}Hf_{40}Si_{20}$	-1.35	2.85	187.1	11.7	3.05
ZrCuAlNi	-1.15	3.05	163.1	13.0	2.78
$Ta_{40}W_{40}Si_{20}$	-0.85	3.35	180.1	16.6	2.97
$Ta_{40}Ni_{40}Si_{20}$	-0.77	3.43	180.6	16.6	2.97
$Pt_{50}Ta_{20}Si_{30}$	0	4.2	149.4	9.9	2.62

Table 6.4: Al-Al_2O_3-AMTF MIM diode bottom electrode, $\Delta\phi$, bottom electrode estimated work function (WF), extracted slope and intercept from Fig 6.5, and estimated barrier when aligned to $Ta_{40}Hf_{40}Si_{20}$ curve. $\phi_{B-Al-Al_2O_3}$ barrier estimates are obtained from the slope value assuming an effective mass of 0.3 and insulator thickness of 9.4 nm.

Bottom Electrode	$\Delta\phi$ $[eV]$	WF $[eV]$	**Slope**	**Intercept**	$\phi_{B-Al-Al_2O_3}$ **Barrier Estimate** $[eV]$
$Ta_{40}Hf_{40}Si_{20}$	0	4.2	93.90	7.20	1.92
ZrCuAlNi	0.2	4.4	82.2	3.58	1.76
$Ta_{40}W_{40}Si_{20}$	0.5	4.7	91.4	6.27	1.89
$Ta_{40}Ni_{40}Si_{20}$	0.58	4.78	91.5	6.2	1.89
$Pt_{50}Ta_{20}Si_{30}$	1.35	5.55	76.4	1.62	1.68

bottom electrode on I-V characteristics. Measured I-V curves from these devices show that the onset of current conduction for electron injection at the Al-Al_2O_3 is shifted along the voltage axis based on the nature of the bottom electrode. This shift is due to the built-in potential established by the difference in work functions of the top and bottom contacts. By employing the $\Delta\phi$ correction, as devised by Simmons, negative polarity measured I-V char-

acteristics which are displaced from one another along the voltage axis due to differences in their bottom electrode may be corrected so that these curves overlap, as expected. However, this $\Delta\phi$ correction procedure does not provide a procedure for determining a unique, physically relevant estimate of the true $\Delta\phi = 0$ flat band reference.

7. CONCLUSIONS AND RECOMMENDATION FOR FUTURE WORK

7.1 Conclusions

The goal of the research project culminating in this dissertation was to develop a thermally stable amorphous metal thin film (AMTF) for TIJ and MIM tunnel diode applications. This goal was achieved. AMTFs were developed using the following guidelines, as developed from the literature.

- The amorphous metal should be composed of three or more elements with the major element being a refractory metal.
- The constituent elements should have a wide distribution of atomic radii, with at least a 12% difference in size between any two elements.
- There should be a large negative heat of mixing among each of the components.
- At least one of the components should be a metalloid, such as Si.

Based on the above the design criteria, six AMTFs with crystallization temperatures of greater than 600 °C were deposited using multicomponent sputter targets and characterized to be amorphous and thermally stable. The sputtering target composition of these AMTFs, with their respective crystallization temperatures, are shown in Table 7.1. The crystallization temperatures of AMTFs metals demonstrate the fundamental viability of the design rules employed, i.e. the more refractory the composition, the higher the thermal stability and incorporation of a metalloid is crucial for achieving the highest crystallization temperature. The oxidation of $Ta_{40}W_{40}Si_{20}$ and $Ta_{30}W_{30}Si_{40}$ is studied. It is found that these AMTFs

Table 7.1: Amorphous metal thin films (AMTFs) developed in this dissertation and their corresponding crystallization temperature.

AMTF	**Crystallization Temperature** $[^{\circ}C]$
$Ta_{40}Ni_{40}Si_{20}$	600 - 700
$Ta_{40}Hf_{40}Si_{20}$	600 - 700
$Ta_{40}Mo_{40}Si_{20}$	800 - 900
$Ta_{30}W_{50}Si_{20}$	800 - 900
$Ta_{40}W_{40}Si_{20}$	900 - 1000
$Ta_{30}W_{30}Si_{40}$	1000 - 1100

form a stable passive oxide and that the transition between the AMTF and the native oxide is remarkably abrupt. These AMTFs display much better oxidation stability compared to that of a β-Ta thin film, the metal typically used for TIJ applications.

A $Ta_{30}W_{30}Si_{40}$ AMTF possesses a crystallization temperatures up to well in excess of the basic TIJ requirement, i.e., $>$ 340 °C, and is shown to be capable of withstanding the demanding TIJ environment. It is also shown to be mechanically stable and to retain its amorphous microstructure after testing to 60% of its lifetime, making it a promising candidate for TIJ applications.

$Pt_{50}Ta_{20}Si_{30}$, $Ta_{40}Ni_{40}Si_{20}$, $Ta_{40}W_{40}Si_{20}$, ZrCuAlNi, or $Ta_{40}Hf_{40}Si_{20}$ AMTFs are used as bottom electrodes in MIM diodes in order to demonstrate the impact of the bottom electrode on measured I-V characteristics. While the nature of electron injection at the Al-Al_2O_3 should not depend on the bottom AMTF electrode, measured I-V curves from devices fabricated suing these AMTFs as bottom electrodes show that the onset of current conduction is shifted along the voltage axis. This shift is ascribed to the built-in potential established by

the difference in work function of Al top contact and the AMTF bottom contact. Although a $\Delta\phi$ correction procedure can be used to align measured I-V curves obtained using different AMTF bottom electrodes, this $\Delta\phi$ correction procedure does not yield a unique, physically satisfying estimate for the $\Delta\phi = 0$ reference.

7.2 Future Work

While the goal of this thesis has been met, there are still many directions that could be pursued to further expand the field of AMTFs and MIM tunnel diodes.

Oxidation Studies

Further oxidation studies should be performed on all of the materials developed from this work. Additional characterization of $Ta_{30}W_{30}Si_{40}$ would enable the development of oxidation rate equations. Further studies of the other systems not discussed herein, e.g., $Ta_{40}Ni_{40}Si_{20}$, $Ta_{40}Mo_{40}Si_{20}$, and $Ta_{40}Hf_{40}Si_{20}$, may show improved oxidation stability at lower temperatures. For example, $Ta_{40}Ni_{40}Si_{20}$ may possess much less oxidation at temperatures below 600 °C. Additionally, studies of other materials may reveal different oxidation mechanisms leading to new applications. For example, oxidization of $Ta_{40}Hf_{40}Si_{20}$ may lead to a new type of insulator.

Thermal Inkjet Printer Product Testing and Applications

$Ta_{30}W_{30}Si_{40}$ AMTFs should be tested in a TIJ product as a cavitaiton plate and as a resistor material. Product testing would appropriately evaluate the improvements an amorphous metal would provide as a TIJ cavitation plate. Additionally, strategies for increasing the resistivity of the AMTF should be explored.

AMTFs MIM Diode Characterization

Further studies of these AMTFs as MIM diode bottom electrodes are needed to address the uniqueness of ϕ_B and $\Delta\phi$. $\Delta\phi$ estimates that provide satisfying estimates of the bottom electrode work function do not provide satisfying estimates of ϕ_B in comparison to that of an internal photoemission measurement (IPE). There is currently no satisfying theory to explain this trend and additional studies, such as low temperature measurements, may lead to the development of an explanation.

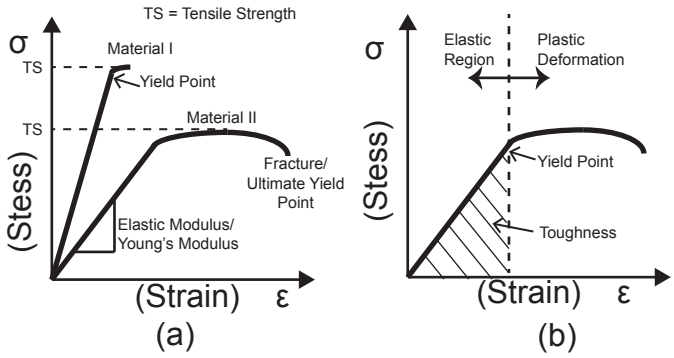

Figure 8.1: Idealized stress-strain curves from an uniaxial tensile test defining mechanical properties such as (a) yield point, elastic modulus, tensile strength (TS), fracture point, (b) toughness, elastic region, and plastic deformation region.

8. APPENDIX

8.1 A Review of Mechanical Properties

A review of common mechanical testing terminology is provided to facilitate a subsequent discussion of amorphous metal mechanical properties. Stress-strain curves, shown in Fig. 8.1, are essential for assessing the mechanical properties of solids. The slope of the linear portion of the stress-strain curve (Fig. 8.1 (a)) is equal to the elastic modulus, or Young's modulus [79]. More precisely, Young's modulus is a measure of the rate of change in strain under an applied uniaxial stress in the linear portion of the stress-strain curve or elastic region (the elastic is region shown in Fig. 8.1 (b)) [79]. Young's modulus applies to elastic strain, i.e., strain that disappears after the stress is removed. The bulk modulus is another measure of elasticity, involving a change in volume due to uniform compression rather than uniaxial stress. The yield point, shown in Fig. 8.1 (a) and (b), is the largest stress a material can handle prior to the onset of a permanent change in strain, beyond which the material does not return

to its original shape [79]. The yield point defines the upper limit of elastic behavior. Past the yield point of a stress-strain curve, the material undergoes plastic deformation, as indicated in Fig. 8.1 (b) [79]. Under these conditions, the material is permanently deformed. The tensile strength, shown in Fig. 8.1 (a), is the largest stress the material can withstand. Material I in Fig. 8.1 (a) is characteristic of a brittle material which exhibits little or no plastic deformation prior to fracture (defined by the fracture point). Material II in Fig. 8.1 (a) is characteristic of a ductile material exhibiting a significant amount of plastic deformation prior to fracture. Crystalline metals tend to be ductile [79]. Toughness is the area under the stress strain curve in the elastic region, as shown in Fig. 8.1 (b) It is a measure of how much energy a material can accommodate within the elastic region [79].

Hardness is another common mechanical property. It is often defined as ”resistance to the formation of a permanent surface impression by an indenter” [79]. In an indention test, a sharp tip is driven into the test sample to determine a hardness value. Vickers hardness is a specific hardness test that is commonly used to assess a material's hardness. The resulting measurement from this test is known as the Vickers hardness.

8.2 XRD Phase Matches for TaWSi Thermal Analysis

Phase analysis for the $Ta_xW_ySi_z$ crystallization study is presented in Figs. 8.2, 8.3, and 8.4. Since $Ta_xW_ySi_z$ possesses the high highest thermal stability, this phase analysis is presented for completeness. This information may also be useful in further understanding the performance and behavior of this material system.

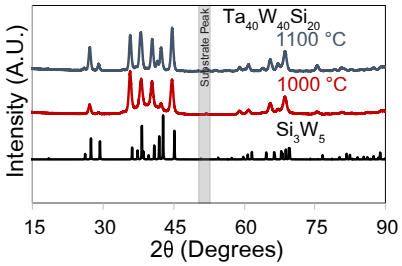

Figure 8.2: Crystalline pattern of Si_3W_5 (ICSD : 733331 [10]) compared to that of $Ta_{40}W_{40}Si_{20}$ thin films crystallized at 1000 °C and 1100 °C. The silicon substrate peak artifact at ∼52.5° is indicated.

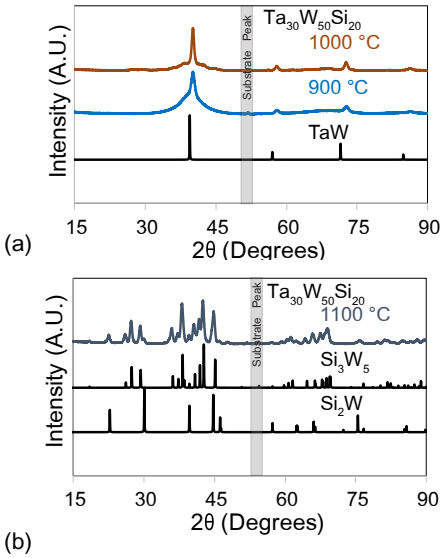

Figure 8.3: (a) Crystalline pattern of (i) TaW (ICSD 106122 [11]) compared to that of $Ta_{30}W_{50}Si_{20}$ thin films crystallized at 900 °C and 1000 °C. (b) Crystalline pattern of Si_3W_5 (ICSD 733331 [10]) and Si_2W (ICSD 96024 [12]) compared to that of a $Ta_{30}W_{50}Si_{20}$ thin film crystallized at 1100 °C. The silicon substrate peak artifact at ∼52.5° is indicated.

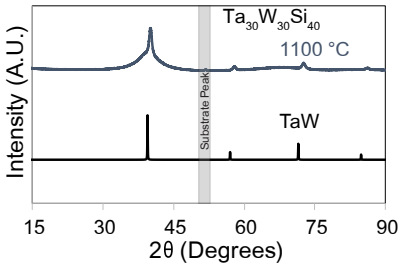

Figure 8.4: (a) Crystalline pattern of TaW (ICSD 106122 [11]) compared to that of a $Ta_{30}W_{30}Si_{40}$ thin films crystallized at 1100 °C. The silicon substrate peak artifact at ∼52.5° is indicated.

BIBLIOGRAPHY

1. N. Ohta and M. Rosen, *Color desktop printer technology*. Boca Raton, FL: CRC Press/Taylor & Francis Group, 2006.

2. H. P. Le, "Progress and trends in ink-jet printing technology," *Journal of Imaging Science and Technology*, vol. 42, no. 1, pp. 49–62, 1998.

3. J. S. Aden, J. H. Bohórquez, D. M. Collins, and M. Douglas Crook, "The third-generation HP thermal inkjet printhead," *Hewlett Packard Journal*, vol. 45, pp. 41–41, 1994.

4. C. Suryanarayana and A. Inoue, *Bulk Metallic Glasses*. CRC Press Taylor and Francis Group, 2011.

5. E. Axinte, "Metallic glasses from "alchemy" to pure science: Present and future of design, processing and applications of glassy metals," *Materials & Design*, vol. 35, pp. 518–556, Mar. 2012.

6. P. Sharma, N. Kaushik, H. Kimura, Y. Saotome, and A. Inoue, "Nano-fabrication with metallic glass–An exotic material for nano-electromechanical systems," *Nanotechnology*, vol. 18, p. 035302, 2007.

7. M. Imran and O. Lafi, "Glass transition kinetics and optical band gap $Se_{85-x}Sb_{15}Sn_x$(x=10, 11, 12.5, and 13) chalcogenide glasses," *Materials Chemistry and Physics*, vol. 129, pp. 1201–1206, 2011.

8. B. Cullity and S. Stock, *Elements of X-Ray Diffraction*. Prentice Hall, 3rd ed., 2001.

9. M. Birkholz, *Thin Film Analysis by X-Ray Scattering*. Wiley-VHC, 2006.

10. B. Aronsson, O. Tjomsland, R. Lundén, and H. Prydz, "The crystal structure of Mo_5Si_3 and W_5Si_3," *Acta Chemica Scandinavica*, vol. 9, pp. 1107–1110, 1955.

11. K. Tanaka, K. Nawata, H. Inui, M. Yamaguchi, and M. Koiwa, "Refinement of crystallographic parameters in refractory metal disilicides," *MRS Proceedings*, vol. 646, Jan. 2000.

12. Z. Tolmacheva and V. Kornilova, "Phase field boundaries in the W-Ta-Ti system at 1600 °C," *Izvestiya Akademii Nauk SSSR*, vol. 03, pp. 211–214, 1972.

13. J. P. Chu, J. S. C. Jang, J. C. Huang, H. S. Chou, Y. Yang, J. C. Ye, Y. Wang, J. W. Lee, F. X. Liu, P. K. Liaw, Y. C. Chen, C. M. Lee, C. L. Li, and C. Rullyani, "Thin film metallic glasses: Unique properties and potential applications," *Thin Solid Films*, vol. 520, pp. 5097–5122, June 2012.

14. G. Kumar, A. Desai, and J. Schroers, "Bulk Metallic Glass: The smaller the better," *Advanced Materials*, vol. 23, pp. 461–476, Jan. 2011.

15. R. A. Askeland, W. D. Childers, and W. R. Sperry, "The second-generation thermal inkjet structure," *Hewlett Packard Journal*, vol. 39, no. 4, pp. 28–31, 1988.

16. E. Peeters and S. Verdonckt-Vandebroek, "Thermal ink jet technology," *IEEE Circuits and Devices Magazine*, vol. 13, pp. 19–23, July 1997.

17. R. R. Allen, J. D. Meyer, and W. R. Knight, "Thermodynamics and hydrodynamics of thermal ink jets," *Hewlett-Packard Journal*, vol. 36, no. 5, pp. 21–27, 1985.

18. P.-H. Chen, W.-C. Chen, and S.-H. Chang, "Bubble growth and ink ejection process of a thermal ink jet printhead," *International Journal of Mechanical Sciences*, vol. 39, no. 6, pp. 683–695, 1997.

19. E.W. Cowell III, N. Alimardani, C. Knutson, J. Conley, D.A. Keszler, B. Gibbons, and J.F. Wager, "Advancing MIM electronics: Amorphous metal electrodes," *Advanced Materials*, vol. 23, pp. 74–78, 2011.

20. N. Alimardani, E.W. Cowell III, J.F. Wager and J. Conley Jr, "Impact of electrode roughness on metal–insulator–metal tunnel diodes with atomic layer deposited Al_2O_3 tunnel barriers," *Journal of Vacuum Science and Technology A*, vol. 1, pp. 01A113 – 01A113–5, 2012.

21. N. Alimardani and J. Conley Jr, "Step tunneling enhanced asymmetry in asymmetric electrode metal-insulator-insulator-metal tunnel diodes," *Applied Physics Letters*, vol. 102, p. 143501, 2013.

22. N. Alimardani, J. M. McGlone, J. F. Wager and J. F. Conley Jr., "Conduction processes in metal–insulator–metal diodes with Ta_2O_5 and Nb_2O_5 insulators deposited by atomic layer deposition," *Journal of Vacuum Science & Technology A*, vol. 32, p. 01A122, 2014.

23. N. Alimardani, S. W. King, B. L. French, C. Tan, B. P. Lampert, and J. F. Conley Jr., "Investigation of the impact of insulator material on the performance of dissimilar electrode metal—insulator—metal diodes," *Journal Applied Physics*, vol. 116, p. 024508, 2014.

24. M. Grubbs, X. Zhang, M. Deal, Y. Nishi, and B. Clemens, "Development and characterization of high temperature stable Ta-W-Si-C amorphous metal gates," *Applied Physics Letters*, vol. 97, p. 223505, 2010.

25. T. Matsukawa, Y. Liu, W. Mizubayashi, J. Tsukada, H. Yamauchi, K. Endo, Y. Ishikawa, S. O'uchi, H. Ota, S. Migita, Y. Moraita, Y. Morita, and M. Masahara, "Suppressing V_T and G_m variability of FinFETs using amorphous metal gates for 14 nm and beyond," *IEEE International Electron Devices Meeting*, pp. 8.2.1–8.2.4, 2012.

26. S. Kamisuki, T. Hagata, C. Tezuka, Y. Nose, M. Fujii, and M. Atobe, "A low power, small, electrostatically-driven commercial inkjet head," *IEEE Xplore*, pp. 63–68, 1998.

27. G. T. A. Kovacs, *Micromachined transducers sourcebook*. Boston, Ma.: WCB, 1998.

28. N. J. Nielson, "History of ThinkJet printhead development," *Hewlett-Packard Journal*, vol. 45, pp. 4–15, 1985.

29. Y. Wang, J. Bokor, and A. Lee, "Maskless lithography using drop-on-demand inkjet printing method," in *Microlithography 2004*, pp. 628–636, International Society for Optics and Photonics, 2004.

30. Y. Wang and J. Bokor, "Ultra-high-resolution monolithic thermal bubble inkjet print head," *Journal of Micro/Nanolithography, MEMS, and MOEMS*, vol. 6, no. 4, pp. 043009–043009, 2007.

31. E. Özkol, *Evaluation of the direct inkjet printing method for the fabrication of three-dimensional ceramic components*. PhD thesis, Universitätsbibliothek, 2012.

32. R. D. Boehm, P. R. Miller, J. Daniels, S. Stafslien, and R. J. Narayan, "Inkjet printing for pharmaceutical applications," *Materials Today*, vol. 17, no. 5, pp. 247–252, 2014.

33. E. V. Bhaskar and J. S. Aden, "Development of the thin-film structure for the ThinkJet printhead," *Hewlett Packard Journal*, vol. 36, no. 5, pp. 27–33, 1985.

34. J. P. Harmon and J. A. Widder, "Integrating the printhead into the HP DeskJet printer," *Hewlett Packard Journal*, vol. 39, no. 5, 1988.

35. R. Pugliese, "HP/OSU Amorphous Metals Meeting," Jan. 2015.

36. J. Park and Y. Oh, "Investigation to minimize heater burnout in thermal thin film print heads," *Microsystem technologies*, vol. 11, no. 1, pp. 16–22, 2005.

37. J.-H. Lim, K. Kuk, S.-J. Shin, S.-S. Baek, Y.-J. Kim, J.-W. Shin, and Y.-S. Oh, "Failure mechanisms in thermal inkjet printhead analyzed by experiments and numerical simulation," *Microelectronics Reliability*, vol. 45, no. 3, pp. 473–478, 2005.

38. G. Beurer, E. P. Hofer, and J. Patzer, "Process control for improvement of print quality and lifetime of bubble-jet printers," in *IS&T/SPIE 1994 International Symposium on Electronic Imaging: Science and Technology*, pp. 101–109, International Society for Optics and Photonics, 1994.

39. F. E. Anderson, B. V. Bell, R. W. Cornell, and Y. Guan, "Low ejection energy microfluid ejection heads." U.S. Patent 7749397 B2, July, 2010.

40. M. A. Buonanno, "Ink jet printhead having a palladium cavitation barrier and interconnect layer." E.U. Patent 0688672 A1, Dec., 1995.

41. T. Yasuda, T. Hatsui, M. Sakurai, S. Nagamochi, S. Takeuchi, Y. Ishida, and K. Shibata, "Substrate for liquid discharge head and liquid discharge head." U.S. Patent 8721048 B2, May, 2014.

42. M. Ikeda, J. Iri, H. Ishinaga, M. Kasamoto, S. Koyama, Y. Misumi, M. Mochizuki, T. Ozaki, and I. Saito, "Ink jet head with anti-cavitation film preventing kogation and erosion." E.U. Patent 1177899 A1, Feb., 2002.

43. A. I.-T. Pan, "Thermal ink jet resistor passivation." U.S. Patent 6715859 B2, Apr., 2004.

44. P. Gluche, R. Leuner, E. Kohn, C. Rembe, S. Aus der Wiesche, and E. P. Hofer, "Novel thermal microactuator based on CVD-diamond films," *IEEE Xplore*, pp. 483–486, 1998.

45. J. E. Abbott and R. Pugliese, "HP/OSU Amorphous Metals Meeting," 2014.

46. C.-J. Liou, Jian-Chiunand Chen and M.-H. Chuang, "Lower power supply thermal bubble printhead chip with MEMS technology increasing thermal energy effect," *NIP & Digital Fabrication Conference*, vol. 2004, no. 2, pp. 863–866, 2004.

47. S. Lee, M. Doxbeck, J. Mueller, M. Cipollo, and P. Cote, "Texture, structure and phase transformation in sputter beta tantalum coating," *Surface and Coatings Technology*, vol. 177-178, pp. 44–51, Jan. 2004.

48. R. Chandrasekharan, I. Park, R. I. Masel, and M. A. Shannon, "Thermal oxidation of tantalum films at various oxidation states from 300 to 700 °C," *Journal of Applied Physics*, vol. 98, no. 11, p. 114908, 2005.

49. A. S. Sedra, *Microelectronic circuits*. The Oxford series in electrical and computer engineering, New York: Oxford University Press, 6th ed ed., 2010.

50. D.-S. Wuu, C.-C. Chan, R.-H. Horng, W.-C. Lin, S. L. Chiu, and Y. Wu, "Structural and electrical properties of Ta–Al thin films by magnetron sputtering," *Applied Surface Science*, vol. 144, pp. 315–318, 1999.

51. D. S. Wuu, C. C. Chan, and R. H. Horng, "Characterization of sputtered Ta–Ru thin films for ink-jet heater applications," *Thin Solid Films*, vol. 373, no. 1, pp. 84–88, 2000.

52. W.-C. Choi, Z. Wan, J.-H. Ahn, D.-I. Kim, S.-Y. Shin, K.-I. Moon, J.-S. Park, J.-D. Kwon, and S.-H. Kwon, "Multifunctional Ru-AlN heating resistor films for high efficiency inkjet printhead," *Journal of Electroceramics*, vol. 32, no. 2-3, pp. 240–245, 2014.

53. D. S. Wuu, C. C. Chan, and R. H. Horng, "Material characteristics and thermal stability of cosputtered Ta–Ru thin films," *Journal of Vacuum Science & Technology A*, vol. 17, no. 6, pp. 3327–3332, 1999.

54. C. K. Chung, Y. L. Chang, T. S. Chen, and P. J. Su, "Annealing effects on microstructure and properties of Ta–Al thin film resistors," *Surface and Coatings Technology*, vol. 201, no. 7, pp. 4195–4200, 2006.

55. W. G. Hawkins, "Bubble jet printing device." U.S. Patent 4532530 A, Jul., 1985.

56. J. M. Eldridge, A. R. Forouhi, G. L. Gorman, and J. O. Moore, "Various properties of sputter-deposited HfB_2 films," *Journal of The Electrochemical Society*, vol. 137, no. 12, pp. 3905–3909, 1990.

57. D. S. Wuu, M. L. Lee, T. Y. Lin, and R. H. Horng, "Characterization of hafnium diboride thin film resistors by RF magnetron sputtering," *Materials Chemistry and Physics*, vol. 45, no. 2, pp. 163–166, 1996.

58. N. D. Cuong, D.-J. Kim, B.-D. Kang, C. S. Kim, K.-M. Yu, and S.-G. Yoon, "Characterization of tantalum nitride thin films deposited on SiO_2/ Si substrates using DC magnetron sputtering for thin film resistors," *Journal of The Electrochemical Society*, vol. 153, no. 2, pp. G164–G167, 2006.

59. H. Sorimachi and T. Hosoya, "Properties of sputtered W-Si-N thin-film resistors," *IEEE Xplore*, pp. 596–603, 1988.

60. M. Regan, M. Leban, T. Berdahl, C. Shell, and R. Debnam, "High resistivity materials for improved thermal inkjet printheads," *NIP & Digital Fabrication Conference*, vol. 2000, no. 1, pp. 38–38, 2000.

61. M. J. Regan and M. Leban, "High efficiency printhead containing a novel nitride-based resistor system." U.S. Patent 6336713 B1, Jan. 2002.

62. D. S. Wuu, R. H. Horng, C. C. Chang, and Y. Y. Wu, "Various properties of sputter-deposited Ta–Ru thin films," *Applied Surface Science*, vol. 169, pp. 392–395, 2001.

63. M. J. Regan, "High efficiency printhead containing a novel oxynitride-based resistor system." U.S. Patent 6299294 B1, Oct., 2001.

64. W.-S. Kwack, H.-S. Moon, S.-J. Jeong, Q.-M. Wang, and S.-H. Kwon, "Hybrid functional IrO_2-TiO_2 thin film resistor prepared by atomic layer deposition for thermal inkjet printheads," *Transactions of Nonferrous Metals Society of China*, vol. 21, pp. 88–91, 2011.

65. S.-H. Kwon, S.-W. Kang, and K.-H. Kim, "Controlling the temperature coefficient of resistance and resistivity in RuO_2–TiO_2 thin films by the intermixing ratios between RuO_2 and TiO_2," *Applied Physics Letters*, vol. 92, no. 18, pp. 181903–181903, 2008.

66. S.-H. Kwon and K.-H. Kim, "Hybrid functional RuO_2–Al_2O_3 thin films prepared by atomic layer deposition for inkjet printhead," *Journal of Solid State Electrochemistry*, vol. 14, no. 2, pp. 225–229, 2010.

67. S.-H. Park, Min-Ho and Kim, "Temperature coefficient of resistivity of TiAlN films deposited by radio frequency magnetron sputtering," *Transactions of Nonferrous Metals Society of China*, vol. 23, no. 2, pp. 433–438, 2013.

68. S.-C. Moon and S. H. Kim, "CrAlN film deposited by magnetron sputtering for the inkjet printer head," *Journal of Nanoscience and Nanotechnology*, vol. 14, no. 12, pp. 8946–8951, 2014.

69. M. Miller and P. Liaw, *Bulk Metallic Glasses*. Springer Science+Business Media, 2010.

70. P. Atkins, T. Overton, J. Rourke, M. Weller, and F. Armstrong, *Shriver and Atkins' Inorganic Chemistry*, vol. 5th Edition. Oxford University Press, 2010.

71. D. B. Miracle, T. Egami, K. M. Flores, and K. F. Kelton, "Structural aspects of metallic glasses," *MRS Bulletin*, vol. 32, no. 08, pp. 629–634, 2007.

72. N. Kovalenko, Y. Kransny, and U. Krey, *Physics of Amorphous Metals*. Berlin: Wiley-VCH, 2001.

73. W. Klement, R. Willens, and P. Duwez, "Reaction kinetics in differential thermal analysis," *Nature*, vol. 187, no. 4740, pp. 869–870, 1960.

74. H. Chen, "Glassy metals," *Rep. Prog. Phys.*, vol. 43, no. 7, pp. 353–432, 1980.

75. R. C. Taylor, T. R. McGuire, J. M. D. Coey, and A. Gangulee, "Magnetic properties of amorphous neodynmuim-transition metal films," *Journal Applied Physics*, vol. 49, no. 5, pp. 2885–2893, 1978.

76. C. A. Schuh, T. C. Hufnagel, and U. Ramamurty, "Mechanical behavior of amorphous alloys," *Acta Materialia*, vol. 55, pp. 4067–4109, July 2007.

77. W. L. Johnson, "Bulk amorphous metal-An emerging engineering material," *JOM Journal of the Minerals, Metals and Materials Societey*, vol. 54, no. 3, pp. 40–42, 2002.

78. A. Argon, "Plastic deformation in metallic glasses," *Acta Metallurgica*, vol. 27, pp. 47–58, Jan. 1979.

79. C. Carter, *Ceramic Materials Science and Engineering*. New York, N.Y.: SPringer Science+Business Media, LLC, 2007.

80. J. Tregilgas, "How we developed an amorphous hinge material," *Advanced Materials and Processes*, pp. 46–49, 2005.

81. S. Hata, K. Sato, and A. Shimokohbe, "Fabrication of thin film metallic glass and its application to microactuators," *Proc. SPIE 3892, Device and Process Technologies for MEMS and Microelectronics*, pp. 97–108, 1999.

82. M. Ylönen, T. Vähä-Heikkilä, and H. Kattelus, "Amorphous metal alloy based MEMS for RF applications," *Sensors and Actuators A: Physical*, vol. 132, pp. 283–288, Nov. 2006.

83. Y.-C. Lin, Y.-C. Tsai, T. Ono, P. Liu, M. Esashi, T. Gessner, and M. Chen, "Metallic glass as a mechanical material for microscanners," *Advanced Functional Materials*, vol. 25, pp. 5677–5682, Sept. 2015.

84. A. Inoue and K. Hasimoto, *Amorphous and Nanocrystalline Materials, Preperation, Properties and Applications*. Springer, 2001.

85. A. Takeuchi and A. Inoue, "Calculation of mixing enthalpy and mismatch entropy for ternary amorphous alloys," *Materials Transactions-JIM*, vol. 41, no. 11, pp. 1372–1378, 2000.

86. R. Busch, Y. J. Kim, and W. L. Johnson, "Thermodynamics and kinetics of undercooled liquid and the glass transition of the $Zr_{41.2}Ti_{12.8}Cu_{12.0}Ni_{10.0}Be_{22.5}$," *Journal Applied Physics*, vol. 77, pp. 4039–4043, 1995.

87. H. Kissinger, "Reaction kinetics in differential thermal analysis," *Analytical Chemistry*, vol. 29, no. 11, pp. 1702–1706, 1957.

88. H. Kissinger, "Variation of peak temperature with heating rate in differential thermal analysis," *Journal of Research of the National Bureau of Standards*, vol. 57, no. 4, pp. 217–221, 1956.

89. Y. Wang, Q. Wang, J. Zhao, and C. Dong, "Ni-Ta binary bulk metallic glasses," *Scripta Materiela*, vol. 63, no. 2, pp. 178–179, 2010.

90. D. Meng, J. Yi, D. Zhao, D. Ding, H. Bai, M. Pan, and W. Wang, "Tantalum based bulk metallic glasses," *Journal of Non-crystalline Solids*, vol. 357, no. 7, pp. 1787–1790, 2011.

91. X. Zhang, E. Ma, and J. Xu, "Mechanically alloyed multi-component Mo-based amorphous metals," *Journal of Non-Crystalline Solids*, vol. 352, pp. 3985–3994, 2006.

92. T. Yoshitake and H. I. Y. Kubo, "Preparation of refractory transition metal-metalloid amorphous alloys and their thermal stability," *Materials Science and Engineering*, vol. 97, pp. 269–271, 1988.

93. J. Ouyang, R. Wongpiya, M. E. Grubbs, M. D. Deal, B. M. Clemens, and Y. Nishi, "Effect of composition on structural and electrical properties of amorphous Ta-W-Si-C metal thin films," *ECS Solid State Letters*, vol. 2, pp. P86–P88, July 2013.

94. J. Oh, J. Woollam, K. Aylesworth, D. Sellmyer, and J. Pouch, "Thermal and structural stability of cosputtered amorphous Ta_XCu_{1-X} alloy thin films on GaAs," *Journal Applied Physics*, vol. 60, no. 12, pp. 2885–2893, 1986.

95. M. El-Eskandarany, W. Zhang, and A. Inoue, "Mechanically induced crystallin glassy phase transition of mechanically alloyed $Ta_{55}Zr_{10}Al_{10}Ni_{10}Cu_{15}$ multi-component alloy powders," *Journal of Alloyed Compounds*, vol. 350, pp. 222–231, 2003.

96. R. T. Ott, C. Fan, J. Li, and T. C. Hufnagel, "Structure and properties of Zr-Ta-Cu-Ni-Al bulk metallic glasses and metallic glass matrix composites," *Journal of Non-Crystalline Solids*, vol. 317, pp. 158–163, 2003.

97. H. Choi-Yim, M. Tokarz, J. Bilello, and W. L. Johnson, "Structure and properties of Ni_{60} ($Nb_{100-x}Ta_x$) $_{34}Sn_6$ bulk metallic glass alloys," *Journal of Non-crystalline Solids*, vol. 352, pp. 747–755, 2006.

98. S. Kajita, S. Kohara, Y. Onodera, T. Tukunaga, and E. Matsubara, "Structural analysis of Pd-Cu-Si metallic glassy alloy films with varying glass transition temperatures," *Materials Transactions*, vol. 52, pp. 1349–1355, 2011.

99. Z. Yuan, B. Wang, Y. Tong, and X. Chen, "Effect of annealing on kinetics of glass transition and crystallization in Co-Fe-Ta-B amorphous alloy," *Journal of Alloys and Compounds*, vol. 429, pp. 104–110, 2007.

100. S. N. Mott, *Conduction in Non-Crystalline Materials, 2nd Edition*. Oxford Science Publications, 1993.

101. J. S. Dugdale, *The Electrical Properties of Disordered Metals*. Cambridge University Press, 1995.

102. D. C. Giancoli, *Physics, Principles with Applications*. Prentice-Hall, 1980.

103. S. Sze and K. Ng, *Physics of Semiconductor Devices*. John Wiley And Sons, 3rd ed., 2007.

104. R. Pierret, *Semiconducter Device Fundamentals*. Addison-Wesley Publishing, 1996.

105. D. K. Schroder, *Semiconductor Material and Device Characterization, 3rd Ed.* John Wiley and Sons Inc., 2006.

106. W. den Boer, *Active Matrix Liquid Crystal Display*. Elsevier Inc., 1st ed., 2005.

107. S. Muir, J. Meyer, and J. Brewer, "Amorphous-metal thin films enable ultra-high-definition display backplanes," *Information Display*, vol. 32, pp. 22–27, Jan. 2016.

108. D. Griffiths, *Introduction to Quantum Mechanics*. Pearson Prentice Hall, 2005.

109. J. G. Simmons, "Generalized formula for the electric tunnel effect between similar electrodes separated by a thin insulating film," *Journal Applied Physics*, vol. 34, pp. 1793–1803, June 1963.

110. J. G. Simmons, "Electric tunnel effect between dissimilar electrodes separated by a thin insulating film," *Journal Applied Physics*, vol. 34, pp. 2581–2590, September 1963.

111. S. Wolf and R. Tauber, *Silicon Processing for the VLSI Era*. Lattice Press, 2000.

112. B. Chapman, *Glow Discharge Processes*. John Wiley and Sons Inc, 1980.

113. M. Ohring, *Materials Science of Thin Films Depositions and Structure*. Academic Press, 2002.

114. P. Sharma, W. Zhang, H. Kimura, and A. Inoue, "Nanoscale patterning of Zr-Al-Cu-Ni metallic glass thin films deposited by magnetron sputtering," *Journal of Nanoscience and Nanotechnology*, vol. 5, pp. 416–420, 2005.

115. Asylum Research, *Asylum Research Atomic Force Microscopes MFP 3D Manual*, version 0408 ed., 2008.

116. I. Kojima and B. Li, "Structural characterization of thin films by x-ray reflectivity," *The Rigaku Journal*, vol. 16, no. 2, pp. 31–42, 1999.

117. L. G. Parratt, "Surface studies of solids by total reflection of x-rays," *Physical Review*, vol. 95, pp. 359–369, July 1954.

118. J. F. Watts and J. Wolstenholme, *An introduction to surface analysis by XPS and AES*. Chichester, West Sussex, England ; New York: J. Wiley, 2003.

119. W. Stickle, "The Use of Chemometrics in AES and XPS Data Treatment," in *Surface Analysis by Auger and X-Ray Photoelectron Spectroscopy* (D. Briggs and J. Grant, eds.), pp. 377–398, Chichister, West Sussex, UK: IM Publications, 2003.

120. J. Goldstein, ed., *Scanning Electron Microscopy and X-Ray Microanalysis*. New York: Kluwer Academic/Plenum Publishers, 3rd ed ed., 2003.

121. R. F. Egerton, *Physical Principles of Electron Microscopy: An Introduction to TEM, SEM, and AEM*. New York, NY: Springer, 2005. OCLC: ocm61714990.

122. R. F. Egerton, *Electron Energy-Loss Spectroscopy in the Electron Microscope*. The language of science, New York: Springer, third edition ed., 2011.

123. D. L. Smith, *Thin-Film Deposition Principles and Practice*. McGraw-Hill, 1996.

124. S. M. George, "Atomic layer deposition: An overview," *Chemical Review*, vol. 10, pp. 111–131, 2010.

125. M. Leskelä and M. Ritala, "Atomic layer deposition (ALD): From precursors to thin film structures," *Thin Solid Films*, vol. 409, pp. 138–146, 2002.

126. R. L. Puurunen, "Surface chemistry of atomic layer deposition: A case study for trimethylaluminum/water process," *Journal Applied Physics*, vol. 97, p. 121301, 2005.

127. G. Betz and G. K. Wehner, "Sputtering of multicomponent materials," in *Sputtering by Particle Bombardment II* (R. Behrish, ed.), vol. 52, pp. 11–90, Berlin, Heidelberg: Springer Berlin Heidelberg, 1983.

128. L. R. Shaginyan, M. Misina, S. Kadlec, and L. Jastrabi, "Mechanism of the film composition formation during magnetron sputtering of WTi," *Journal of Vacuum Science & Technology A*, vol. 19, no. 5, pp. 2554–2567, 2001.

129. Y. Murakami and T. Shingyoji, "Compositional difference between films and targets in sputtering of refractory metal silicides," *Journal of Vacuum Science & Technology A*, vol. 8, pp. 851–854, Mar. 1990.

130. W. D. Westwood, ed., *Sputter Deposition*, AVS Pacific Northwest Chapter, The Short Course Executive Committee American Vacuum Society, 1996.

131. W. Haynes, *CRC Handbook of Chemistry and Physics 92nd Edition 2011-2012*. CRC Press Taylor and Francis Group, 2011.

132. A. Schauer and M. Roschy, "R.F. sputtered β-tantalum and b.c.c. tantalum films," *Thin Solid Films*, vol. 12, pp. 313–317, Oct. 1972.

133. M. Einat and M. Grajower, "Microboiling measurements of thermal-inkjet heaters," *Journal of Microelectromechanical Systems*, vol. 19, pp. 391–395, Apr. 2010.

134. E.W. Cowell III, *Electronic Device and Nanolaminate Application of Amorphous Metal Thin Films*. PhD thesis, Oregon State University, 2013.

135. M. Lenzlinger and E. H. Snow, "Fowler-Nordheim tunneling into thermally grown SiO_2," *Journal of Applied Physics*, vol. 40, pp. 278–283, Jan. 1969.

136. R. P. Oleksak, E. B. Hostetler, B. T. Flynn, J. M. McGlone, N. P. Landau, J. F. Wager, W. F. Stickle, and G. S. Herman, "Thermal oxidation of Zr–Cu–Al–Ni amorphous metal thin films," *Thin Solid Films*, vol. 595, Part A, pp. 209–213, Nov. 2015.

137. E. I. Oborina, H. N. Benjamin, and A. M. Hoff, "Fowler–Nordheim analysis of oxides on 4h-SiC substrates using noncontact metrology," *Journal of Applied Physics*, vol. 106, p. 083703, Oct. 2009.

138. J. A. Dean, *Lange's Handbook of Chemistry*, vol. 15th Edition. McGraw-Hill, 1999.

139. V. V. Afanas'ev, M. Houssa, and A. Stesmans, "Band alignments in metal–oxide–silicon structures with atomic-layer deposited Al_2O_3 and ZrO_2," *Journal of Applied Physics*, vol. 91, pp. 3079–3084, Feb. 2002.